MINISTÉRIO DA EDUCAÇÃO
UNIVERSIDADE FEDERAL DE CIÊNCIAS DA SAÚDE DE PORTO ALEGRE
PRÓ-REITORIA DE PESQUISA E PÓS-GRADUAÇÃO
PROGRAMA DE PÓS-GRADUAÇÃO EM TECNOLOGIAS DA INFORMAÇÃO E GESTÃO EM SAÚDE

Samara Prass dos Santos

Bayesian optimization of a laser-plasma accelerator aiming the production of high-energy electron beams for VHEE radiotherapy

Porto Alegre
2025

Samara Prass dos Santos

Bayesian optimization of a laser-plasma accelerator aiming the production of high-energy electron beams for VHEE radiotherapy

Dissertation for the Academic Master's Program in Information Technology and Management in Health at the Federal University of Health Sciences of Porto Alegre.

Advisor: Prof. Dr. Alexandre Bonatto
Co-advisor: Prof. Dr Mirko Salomón Alva Sánchez

Porto Alegre
2025

Catalogação na Publicação

Santos, Samara Prass dos
Bayesian optimization of a laser-plasma accelerator aiming the production of high-energy electron beams for VHEE radiotherapy / Samara Prass dos Santos. -- 2025.
103 p. : il., graf., tab. ; 30 cm.

Dissertação (mestrado) -- Universidade Federal de Ciências da Saúde de Porto Alegre, Programa de Pós-Graduação em Tecnologias da Informação e Gestão em Saúde, 2025.

Orientador(a): Alexandre Bonatto ; coorientador(a): Mirko Salomón Alva-Sánchez.

1. Bayesian optimization. 2. VHEE. 3. Bubble Regime. 4. LPA.

Sistema de Geração de Ficha Catalográfica da UFCSPA com os dados fornecidos pelo(a) autor(a).

Samara Prass dos Santos

Bayesian optimization of a laser-plasma accelerator aiming the production of high-energy electron beams for VHEE radiotherapy

Master's Dissertation presented to the Graduate Program in Information Technologies and Health Management at the Federal University of Health Sciences of Porto Alegre as a partial requirement for obtaining the title of Master in Information Technologies and Health Management.

Advisor: Prof. Dr. Alexandre Bonatto
Co-advisor: Prof. Dr. Mirko Salomón Alva Sánchez

Approved on August 25, 2025

DEFENSE COMMITTEE:

Prof. Dr. Henrique Trombini
Universidade Federal de Ciências da Saúde de Porto Alegre

Prof. Dr. José Rafael Bordin
Universidade Federal de Pelotas

Profª. Drª. Thatiane Alves Pianoschi Alva
Universidade Federal de Ciências da Saúde de Porto Alegre

ACKNOWLEDGEMENTS

First and foremost, I would like to express my deepest gratitude to my advisor, Professor Alexandre Bonatto, whose expertise, guidance, and unwavering support were fundamental to the completion of this dissertation. I extend my thanks to the Beam Physics Group of the Federal University of Health Sciences of Porto Alegre (UFCSPA), especially Bruno Silveira Nunes, for their support in the simulations, and the faculty and staff of the Academic Master's Degree in Information Technology and Health Management at UFCSPA for the opportunity.

To my colleagues and friends, thank you for the camaraderie, the productive discussions, and for making this journey more enjoyable.

Finally, my heartfelt thanks go to my family. To my mother, my brother and my partner, I am eternally grateful for your love, patience, and endless support. This work is as much yours as it is mine.

I can do all this through Him who gives me strength.

ABSTRACT

Radiotherapy is one of the main treatment modalities for malignant tumors. However, the dose-limiting toxicity of normal tissues is still one of the significant obstacles to its application. Proton therapy has shown promise for its potential suitability for this aspect, however their cost is currently considered too high for widespread use, as significant infrastructure is necessary to transport the beams to patients. Electrons with energies ranging from 50 to 250 MeV, known as very high energy electrons (VHEE), exhibit deep tissue penetration, rendering them an attractive option for conventional radiotherapy and for FLASH radiotherapy, being the last one highlighted as an alternative capable of providing higher curative doses, making it possible to reduce toxicity in normal tissues and overcome tumor resistance to radiation. Equipment based on FLASH technology from VHEE becomes advantageous to produce this effect. In particular, for this purpose, laser-plasma accelerators have been studied to produce them compactly and at a reduced cost, if compared to conventional ion acceleration in ciclotrons, with great potential for medical applications. In this context, this work proposes the use of Bayesian optimization of a laser-plasma accelerator to produce electron beams with suitable properties for VHEE radiotherapy. The optimization process, spanning 377 simulations, resulted in a high-quality electron beam with a total charge of approximately 1.86 nC. The final energy spectrum is bimodal, with distinct, quasi-monoenergetic peaks at therapeutically relevant energies of 160 MeV and 197 MeV, and a sharp cutoff at 300 MeV. This represents a "cleaner" and qualitatively superior spectrum for VHEE applications compared to previous work, with a significant reduction in the low-energy electron population. A correlation analysis revealed important physical insights, identifying gas composition as a potential determinant of beam energy and plasma ramp geometry as a potential main control for the accelerated charge, requiring further parametric analysis. However, the study was limited by a lack of convergence of the input parameters, which was attributed to the use of a Helium-Nitrogen gas mixture. The computational feasibility of this research was supported by the National Laboratory for Scientific Computing (LNCC/MCTI, Brazil), which provided access to the Santos Dumont supercomputer (Project LPA-FARMA), contributing significantly to the results reported in this work.

Keywords: Bayesian optimization; VHEE; FLASH radiotherapy; Bubble Regime; LPA.

RESUMO

A radioterapia é uma das principais modalidades de tratamento para tumores malignos. No entanto, a toxicidade dos tecidos normais, que limita a dose, ainda é um dos obstáculos significativos à sua aplicação. A protonterapia tem se mostrado promissora por sua potencial adequação a esse aspecto; contudo, seu custo é atualmente considerado elevado demais para o uso generalizado, uma vez que é necessária uma infraestrutura significativa para transportar os feixes até os pacientes. Elétrons com energias variando de 50 a 250 MeV, conhecidos como elétrons de altíssima energia (VHEE, do inglês Very High Energy Electrons), exibem penetração profunda nos tecidos, tornando-os uma opção atraente para a radioterapia convencional e para a radioterapia FLASH. Esta última destaca-se como uma alternativa capaz de fornecer doses curativas mais elevadas, possibilitando a redução da toxicidade em tecidos normais e a superação da resistência tumoral à radiação. Equipamentos baseados na tecnologia FLASH a partir de VHEE tornam-se vantajosos para produzir tal efeito. Em particular, para este propósito, aceleradores a laser-plasma (LPA) têm sido estudados para produzi-los de forma compacta e com custo reduzido, se comparados à aceleração convencional de íons em cíclotrons, apresentando grande potencial para aplicações médicas. Neste contexto, este trabalho propõe o uso da otimização Bayesiana de um acelerador de laser-plasma para produzir feixes de elétrons com propriedades adequadas para radioterapia VHEE. O processo de otimização, abrangendo 377 simulações, resultou em um feixe de elétrons de alta qualidade com uma carga total de aproximadamente 1,86 nC. O espectro de energia final é bimodal, com picos distintos e quase monoenergéticos em energias terapeuticamente relevantes de 160 MeV e 197 MeV, além de um corte nítido em 300 MeV. Isso representa um espectro "mais limpo" e qualitativamente superior para aplicações VHEE em comparação a trabalhos anteriores, com uma redução significativa na população de elétrons de baixa energia. Uma análise de correlação revelou percepções físicas importantes, identificando a composição do gás como um potencial determinante da energia do feixe e a geometria da rampa de plasma como um possível controle principal para a carga acelerada, exigindo análises paramétricas adicionais. No entanto, o estudo foi limitado pela falta de convergência dos parâmetros de entrada, o que foi atribuído ao uso de uma mistura gasosa de Hélio-Nitrogênio. A viabilidade computacional desta pesquisa foi apoiada pelo Laboratório Nacional de Computação Científica (LNCC/MCTI, Brasil), que forneceu acesso ao supercomputador Santos Dumont (Projeto LPA-FARMA), contribuindo significativamente para os resultados relatados neste trabalho.

Palavras-chave: Otimização Bayesiana; VHEE; Radioterapia FLASH; Regime de Bolha; LPA.

List of Figures

List of Tables

Contents

1. INTRODUCTION

According to estimates by the National Cancer Institute for the triennium 2023-2025, there is an expectation of approximately 704,000 new cases of cancer in Brazil (INCA, 2022). The World Health Organization (WHO) predicts the international number of new cases will reach about 29 million by 2040, and if efforts are not made to change this trend, more than 16 million deaths from this cause are expected in 2040 (J Ferlay, 2024). The treatment of malignant tumors can be carried out through surgeries, chemotherapy, targeted therapy, immunotherapy, and radiotherapy, with at least one course of the latter modality being necessary in approximately 50% of cases. Radiotherapy is considered a critical factor in effective cancer services (Lv et al., 2022; Abdel-Wahab et al., 2021), and its objective is to deliver sufficient radiation to eradicate cancerous cells without affecting normal tissues or at least reduce them to clinically acceptable limits (Arthur Accioly Rosa, 2022).

Conventional techniques currently used in teletherapy treatments allow for high-gradient dose conformation and modulation, such as intensity-modulated radiotherapy (IMRT), volumetric modulated arc therapy (VMAT), and proton therapy. However, dose-limiting toxicity of normal tissues remains one of the significant obstacles to the development of tumor radiotherapy (Bourhis et al., 2019; Favaudon et al., 2014). Regarding this aspect, proton therapy has shown promise for its potential suitability due to the following factors outlined by (Bulanov and Khoroshkov, 2002): a proton beam experiences minimal scattering by atomic electrons, leading to reduced irradiation of healthy tissues adjacent to the tumor; the deceleration length of protons with a specific energy remains constant, which helps avoid unintended irradiation of healthy tissues beyond the tumor; and the presence of a sharp peak in proton energy losses within tissues (known as the Bragg peak), that significantly increases the radiation dose near the beam's endpoint. Nevertheless, the cost of this therapeutic modality is currently considered too high for widespread use, as significant infrastructure is necessary to transport the beams to patients, as in Figure 1.1.

While the cost of a conventional radiotherapy system is in the range of $6 million, the establishment of a single proton therapy treatment center can exceed $50 million, even for the most basic configurations. As a direct consequence of this economic factor, access to proton therapy remains highly restricted. It is estimated that fewer than 1% of all radiotherapy patients globally are treated with protons. This is reflected in the number of available facilities: as of March 2023, only 106 proton therapy centers were operational worldwide, compared to over 8,000 conventional radiotherapy installations (Yan et al., 2023).

Electrons with energies ranging from 50 to 250 MeV, termed very high energy electrons (VHEE), possess significant tissue-penetrating capabilities, making them an alternative to conventional radiotherapy. This therapy offers advantages such as low sensitivity to medium heterogeneity compared to X-rays and protons, unique focusing and directing capabilities, flatter

Figure 1.1: Proton therapy single room systems, with a much smaller design. These systems are less expensive and attractive to smaller centers like regional and community hospitals.

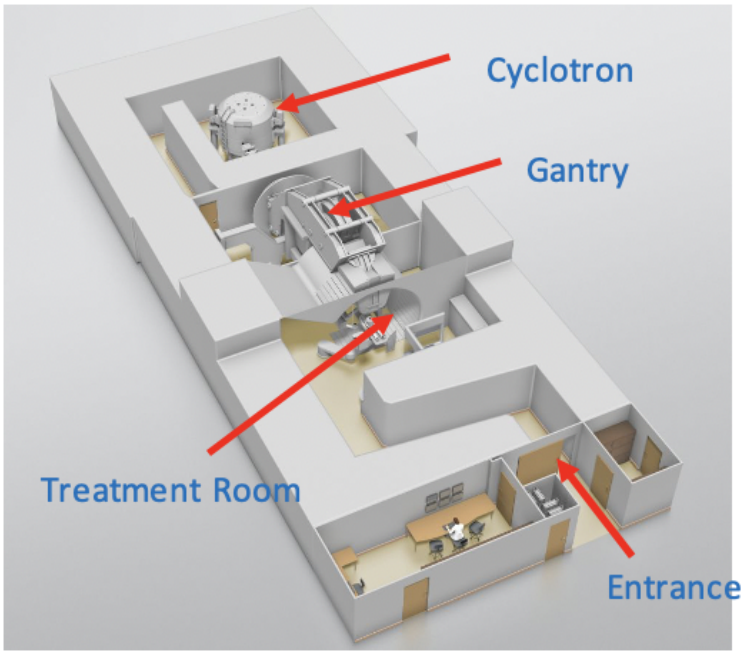

Source: (Maughan, 2022)

percentage depth dose profiles than X-rays, a sharper dose fall-off (penumbra) that minimizes damage to surrounding healthy tissues, and lower skin dosage.

Recent studies have demonstrated the capability to focus VHEE beams to create well-defined and precise high-dose concentrations in small volumes, with the ability to have an entry dose even lower than proton beams (Kokurewicz et al., 2019, 2021; Whitmore et al., 2021; Assalmi et al., 2025; Svendsen et al., 2021). This establishes VHEE beams as viable and highly advantageous aspect for advanced radiotherapy.

In addition to the potential of focused VHEE beams for the treatment of deep tumors, VHEE beams are a promising modality for FLASH radiotherapy (FLASH-RT) due to the high achievable dose rates (Corsini et al., 2021; Kokurewicz et al., 2021). By reducing the total dose administration time, FLASH-RT has the potential to enable the delivery of higher curative doses by increasing the tolerance of normal tissue, thereby potentially overcoming tumor resistance to radiation (Bourhis et al., 2019; Vozenin et al., 2019; Lin et al., 2021).

Equipment capable of producing the FLASH effect to treat deep-seated tumors could be developed employing X-rays (FLASH-X-ray), protons (FLASH-proton) or very high-energy electrons (FLASH-VHEE) (Bourhis et al., 2019). Of these, FLASH-VHEE systems appear most advantageous: a FLASH-X-ray accelerator would demand at least 100 times more energy than used for a FLASH electrons (Bourhis et al., 2019), and proton-based FLASH requires extensive—and costly—infrastructure for acceleration and beam transport.

Despite the aforementioned advantages of VHEE beams (over other radiation sources), com-

mercial equipment capable of delivering such beams is not yet available (Corsini et al., 2021; CERN, 2022). Emerging acceleration technologies like the Compact Linear Collider (CLIC) and LPA (CERN, 2022) hold promise in enabling the construction of such equipment. Particularly, LPA can compactly generate VHEE beams, potentially reducing costs compared to conventional LINACs (Kokurewicz et al., 2017; Corsini et al., 2021).

Conceptually proposed by Tajima and Dawson in 1979 (Tajima and Dawson, 1979), LPA involves a laser pulse propagating through a plasma, perturbing its electron density. Under specific conditions (Esarey et al., 2009), the transverse oscillation of these charged particles generates a high-amplitude wakefield, suitable for electron acceleration. While LINACs based on conventional Radio Frequency (RF) technology are limited to acceleration gradients of approximately 100 MeV/m, LPA can provide gradients up to 100 GeV/m (Esarey et al., 2009), enabling the production of high-energy electron beams over short distances. Although LPA technology is still in development, experimental results have demonstrated the production of 8 GeV electron beams in plasmas only 20 cm long (Gonsalves et al., 2019). These characteristics position LPA as a promising candidate for the development of compact, cost-effective accelerators with significant potential for medical applications.

Two regimes of LPA have garnered attention in research: the bubble (or nonlinear) regime and the self-modulated (SM) regime. In the SM regime, a laser pulse with an envelope initially longer than the plasma wavelength undergoes self-modulation as it propagates through the plasma. In the self-modulation process, caused by the interaction of the laser pulse with the plasma wakefield, the laser pulse is fragmented. Under proper conditions, the laser fragments may work as shorter pulses, driving wakefields and forming ionic cavities (bubbles) due to electron depletion by the laser (Esarey et al., 2009). As a result of the irregularity of the laser pulse fragments resulting from the self-modulation process, the variation in the wakefields excited by them, as well as their overlap, leads to the acceleration of electron beams with low quality, that is, with high energy spread and poor collimation. In the bubble regime, on the other hand, an intense laser pulse, initially shorter than the plasma wavelength, propagates in the plasma, forming bubbles in the plasma wake. Electrons from the plasma, captured in the back of these bubbles in a process known as self-injection, can be accelerated by the intense wakefields, forming ultra-short, high-energy electron bunches with quasi-monoenergetic energy spectra, through a series of intricate processes (Esarey et al., 2009; Pukhov et al., 2004; Panaino et al., 2025).

Despite its promise, LPA involves complex dynamics, and the properties of the accelerated electron beams depend on numerous laser and plasma parameters. As a result, studies of LPA-based applications frequently rely on extensive and costly ensembles of particle-in-cell (PIC) simulations to sweep the multidimensional parameter space. To mitigate this computational expense, an effective alternative is employing Bayesian optimization (BO), a global algorithm for intelligently exploring expensive-to-evaluate black-box functions and identifying optimal parameter settings. Previous studies have demonstrated that BO is an effective methodology for improving LPAs in the generation of VHEE beams. The work by (Jalas et al., 2021) demon-

strated the effectiveness of BO in autonomously tuning key laser and plasma parameters to optimize beam quality, achieving notable improvements in charge and energy spread through a systematic iterative process. Additionally, a study incorporating multitask BO illustrated how integrating reduced physical models with high-fidelity simulations can significantly lower computational costs while still capturing the complex nonlinear dynamics inherent in LPAs. This multitask approach facilitates efficient exploration of parameter spaces, enhancing the optimization process without sacrificing beam quality. Collectively, these findings underscore the versatility and efficacy of BO as a powerful tool for advancing LPA technology, ultimately contributing to more reliable and effective VHEE beam generation for radiotherapy applications.

Considering the mentioned factors, this study proposes Bayesian optimization of LPA to produce electron beams for VHEE radiotherapy using data from PIC simulations. The work aims to optimize the input parameters of LPA PIC simulations, defining laser pulse and plasma profiles. An objective function, based on relevant output parameters such as electron beam energy, charge, and quality, will guide the optimization process. Post-optimization, new input parameters will be generated and used in a subsequent PIC simulation to validate the methodology. Prior research conducted by the Beam Physics Group at the Federal University of Health Sciences of Porto Alegre focused on Bayesian optimization of a LPA operating in the self-modulated regime for the production of Mo^{99}, without considering beam quality. This study aims to extend this work by applying Bayesian optimization to a LPA operating in the bubble regime, with the goal of generating a high-quality VHEE beam suitable for use in radiotherapy.

The Institute of Energy and Nuclear Research (IPEN) has recently received approval to acquire a 15 TW laser, making it the most powerful in the Southern Hemisphere (Vieira Junior and Samad, 2024). To ensure practical relevance and experimental feasibility of this optimization approach, this work will be scaled to IPEN's laser system parameters to guide future VHEE radiotherapy experiments nd provide a computational framework that can be directly applied to real-world experimental conditions.

The work is structured in six chapters. Chapter 2 (THEORY) presents the theoretical foundations necessary for the study, covering the characteristics of very high energy electron (VHEE) beams and their use in radiotherapy, the fundamental properties of laser-plasma accelerators (LPAs), and the principles of Bayesian optimization (BO) via Gaussian process regression. Chapter 3 (METHODS) details the methodology, which involves defining the initial LPA parameter space, using the Fourier-Bessel Particle-In-Cell (FBPIC) code, and applying the Bayesian optimization algorithm to PIC simulations. Chapter 4 (ARTICLE) presents the results in publication format, following the dissertation model of the Graduate Program in Information Technologies and Health Management at the Federal University of Health Sciences of Porto Alegre. Specifically, the chapter presents the progress of the work, focusing on the Bayesian optimization of an LPA in the bubble regime for the production of high-energy electron beams suitable for VHEE radiotherapy. Chapter 5 (DISCUSSION) discusses the results obtained in the application of the optimization for VHEE-RT, along with a correlation analysis

between the parameters, and also briefly addresses the results of the previous study that dealt with the application of BO for the production of Mo^{99}. Chapter 6 (CONCLUSIONS) summarizes the conclusions of the work. Finally, appendices A (APPENDIX A - BOOK CHAPTER) and B (APPENDIX B - ARTICLE) report the initial Bayesian optimization studies of the self-modulated laser wakefield acceleration (SM-LWFA) for the production of the radioisotope Molybdenum-99 (Mo^{99}).

2. THEORY

This chapter presents the theoretical foundations required to carry out the proposed study, encompassing the key characteristics of very-high-energy electron (VHEE) beams and their use in radiotherapy, the fundamental properties of laser–plasma accelerators, and the principles of Bayesian optimization via Gaussian process regression.

2.1 VHEE Beams

Electrons have been used in radiotherapy since the 1950s, being initially extracted mostly from betratons. Only in the 1970s, high-energy linear accelerators with multienergy electron beam capabilities were available for clinical use. Currently, the maximum penetration capacity of electron beams used in radiotherapy for conventional clinical treatments reaches approximately 12.5 centimeters into tissue. This depth is achieved with the highest energies available in clinical linear accelerators, which typically reach 22 MeV (Khan, 2003).

The main characteristic of electron beams in radiotherapy is their controlled dose deposition and an abrupt dose drop after reaching a specific depth. This makes them ideal for treating superficial or near-skin tumors, such as skin cancer, chest wall tumors after mastectomy, and superficial lymph nodes. The major advantage is the ability to spare deeper-lying healthy tissue. In Figure 2.1 it is possible to see the percentage depth dose for 6 MeV, 12 MeV and 22 MeV electron beams (Khan, 2003).

The depth an electron beam can reach in tissue is directly related to its initial energy, with the "practical range" being the maximum depth at which the electrons penetrate. The effective therapeutic dose, however, is delivered at depths slightly shallower than the practical range. For example, the depth at which 90% of the maximum dose is deposited (R_{90}), a clinically relevant parameter, is shallower than the practical range. For a 22 MeV beam, the R_{90} is approximately 6 cm (Khan, 2003).

The premise that the use of significantly high-energy electrons could circumvent the limitations of conventional radiotherapy emerged in studies about twenty years ago. This hypothesis catalyzed investigations into VHEE, in the 50 to 400 MeV range, and led to the concept of a new therapeutic approach, VHEE radiotherapy. This technique was designed to enable the effective treatment of deep tumor targets, overcoming the limited reach of low-energy beams (Panaino et al., 2025). Some physical and dosimetric properties, as well as focused VHEE and FLASH-RT using this type of beam, will be discussed below.

2.1.1 Properties of VHEE Beams

The characterization of the longitudinal dose profile of VHEE beams was notably advanced by pioneering studies in the early 2000s, which underscored their clinical potential. Dosime-

Figure 2.1: Comparison of depth-dose curves measured with a diode and an ion chamber.

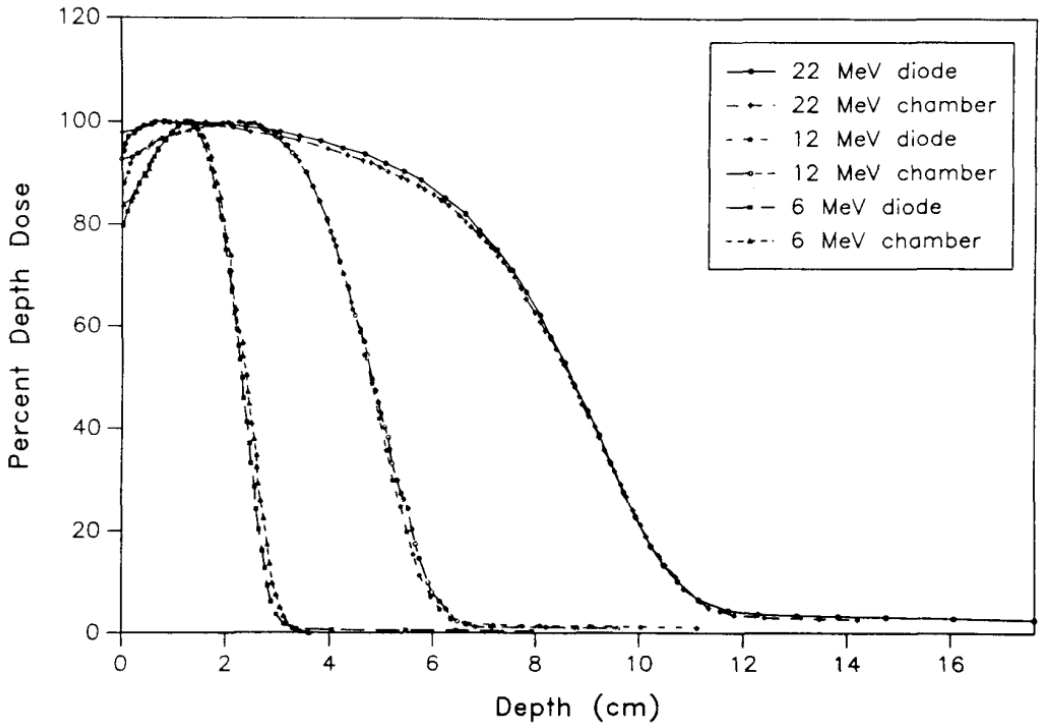

Source: (Khan, 2003)

try along the beam's propagation axis is defined by crucial parameters, including the depth of maximum dose (d_{max}), the proximal fall-off (PFO, at 90% of d_{max}), and the therapeutic range (TR, also at 90% of d_{max}) (Panaino et al., 2025). For an ideal, parallel, and collimated beam, the depth-dose curve is segmented into three distinct regions: an initial build-up zone, where the dose increases from the surface to the PFO; a therapeutic dose plateau, which extends from the PFO to the TR with doses exceeding 90% of the maximum; and finally, a region of ballistic fall-off, where the dose decreases abruptly after the TR. Figure 2.2a shows this characteristics. The clinical strategy consists of positioning the tumor volume entirely within the dose plateau, with the build-up and fall-off regions being as steep as possible to maximize the sparing of the skin and adjacent healthy tissues (Panaino et al., 2025). Subsequent studies, demonstrated that both the PFO and the TR deepen with increasing energy and field size, ensuring robust and adequate penetration. As an example, a 250 MeV beam with a 15×15 cm^2 field can generate a peak dose region that extends up to 40 cm in depth. In contrast, for divergent beams, the PFO shifts closer to the surface and the TR exhibits less dependence on energy or field size, resulting in therapeutic ranges inferior to those observed in collimated beams (Panaino et al., 2025).

In the transverse plane, the dose distribution is primarily characterized by the lateral penumbra (LP, the distance between the 90% and 20% isodose lines) and the beam width (BW, the width at the 90% isodose line at a given depth), which can be seen in Figure 2.2b, c, and d. Generally, the lateral penumbra of VHEE beams widen with depth due to multiple scattering,

being more gradual at shallow depths for energies above 100 MeV and increasing considerably at greater depths. Beam broadening (divergence), on the other hand, is significantly attenuated with increasing energy and, more discreetly, with a reduction in field size. When compared to those of photon beams, VHEE penumbra are sharper (narrower) at depths less than 5 cm but wider at depths greater than 10 cm, although, in absolute terms, the lateral scattering of VHEE is lower at great depths. The behavior of the beam width (BW) also differs according to the configuration: for collimated beams, the BW decreases with depth, whereas for divergent beams, it widens at the phantom entrance, an effect that is subsequently counteracted by the predominant scattering at depth (Panaino et al., 2025).

Figure 2.2: The depicted dose distributions result from a 200 MeV, 1 cm diameter parallel VHEE beam, which is collimated and impinges on a water phantom. The longitudinal dose distribution along the beam's central axis is presented in (a), indicating the depth of maximum dose (d_{max}), the proximal fall-off (PFO), and the therapeutic range (TR), with the latter two defined at the 90% dose level. The transverse dose distributions are shown at three distinct depths: (b) d_{max}, (c) 20 cm, and (d) 30 cm. In these profiles, the lateral penumbra (LP) is defined as the spatial distance between the 90% and 20% isodose lines, while the beam width (BW) corresponds to the full width at the 90% isodose contour at that depth.

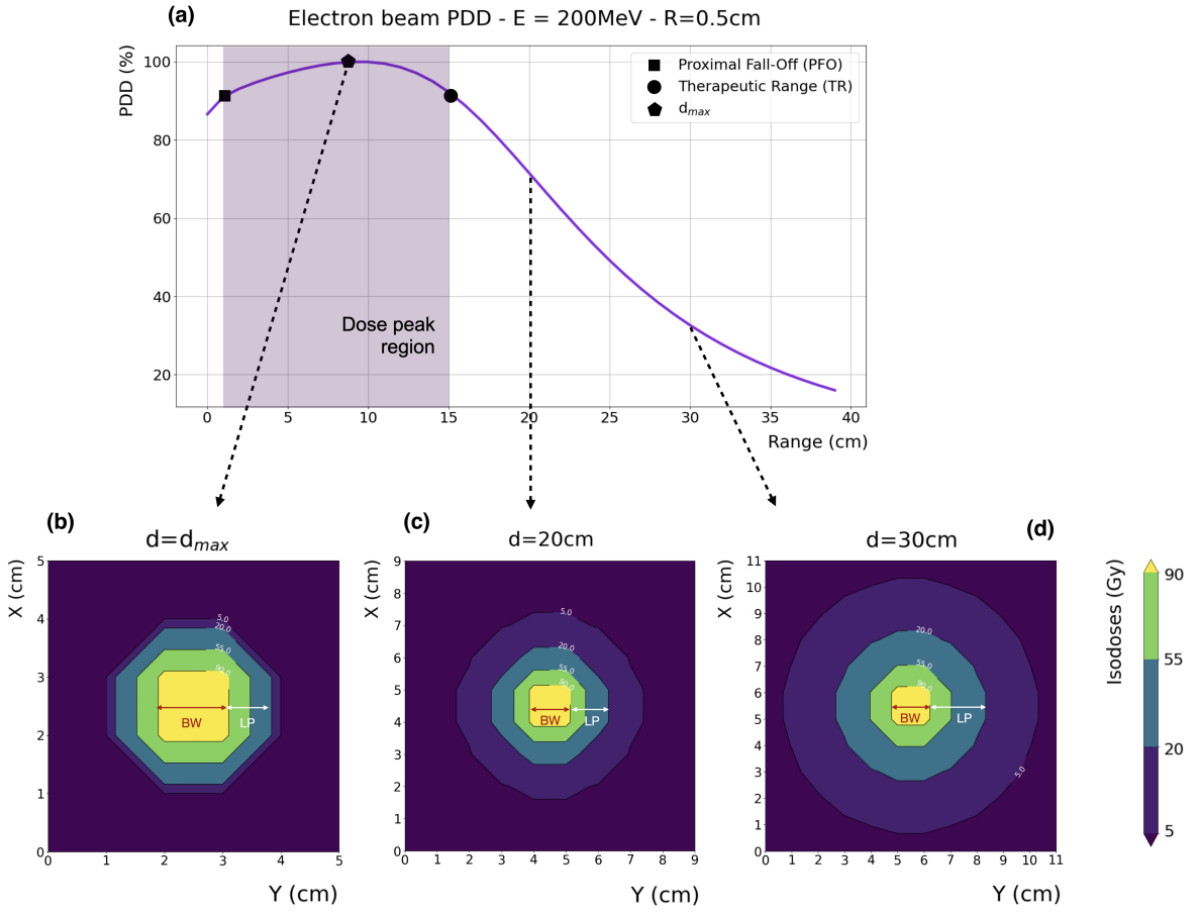

Source: (Panaino et al., 2025)

The dose deposited at the surface is a critical parameter that varies with the beam configura-

tion. For a collimated beam, the relative surface dose decreases with increasing energy and/or field size, potentially reaching values on the order of 66% of the maximum dose for a 250 MeV, 10×10 cm^2 beam (Panaino et al., 2025). In contrast, divergent beam configurations result in substantially higher surface doses, typically between 90% and 95% of the maximum dose. This implies that the skin-sparing potential for a single VHEE field is inferior to that of a single photon field, which can exhibit surface doses of 20% or less. However, this disadvantage can be effectively mitigated by the implementation of magnetic focusing systems (e.g., quadrupoles) or by the use of multiple-beam arrangements. The application of multiple converging fields drastically reduces the entrance dose; for example, the relative surface dose can be reduced to less than 50% with two orthogonal beams and to less than 30% with a four-beam arrangement (Panaino et al., 2025).

The intrinsic characteristic of VHEE of maintaining electron balance confers superior dosimetric resilience to tissue heterogeneity and changes in the patient's anatomy (Panaino et al., 2025). This robustness makes this technique a particularly promising alternative for the treatment of neoplasms located in anatomically inhomogeneous regions.

Figure 2.3 shows the effects of inhomogeneities on dose, comparing how different types of radiation (VHEE, protons, and photons) interact with an air cavity within a water phantom. For protons, the primary concern is a perturbation of the Bragg peak, leading to its distal shift and potentially undesired dose deposition in healthy tissues located beyond the target volume. In the case of photons, the interaction with low-density inhomogeneities, such as air cavities, can result in a localized dose build-up distal to the inhomogeneity, altering the planned dose distribution. In contrast, VHEE demonstrate a notable insensitivity to these low-density media. This characteristic allows for more predictable and precise dose delivery, as the dose distribution remains largely unperturbed by internal inhomogeneities.

The ability to perform efficient electromagnetic (EM) scanning is facilitated by the high charge-to-mass ratio of electrons, which is 1836 times greater than that of protons. This results in a magnetic rigidity that is 3 to 4 times lower, allowing electrons to be accelerated and steered by magnetic fields of substantially lower intensity. The practical consequence is the possibility of designing treatment systems that are more compact, less complex, and more economical, with a reduced technological footprint. EM scanning enables precise and dynamic control over dose delivery, making advanced techniques such as intensity-modulated VHEE therapy (IM-VHEET) feasible. Despite these advantages, the high susceptibility of electrons to the Lorentz force represents a challenge for integration with magnetic resonance imaging (MRI) systems. Nevertheless, innovative solutions, such as the MR-guided parallel-beam VHEE concept, have already been proposed to circumvent beam deflection and enable MRI guidance in the future (Panaino et al., 2025).

Considering radiobiological aspects, a study has already performed a comprehensive evaluation of laser-driven VHEE beams in vitro, ex vivo and in vivo models, directly comparing their effects with conventional intermediate energy electron (CIEE) generated by a clinical lin-

ear accelerator (LINAC). The findings consistently demonstrate that VHEE irradiation elicits biological responses comparable to those observed with CIEE, showing similar radiosensitivity in human fibroblasts (MRC5-hTERT) with no significant difference in D_{10} values ($p = 0.7$), equivalent dose-dependent reductions in cell proliferation in mouse precision-cut lung slices (PCLS) ($p \geq 0.99$) , and comparable morphological developmental toxicity in zebrafish embryos, including body shortening and spinal curvature alterations ($p \geq 0.495$) (Giaccaglia et al., 2025). These results highlight the potential of VHEE beams generated by laser plasma accelerators (LPA), supporting their future clinical translation in radiotherapy.

Figure 2.3: Dose maps of VHEE, proton and photon beams ($\sigma = 5$ mm) in a $30 \times 30 \times 30$ cm^3 water phantom with an air cavity placed at depth $d = 10$ cm and radius $r = 1$ cm.

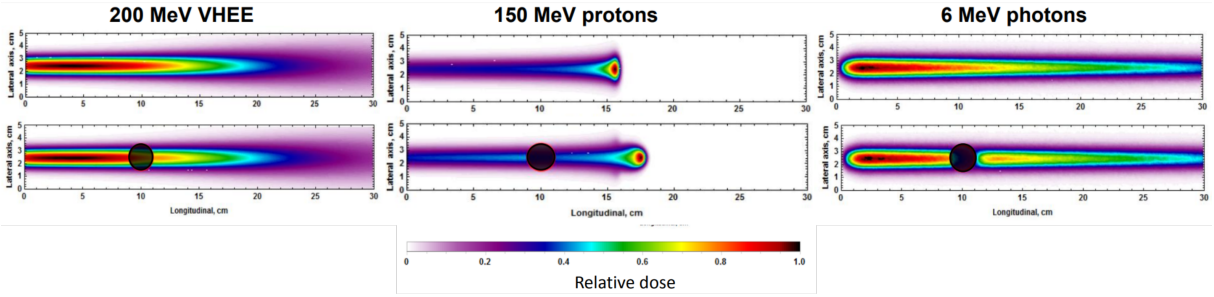

Source: (Agnese Lagzda, 2017)

2.1.2 Focused VHEE

A common theme across the research is the crucial role of magnetic fields, specifically quadrupole magnets, in precisely controlling VHEE beam characteristics, from deflection and scattering for homogeneous dose distribution to focused delivery at specific depths. The studies consistently report the significant benefits of VHEE focusing in reducing entrance and exit doses while concentrating energy at the tumor, thereby enhancing healthy tissue sparing compared to conventional radiotherapy techniques (Panaino et al., 2025; Kokurewicz et al., 2019). Figure 2.4 shows the percentage on-axis depth-dose (PDD) curves of diferent types of radiation in a water phantom. This figure illustrates that focused delivery results in a reduced radiation dose to surrounding healthy tissue. Curves **g** and **h** indicate that the beams achieve highly localized dose deposition at the target depth of 15 cm.

2.1.3 FLASH Radiotherapy with VHEE Beams

The primary distinction between FLASH-RT and conventional radiotherapy (CONV-RT) used in clinical practice lies in the magnitude of the dose rate delivered. While a mean dose rate of 0.01 Gy/s is typical for CONV-RT, for FLASH-RT a mean dose rate of at least 40 Gy/s is required (Bourhis et al., 2019), that is, it is defined by the administration of radiation doses at ultra-high dose rates (UHDRs). Consequently, with a higher dose rate, the time required for

Figure 2.4: PDD curves of diferent types of radiation in a water phantom. **(a)** 6 MV Photons, **(b)** Bragg peak 147 MeV protons, **(c)** spread-out Bragg peak, **(d)** 10 MeV electrons, **(e)** collimated 200 MeV electrons, **(f)** collimated 2 GeV electrons, **(g)** 200 MeV electrons focused at 15 cm, **(h)** 2 GeV electrons focused at 15 cm.

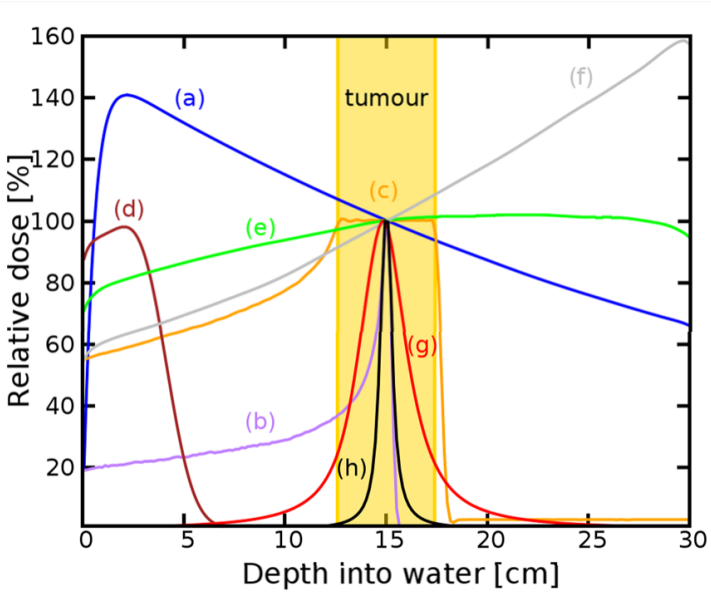

Source: (Kokurewicz et al., 2019)

dose delivery is drastically reduced in the new modality, potentially delivered in milliseconds, which is appealing in clinical practice as it enhances accuracy by minimizing intrafractional motion (Jaccard et al., 2018).

To trigger the FLASH effect, the beam should ideally be pulsed at a frequency of approximately 100 Hz, with a dose per pulse $\geq$ 1 Gy and an intra-pulse dose rate $\geq 10^6$ Gy/s (Panaino et al., 2025). This allows the total treatment time for FLASH-RT to range from microseconds to hundreds of milliseconds, unlike the several minutes required for a CONV-RT treatment. The primary benefit of FLASH-RT is its ability to reduce toxicity in normal tissues while maintaining antitumor efficacy, making it promising for radioresistant tumors or for sites where conventional radiotherapy would cause significant damage to healthy tissues (Panaino et al., 2025).

Historically, the feasibility of UHDR was first evaluated with low-energy electrons. The Kinetron and the Oriatron eRT6 are notable examples of experimental electron systems that offer FLASH irradiation, with the Oriatron eRT6 having been used in the first FLASH-RT treatment of a patient with cutaneous lymphoma in 2019. Efforts have also been made to adapt clinical low-energy accelerators for FLASH-RT experiments (Panaino et al., 2025).VHEE FLASH-RT is considered an exceptional treatment solution as it combines the normal tissue-sparing capability of FLASH with the unique dosimetric advantages of VHEET. However, the development of VHEE FLASH-RT systems, much like VHEE systems for CONV dose rates, is still limited to a few research infrastructures. Recent research focuses on radiobiological eval-

uations of VHEE beams at UHDR and the development of new dosimeter concepts capable of withstanding UHDR.

Studies indicate that the treatment time with IM-VHEET (intensity-modulated VHEE radiotherapy) can be potentially shorter than that of photon therapies. For example, a 100 MeV VHEE dose rate was estimated at approximately 117 Gy/s, which theoretically makes it compatible with FLASH applications for large treatment doses in sub-second times, ignoring scanning time. However, IM-VHEET may require an extended delivery time, which could reduce or eliminate the FLASH effect. To trigger the FLASH effect in a 1 L volume, a single beam of approximately 2500 VHEE pencil beams with 2 mm spacing would need to be delivered in 100 ms, requiring a minimum repetition rate of 25 kHz, which current systems cannot meet (Panaino et al., 2025).

In this context, the 3D-CRT VHEET and transmission VHEET (TR-VHEET) treatment modalities are considered for their ease of transition to FLASH conditions. 3D-CRT VHEET has demonstrated the potential to deliver dose distributions competitive with IMRT in brain and lung cancer, and the increased biological selectivity of FLASH may compensate for or even surpass the dosimetric quality of IMRT, especially at the GTV (Gross Tumor Volume)-PTV (Planning Target Volume) margins (Panaino et al., 2025). TR-VHEET, where the patient's tissue is irradiated with the beam section near the Bragg peak and the peak itself is kept outside the patient, also shows promise, with TR-VHEET plans in the 150-250 MeV range offering acceptable dosimetric quality compared to TR-PT (transmission proton therapy) plans (Panaino et al., 2025).

The application of dose modifying factors (DMF) or their inverses, FLASH modifying factors (FMF), has been evaluated for IM-VHEET plans at UHDR (Panaino et al., 2025). A DMF of 0.8 (FMF of 1.25) may allow an 80 MeV IM-VHEET plan to theoretically compete with IMRT and could improve PTV coverage when constrained by dose limits in OARs. VHEET-based GRID therapy has also been modeled at UHDR, showing that the open-beam modality can have UHDRs above 40 Gy/s in most OARs, whereas the multi-GRID modality may have dose-rate peaks at UHDR but lower volume-weighted average dose rates (Panaino et al., 2025). Studies on the total treatment time (TTT) under FLASH-UHDR conditions with VHEE indicate that minimum beam intensities are required to achieve FLASH conditions in most of the PTV volume, and that higher VHEE energies result in higher dose rates and, consequently, shorter delivery times (Panaino et al., 2025).

From a radiobiological standpoint, initial investigations of the FLASH effect in VHEET have focused on the irradiation of pBR322 plasmids and cells in suspension. Although some early studies did not observe statistically significant variations in the yield of double-strand breaks (DSB) with dose rate, others, by increasing the concentration of hydroxyl radical scavengers to simulate a cell-like environment, observed a notable reduction in single-strand breaks (SSB) from CONV to UHDR, providing evidence of the FLASH effect with VHEE irradiation (Panaino et al., 2025). In vitro experiments have also shown a differential response of tumor

and normal cells to UHDR VHEE irradiation, with less impact on non-cancerous cells.

In summary, VHEE FLASH-RT represents a significant advancement, uniting the dosimetric precision of VHEET with the healthy tissue-sparing capacity of the FLASH effect. However, its clinical implementation requires advances in more compact and stable accelerators, treatment planning systems that consider time-dependent parameters, accurate dosimeters capable of withstanding UHDR, and a deeper understanding of VHEE-FLASH radiobiology. The higher charge-to-mass ratio of electrons, which results in lower magnetic rigidity, allows for more compact and economical VHEE systems. This is a crucial advantage for FLASH-RT, facilitating multi-directional beams at UHDR within the required time constraints (Panaino et al., 2025).

2.2 Laser-Plasma Acceleration (LPA)

Laser Plasma Accelerators (LPAs) were proposed by Tajima and Dawson in 1979 (Tajima and Dawson, 1979; Esarey et al., 2009). Their pioneering efforts established the groundwork for the development and investigation of plasma-based particle accelerators powered by either lasers or particle beams. Dawson's contributions significantly propelled the field of plasma accelerators, facilitating the advancement and application of this innovative technology (Esarey et al., 2009). LPAs employ high-intensity laser pulses to induce ultra-high acceleration gradients in plasma, enabling the rapid acceleration of particles to extremely high energies over significantly shorter distances compared to conventional accelerators (Bingham and Trines, 2016).

LPAs can achieve high acceleration gradients, on the order of GV/m, surpassing traditional accelerators by several orders of magnitude. These high acceleration gradients enable particles to attain high energies over significantly shorter distances. To ensure efficient acceleration in LPAs, the laser pulse duration should be comparable to or shorter than the plasma wavelength. This condition prevents the re-absorption of energy in the plasma wave by the trailing part of the laser pulse, thus exciting wakefields with a phase velocity equal to the laser group velocity. LPAs have the potential to transform particle acceleration and find applications in diverse fields such as high-energy physics, medical science (cancer therapy), and industrial applications (Bingham and Trines, 2016; Wenz and Karsch, 2020).

LPAs utilize high-power laser pulse with a relativistic intensities exceeding 10^{18} W/cm^2 in a gaseous medium. Figure 2.5 shows an intense laser reaching a gaseous target, transforming it into an underdense plasma, since the atoms in the target gas are ionized. As the high-intensity laser pulse travels through a low-density plasma, the electrons are displaced while the ions remains stationary due to the transmission of a ponderomotive force arising from the laser's intensity gradient in a tightly focused beam. The electrons are expelled and return to the laser axis repeatedly, due to the high electrostatic field induced by charge separation, causing periodic modulations of electron density following the laser pulse, known as a plasma wave or Langmuir wave, as represented in Figure 2.5. For a given plasma density, the normalized vector potential

a_0, also known as the laser strength parameter, and the laser pulse duration will define the LPA operation regime, and thus the shape of the plasma wave. A Particle-in-cell (PIC) simulation artwork of laser wakefield electron acceleration is shown in Figure 2.6.

Figure 2.5: Basic physical process of LWFA

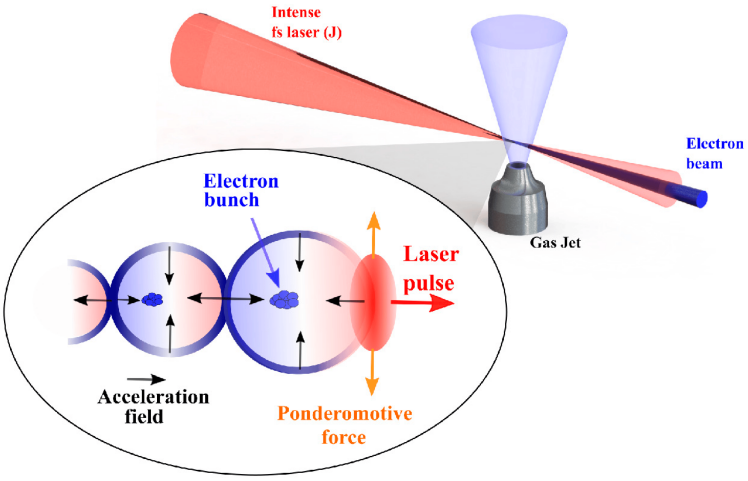

Source: (Kim et al., 2021)

Figure 2.6: Laser pulse, wakefield, and accelerated electron bunch in a LPA. The laser pulse propagates in an underdense plasma, generating a strong longitudinal electric field, the wakefield. When electrons are trapped within the accelerating region of the electric field, their energy is boosted to high values over very short distances.

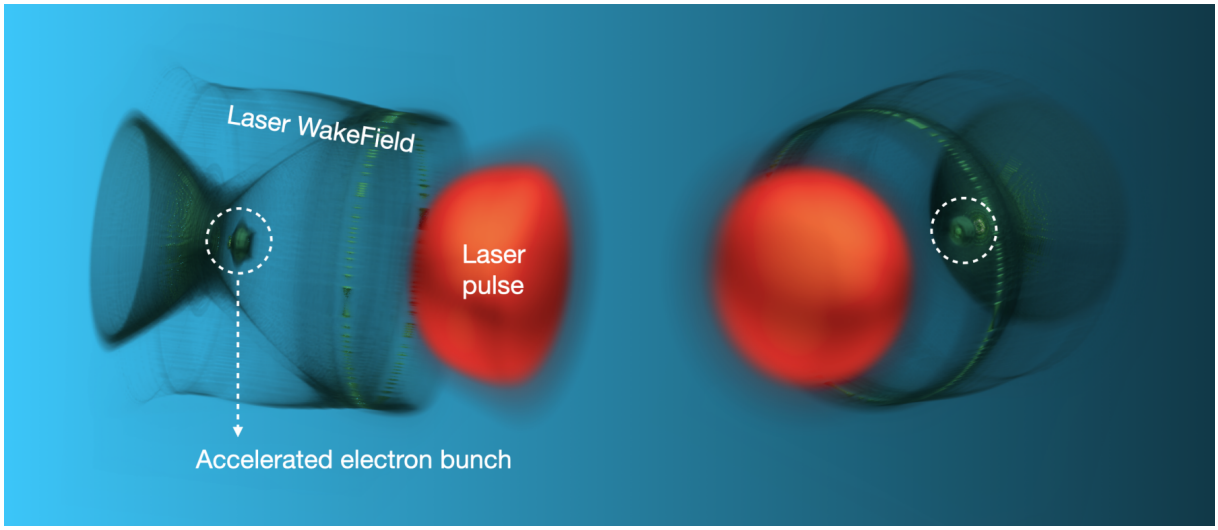

Source: (Panaino et al., 2025)

2.2.1 Bubble regime

The bubble regime of electron acceleration in ultra-relativistic laser-plasma interactions involves the formation of a distinct "bubble" structure in the plasma behind an intense laser pulse

when $a_0 > 1$ and the pulse duration is shorter than half the plasma period (Kim et al., 2021), with several key features. Firstly, instead of the typical periodic plasma wave, this regime forms a cavity devoid of cold plasma electrons, which is characteristic of the bubble regime. Within this cavity, a dense bunch of relativistic electrons with a monoenergetic spectrum is self-generated, essential for high-quality electron beam production. The laser pulse can propagate long distances in the homogeneous plasma without significant diffraction, aiding in high-energy particle acceleration. Additionally, the bubble regime enables the self-generation of electron beams with unique properties, such as quasi-monoenergetic energy spectra, and does not require a preformed plasma channel for laser pulse guidance, as the bubble itself can effectively guide the laser pulse (Pukhov et al., 2004).

Overall, the bubble regime presents a promising approach to electron acceleration in ultra-relativistic laser-plasma interactions, distinguished by its unique features compared to traditional acceleration methods. By leveraging the specific conditions and dynamics within the bubble regime, including cavity formation, electron sheath development, and efficient trapping mechanisms, the process culminates in the production of ultra-short dense bunches of electrons with quasi-monoenergetic energy spectra (Pukhov et al., 2004).

2.2.2 Gas mixture choice

In the context of LWFA, ionization injection is a specialized technique employed to facilitate electron trapping at a precise position along the laser-plasma interaction path. For high-quality and stable beams, controlled injection methods are preferred over inherently unstable self-injection via wave breaking (Kirchen et al., 2021). This method typically utilizes a gas target composed of a helium and nitrogen (He + N_2) mixture (Maldonado et al., 2023; Labate et al., 2020a). As the laser pulse propagates through this medium, its leading edge is intense enough to ionize all of helium's electrons and the first five electrons of nitrogen, thereby creating a background plasma in which a nonlinear wakefield is excited (Maldonado et al., 2023). The crucial injection mechanism occurs subsequently, near the laser's focal point where the pulse intensity reaches its maximum. At this location, the intense field induces tunneling photoionization of the remaining core electrons from the N^{5+} ions (Maldonado et al., 2023). This secondary ionization event releases a new population of electrons directly into the established wakefield, and a trapped bunch may be formed if these electrons reach phase velocity before being overtaken by the wakefield structure. Thus, nitrogen acts as an injector species, enabling a controlled release of electrons into the accelerating phase of the wakefield.

While quasi-monoenergetic electron beams were observed in a N_2 + 50% He mixture (Hazra et al., 2019), the primary acceleration mechanisms in those specific experimental conditions were attributed to direct laser acceleration (DLA) or a hybrid (DLA + wakefield) mechanism, rather than the classical bubble regime (Hazra et al., 2019). The study highlights that the contribution of DLA cannot be ignored when the laser pulse significantly overlaps with the injected electrons (Hazra et al., 2019).

The mixture of H_2 + N_2 is highly suitable for an LPA operating in a bubble-like (blowout) regime with controlled ionization injection (Kirchen et al., 2021). The H_2 base ensures that the drive laser pulse experiences minimal distortion from ionization, allowing it to form a strong and stable wakefield (Kirchen et al., 2021). The addition of a small percentage of N_2 (e.g., 10%) acts as a dopant, enabling localized ionization injection of electrons at specific phases of the wakefield (Kirchen et al., 2021). This controlled injection, combined with optimal beam loading, allows for flattening of the accelerating fields along the electron bunch (Kirchen et al., 2021). Experimental results with a 90% H_2 + 10% N_2 mixture demonstrated low energy spread (1.2% rms), high charge (44 pC), and a high estimated energy-transfer efficiency ($\sim$ 19%) (Kirchen et al., 2021). This approach significantly improves beam quality and stability by reducing correlated energy spread and managing shot-to-shot fluctuations related to laser parameters (Kirchen et al., 2021).

Given that He still induces more ionization distortions on the laser pulse than H_2, particularly for few-cycle pulses (Monzac et al., 2024), H_2-based mixtures are generally favored for achieving optimal conditions for the bubble regime that relies on a clean, undistorted drive pulse. However, hydrogen is a flammable gas with a flammability range in air of 4% to 75% by volume and a low minimum ignition energy, being an exceptionally broad range compared to other fuels, increasing the likelihood that a leak will result in a flammable mixture (Ring et al., 2008). It takes less than 7% of the energy needed for natural gas to ignite a hydrogen-air mixture, meaning that a simple electrostatic discharge, like the spark from touching a doorknob, can be sufficient to inflame (Ring et al., 2008; Hathaway et al., 1999). Contrariwise, He safety profile is fundamentally different, since it is a chemically inert, non-toxic, and non-flammable noble gas (New Jersey Department of Health, 2006). Therefore, selecting helium as the plasma source offers a more favorable safety profile, minimizing operational hazards.

2.3 Particle-in-cell Simulations

The laser-plasma interaction in the laser wakefield acceleration (LWFA) regime is characterized by strong nonlinearity (Brigren and Hallborn, 2021; Jalas et al., 2021). The laser pulse shapes the plasma, while the plasma, in turn, guides and modifies the laser, establishing a complex feedback loop. The process of electron self-injection into the wakefield's "bubble" structure and its subsequent acceleration is a kinetic phenomenon whose complexity eludes a complete analytical description. In this case, theoretical models are insufficient to capture the full dynamics of the system. For this reason, high-fidelity numerical simulations are more than verification tools; they are essential instruments for the discovery, design, and optimization of LWFA experiments (Jalas et al., 2021). The ability to perform large-scale parameter sweeps and machine learning-guided optimizations elevates the simulation from a post-hoc analysis tool to a cornerstone of predictive design. This paradigm shift directly accelerates experimental discovery and reduces the operational costs of high-power laser facilities.

In PIC simulations, discrete "packets" of charge and mass are utilized to represent particles, and their movements are determined by Newton's laws of motion while they interact with electric and magnetic fields, described by Maxwell's equations (Brigren and Hallborn, 2021; Birdsall and Langdon, 2004). The PIC algorithm, depicted in Figure 2.7 (Nunes, 2023), enables the investigation of energy exchange between particles and fields, facilitating the comprehension of phenomena like electron acceleration through laser-plasma interactions.

Figure 2.7: Loop of a PIC code. The charge and current densities are calculated from the position and speed of the macroparticles. They are used in calculations of the electric field and magnetic flux density. Finally, the Lorentz force is calculated, which is applied to Newton's second law, to update the positions and velocities of the macroparticles.

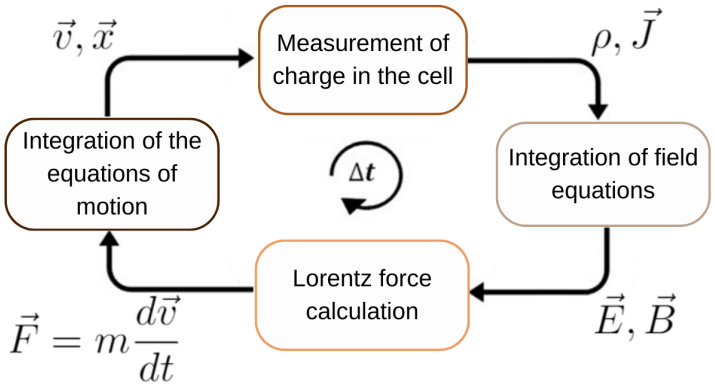

Source: (Nunes, 2023)

2.4 Modelling and Optimization

2.4.1 Bayes Theorem

The described plasma dynamics highlight the complexity of a system resulting from the interaction between a high-energy laser and plasma. Predicting the optimal input parameters for electrons accelerated in this process is both desirable and challenging when using exhaustive methods. In such cases, Bayesian inference can be particularly advantageous. This approach is especially useful for making inferences when investigating unique data, where empirical (or frequentist) probability is not available, meaning that the events are not repetitive in nature. The Bayes Theorem is given by

$$P(H|E) = \frac{P(E|H)P(H)}{P(E)}, \tag{2.1}$$

where $P(H|E)$ is often defined as the *posterior probability of* H, and represents the probability of hypothesis H being true given the evidence E. $P(H)$ is termed as *prior probability of hypothesis* H, being the initial belief in the hypothesis before considering the evidence. The likelihood of

the evidence E occurring given that the hypothesis H is true is denoted by $P(E|H)$. Finally, $P(E)$ provides the probability of the evidence E occurring regardless of the hypothesis, and is known as *the total probability* of the evidence.

Considering the experimental scenario with lasers and plasma, it is possible to specify a procedure for generating observations (including noise ε), represented by a model $\mathscr{M}$, which relates input variables, given by $\mathbf{x}$, to observations, delineated by y (Brigren and Hallborn, 2021). This model is composed of the target function and a noise term:

$$\mathscr{M} : y(\mathbf{x}) = f(\mathbf{x}) + \varepsilon. \tag{2.2}$$

To inference about these quantities, it is possible to use the Bayes theorem explored before. So, using *prior probability distributions*, the prior knowledge about both $f(\mathbf{x})$ and ε are included in the model concept (Brigren and Hallborn, 2021). The following equation represents a probability for the model given the observations $\mathbf{y} = \{y_i\}_{i=1}^{n}$ and corresponding inputs $\{y_i\}_{i=1}^{n}$ as

$$P(f, \varepsilon|\mathbf{y}) = \frac{P(\mathbf{y}|f, \varepsilon)P(f, \varepsilon)}{P(\mathbf{y})}, \tag{2.3}$$

where the joint probability distribution for the quantities given the observations is represented by $P(f, \varepsilon|\mathbf{y})$.

Parametric models assume that data distributions can be described using a finite set of parameters. Consequently, the flexibility or complexity of these models is bounded by the number of parameters employed in regression analyses. Given that the function $f(\mathbf{x})$ is treated as a black-box type function, in other words the objective function and/or the constraints defining the set is unknown, this study employs a non-parametric regression approach, specifically a Gaussian Process, to model $f(\mathbf{x})$. This treatment maintains $f(\mathbf{x})$ as an abstract entity, representing a probability distribution of functions (Wang, 2020; Brigren and Hallborn, 2021).

2.4.2 Mathematical Background

Gaussian Processes

Gaussian processes (GPs) are prevalent in the field of machine learning, particularly in supervised learning applications. They serve as probabilistic frameworks utilized for tasks such as regression and classification. In regression, an algorithm predicts an output value based on existing data. Gaussian Process Regression (GPR) leverages this concept by making predictions while incorporating prior knowledge, which is encapsulated in kernels. GPR not only provides predictions but also quantifies the uncertainty associated with these predictions (Wang, 2020; Nunes, 2023), being used as the prior probability distribution of functions $f(\mathbf{x})$.

The goal of regression is to model a function based on a set of observed data, enabling the representation of these data points and the prediction of outcomes for new, unknown data

points. GPR provides not only the expected values for the function but also the respective standard deviations. This feature allows for the generation of an infinite number of functions that can be fitted to a given set of observed data, considering a desired confidence interval. In essence, GPR performs regression by establishing a probability distribution over this infinite set of functions. The mean of this distribution represents the most probable characterization of the data (Wang, 2020). In GPR, an optimal fit is characterized by a smooth distribution curve without abrupt changes. This implies that for two closely spaced points in the input set x_i and x_{i+1}, the corresponding functions values $f(x_i)$ and $f(x_{i+1})$ should be similar, indicating a relationship between them. This smoothness property implies that the curve should follow a multivariate normal distribution, defined by its probability density as follows:

$$P(\mathbf{x}) = \frac{e^{-\frac{1}{2}(\mathbf{x}-\mu)^T \mathbf{K}^{-1}(\mathbf{x}-\mu)}}{(2\pi)^{N/2} \mid \mathbf{K} \mid^{1/2}}, \tag{2.4}$$

where N is the number of dimensions, $\mathbf{x}$ is the input data, μ is the mean of the distribution, and $\mathbf{K}$ is the covariance matrix, which determines how these data relate to each other. The notation that represents the multivariate distribution of dimension $\mathscr{N}$ is

$$\mathscr{N}(\mu, \mathbf{K}) \sim \mathscr{N}\left(\begin{pmatrix}\mu_1\\ \mu_2\\ \mu_3\end{pmatrix}, \begin{pmatrix}K_{11} & K_{12} & ... & K_{1N}\\ K_{21} & K_{22} & ... & K_{2N}\\ K_{N1} & K_{N2} & ... & K_{NN}\end{pmatrix}\right), \tag{2.5}$$

where $\mathscr{N}$ represents a multivariate Gaussian distribution.

The definition of the covariance matrix K, which is of size NxN in the notation discussed above, stands out as one of the key parameters in GPR. The entries of this matrix quantify the relationships between variables, such as x_i and x_j. It is expected that when points are closely spaced, such as x_i, x_{i+1}, and x_{i+2}, the elements $K_{i(i+1)}$ and $K_{i(i+2)}$ are numerically similar, indicating a strong relationship. Conversely, when points are far apart, the coefficients are expected to approach zero. Therefore, the covariance matrix not only describes the distribution's shape but also governs the characteristics of the function being predicted (Wang, 2020; Nunes, 2023). Figures 2.8(a) and 2.8(b), 2.8(c) and 2.8(d), and 2.8(e) and 2.8(f) represents, respectively, the following three matrices: $\mathbf{K} = \begin{pmatrix}1 & -0.8\\ -0.8 & 1\end{pmatrix}$, $\mathbf{K} = \begin{pmatrix}1 & 0\\ 0 & 1\end{pmatrix}$, and $\mathbf{K} = \begin{pmatrix}1 & 0.8\\ 0.8 & 1\end{pmatrix}$.

Various functions, referred to as kernels or covariance functions, can be employed to define the elements of the covariance matrix. A kernel operates on two points, computing a scalar that represents the similarity between these points. Consequently, the kernel, by describing the similarity between function values, dictates the possible forms a fitted function can assume. Examples of kernels found in the literature include the White Noise Kernel (WNK), Radial Basis Function (RBF), Rational Quadratic Kernel (RQK), Periodic Kernel (PK), and Matérn Kernel (MK) (Nunes, 2023). Each of these kernels is characterized by its specific parameters. The RBF kernel is commonly regarded as the standard in GPR and is defined as:

Figure 2.8: Examples of three bivariate Gaussian distributions with zero mean

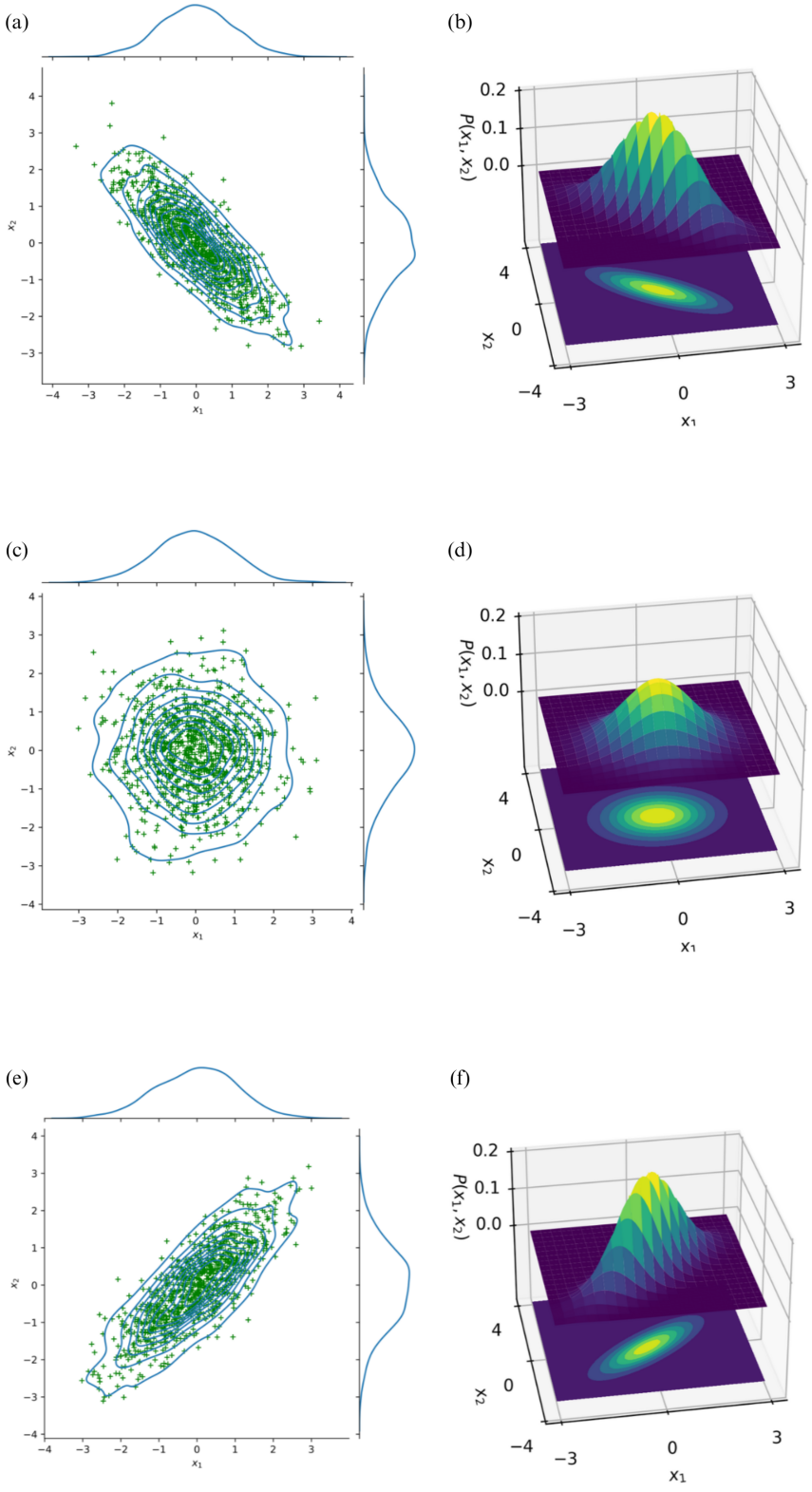

Source: author

$$K_{ij} = \sigma^2 e^{-\frac{\|x_i - x_j\|}{2l^2}}, \tag{2.6}$$

where σ^2 is the variance, and l is the length determining the influence range on neighbors. When we increase this last parameter, points further away from each other become more correlated.

A regression function modeled by a multivariate normal distribution given input data x is expressed as

$$P(\mathbf{f}|\mathbf{x}) = \mathcal{N}(\mathbf{f}|\mu, \mathbf{K}), \tag{2.7}$$

where $\mathbf{f}$ is a vector of the target function values given the input data $\mathbf{x}$, so $\mathbf{f} = [f(x_1), f(x_2), ..., f(x_N)]$. Considering a scenario where is desirable to make predictions of new data points x_*, we can express the joint probability distribution of $\mathbf{f}$ and $\mathbf{f}_*$, being $\mathbf{f}_* = \mathbf{f}(\mathbf{x}_*)$, as

$$\left[\begin{pmatrix}\mathbf{f}\\ \mathbf{f}_*\end{pmatrix}\right] \sim \left[\begin{pmatrix}\mu(\mathbf{x})\\ \mu(\mathbf{x}_*)\end{pmatrix}, \begin{pmatrix}\mathbf{K} & \mathbf{K}_*\\ \mathbf{K}_*^T & \mathbf{K}_{**}\end{pmatrix}\right], \tag{2.8}$$

where $\mathbf{K} = K(\mathbf{x}, \mathbf{x})$, $\mathbf{K}_* = K(\mathbf{x}, \mathbf{x}_*)$, and $\mathbf{K}_{**} = K(\mathbf{x}_*, \mathbf{x}_*)$. Taking into consideration the fact that regressions demand conditional distribution, in this example being $P(\mathbf{f}_*|\mathbf{f}, \mathbf{x}, \mathbf{x}_*)$, and 2.8 is the joint distribution, the Marginal and Conditional Distributions theorem was used to derive 2.9 below from 2.8 (Wang, 2020). Considering $\mu(\mathbf{x}) = \mu(\mathbf{x}_*) = 0$, the result is

$$P(\mathbf{f}_*|\mathbf{f}, \mathbf{x}, \mathbf{x}_*) \sim \mathcal{N}(\mu_\star, \Sigma) \tag{2.9}$$

$$\mu_\star = \mathbf{K}_\star^T \mathbf{K}^{-1} \mathbf{f} \tag{2.10}$$

$$\Sigma = \mathbf{K}_{\star\star} - \mathbf{K}_\star^T \mathbf{K}^{-1} \mathbf{K}_\star \tag{2.11}$$

Likelihood and Marginal Likelihood

Considering measured data, the probability for measuring is going to depend on the target function (unknown) and the measurement error. Defining a vector of measured target function values $\mathbf{y} = [y_1, y_2, ..., y_n]^T$ and a vector of corresponding errors $\mathbf{e} = [\varepsilon_1, \varepsilon_2, ..., \varepsilon_n]^T$, then the measured data can be expressed as

$$\mathbf{y} = \mathbf{f} + \mathbf{e}. \tag{2.12}$$

The target function is modeled using GPR, which represents the distribution of $\mathbf{f}$ as $\mathbf{f} \sim \mathcal{N}(\mathbf{m}, \mathbf{K})$. If the vector $\mathbf{e}$ is considered Gaussian noise, then it is also distributed as a multivariate normal, $\mathbf{e} \sim \mathcal{N}(\mathbf{m}_\varepsilon, \Sigma_\varepsilon)$. Consequently, assuming $\mathbf{f}$ and $\mathbf{e}$ independent, the observed data $\mathbf{y}$ is the sum of two multivariate normal distributions, resulting in a normal distribution as well (Brigren and Hallborn, 2021). Thus, it can be concluded that the likelihood is a multivariate normal distribution given by $\mathbf{y} \sim \mathcal{N}\left(\mathbf{m} + \mathbf{m}_\varepsilon, \mathbf{K} + \sum_\varepsilon\right)$.

In determining appropriate estimates for the hyperparameters, denoted as θ, which param-

eterize the prior probability distributions for f and ε (e.g. lengthscale and noise variance), it is common practice to assess the marginal likelihood of 2.3, $P(\mathbf{y}|\theta)$. The marginal likelihood, also known as the evidence, represents the probability distribution over all possible data sets $\mathbf{y}$ given a data generation process that includes prior knowledge about the system (i.e., a model). It signifies the probability that randomly selected functions f and ε from the specified model class would produce the observed data $\mathbf{y}$ (Brigren and Hallborn, 2021), $P(\mathbf{y}|\theta)$.

It is possible to express the marginal likelihood in terms of an integral over the likelihood and the priors (Brigren and Hallborn, 2021) if we integrate the posterior in 2.3, $P(f,\varepsilon|\mathbf{y})$. The following equations describes this process

$$\int P(f,\varepsilon|\mathbf{y})dfd\varepsilon = \frac{1}{P(\mathbf{y})}\int P(\mathbf{y}|f,\varepsilon)P(f,\varepsilon)dfd\varepsilon = 1 \tag{2.13}$$

$$P(\mathbf{y}) = \int P(\mathbf{y}|f,\varepsilon)P(f,\varepsilon)dfd\varepsilon. \tag{2.14}$$

Since $\mathbf{y}$ depends on the model, which is defined by the hyperparameters, we can define 2.14 as following:

$$P(\mathbf{y}|\theta) = \int P(\mathbf{y}|f,\varepsilon)P(f,\varepsilon|\theta)dfd\varepsilon. \tag{2.15}$$

A commonly utilized approach for selecting appropriate hyperparameters based on the provided data is the process of identifying the model that best predicts the dataset, therefore the process of maximizing the marginal lilelihood with respect to θ. In full Bayesian analysis, hyperparameters are treated by incorporating prior knowledge about them through hyperpriors (Brigren and Hallborn, 2021). The hyperprios are expressed by $P(\theta)$, and it is added to the expression by extending the posterior to include $P(\theta)$, as in 2.16, and then marginalized over θ to yield the joint posterior for f and ε as in 2.15 as follows

$$P(f,\varepsilon,\varepsilon|\mathbf{y}) = \frac{P(\mathbf{y}|f,\varepsilon)P(f,\varepsilon)|\theta P(\theta)}{P(\mathbf{y})} \tag{2.16}$$

$$P(f,\varepsilon|\mathbf{y}) = \int P(f,\varepsilon,\theta|\mathbf{y})d\theta. \tag{2.17}$$

The marginal likelihood can be used for the *maximum a posteriori* (MAP) estimate, being a last computationally expensive approach than 2.17. This involves maximizing the posterior distribution of θ

$$P(\theta|\mathbf{y}) \propto P(\mathbf{y}|\theta)P(\theta). \tag{2.18}$$

The Posterior Distribution

The posterior can be calculated after fitting the hyperparameter given data and a model, representing our inferred knowledge and being used in the scenario where is desirable to make predictions about new data points y_p based on known data $\mathbf{y}$ (Brigren and Hallborn, 2021). The marginalization of the joint probability distribution $P(y_p, f, \varepsilon|\mathbf{y})$ can be used to express the probability about the new data points given the data. This reasoning is expressed below

$$P(y_p|\mathbf{y}) = \int P(y_p, f, \varepsilon|\mathbf{y}) df d\varepsilon = \int P(y_p|f, \varepsilon) P(f, \varepsilon|\mathbf{y}) df d\varepsilon. \tag{2.19}$$

We can get to the posterior predictive distribution similarly

$$P(f_p|\mathbf{y}) = \int P(f_p, f|\mathbf{y}) P(f|\mathbf{y}) df, \tag{2.20}$$

where $P(f|\mathbf{y})$ is the posterior in 2.17 marginalized over ε. Equation 2.20 denotes the posterior predictive distribution for the target function f and finds extensive application in the subsequent discussion of the Bayesian optimization algorithm (Brigren and Hallborn, 2021).

2.4.3 Bayesian Optimization

The process of a Bayesian Optimization algorithm can be succinctly summarized in two main steps: firstly, by modeling the objective function as a probability distribution of potential objective functions conditioned on data points, and secondly, by creating an acquisition function to guide the sampling process more efficiently than a random approach (Brigren and Hallborn, 2021). The term "optimization" refers to the goal of finding the optimal value of an objective function (i.e., a global maximum or minimum) among all possible values or determining the corresponding location of this optimum in a given environment. The search process commences at a specific location and employs a defined strategy to iteratively guide the selection of subsequent sampling locations, gather the corresponding observations, and update the strategy (Nunes, 2023). This strategy, according to (Brigren and Hallborn, 2021), can be express as the following sequence:

1. Evaluate target function at point $\mathbf{x}$ to get y;
2. Maximize the marginal likelihood conditioned on the new data points [y, $\mathbf{x}$] to get optimal hyperparameters;
3. Update the posterior distribution with the new hyperparameters;
4. Maximize the acquisition function based on the posterior distribution to get a new evaluation point $\mathbf{x}$.

Acquisition Functions

Various acquisition functions exist, each designed to balance the exploration of new points with the exploitation of known high-value regions. These functions are formulated to manage the trade-off between exploring new points with high predicted function values (exploitation) and exploring points with greater uncertainty to potentially capture the true function value (exploration) (Brigren and Hallborn, 2021).

Commonly used acquisition functions include those centered on improvement metrics, such as the improvement probability function, expected improvement function, and upper confidence bound function. When Gaussian processes are employed for the adjustment, these acquisition functions can be expressed as follows (Nunes, 2023):

- Improvement Probability function

$$x_{i+1} = \underset{x}{\text{argmax}} \Phi \left[\frac{\mu_i(x) - f(x^+) - \varepsilon}{\sigma_i(x)} \right], \tag{2.21}$$

  where $\Phi(A)$ is the cumulative distribution function, ε is a small positive number, x^+ is the point where the highest value for the objective function was estimated up to iteration i, and $\mu_i(x)$ and $\sigma_i(x)$ are, respectively, the mean and standard deviation estimated by Gaussian processes in iteration i.

- Expected Improvement function

$$Z = \frac{\mu_i - f(x^+) - \varepsilon}{\sigma_i(x)} \tag{2.22}$$

$$\mathscr{X} = \begin{cases} (\mu_i(x) - f(x^+) - \varepsilon)(\Sigma(Z) + \sigma_i(x)\phi(Z), & \text{if } \sigma_i(x) > 0, \\ 0, & \text{if } \sigma_i(x) = 0. \end{cases} \tag{2.23}$$

$$x_{i+1} = \underset{x}{\text{argmax}}\, \mathscr{X}, \tag{2.24}$$

  where $\phi(A)$ is the probability density function.

- Upper Confidence Bound (UCB) function

$$x_{i+1} = \underset{x}{\text{argmax}} \mu_i + \sqrt{\beta_i(x)}\sigma_i(x) \tag{2.25}$$

$$\beta_i = 2log\frac{N(i\pi)^2}{6\delta}, \tag{2.26}$$

  where, β_i is the weight of the adjustment uncertainty, which depends on the number of iterations already performed N and δ, a constant to be chosen by the user in the range $0 < \delta \leq 1$.

Bayesian Optimization with Botorch

Botorch, a state-of-the-art Bayesian optimization (BO) library developed by Meta AI, is engineered as a modular and extensible framework built natively on the PyTorch deep learning platform (Balandat et al., 2020). Its development was driven by the necessity for a modern, flexible tool capable of addressing complex and data-efficient global optimization problems encountered in both industrial production and scientific research (Bakshy, 2019). The foundational design principle of BoTorch is its profound modularity, which empowers researchers to fluidly compose, customize, and extend the fundamental primitives of Bayesian optimization: probabilistic surrogate models, acquisition functions, and optimizers (Balandat et al., 2020).

A pivotal innovation within BoTorch is its deep reliance on Monte Carlo (MC) based acquisition functions. This approach, enabled by the reparameterization trick and leveraging PyTorch's powerful auto-differentiation engine, circumvents the traditional and often arduous requirement of deriving analytical gradients for new optimization strategies. This design choice not only significantly enhances developer efficiency but also unlocks the potential for developing novel optimization methods for problems that defy analytic solutions, such as batch optimization and the modeling of multiple correlated outcomes (Bakshy, 2019).

In this study, the BO algorithm was employed through the Botorch library, with the objective of maximizing the function F_{obj}, defined in relation to the energy and charge of the beam accelerated by LWFA. The UCB acquisition function has been adopted.

3. METHODS

To achieve the objectives of the study, an initial effort was made to identify the operational parameters of an LPA capable of generating electron beams suitable for VHEE radiotherapy. Based on a chosen reference study, entitled "Toward an effective use of laser-driven very high energy electrons for radiotherapy: Feasibility assessment of multi-field and intensity modulation irradiation schemes" (Labate et al., 2020a), specific input parameters (e.g., laser and plasma profiles) and output parameters (e.g., energy, charge, and quality of the accelerated beam) were then defined to initiate PIC simulations. These PIC simulations were executed, and the objective function was subsequently evaluated. To optimize the process, Bayesian optimization was employed to derive new input parameters. This iterative process is illustrated in Figure 3.1. Each step will be discussed in detail in the following sections. The computational feasibility of this research was supported by the National Laboratory for Scientific Computing (LNCC/MCTI, Brazil), which provided access to the Santos Dumont supercomputer (Project LPA-FARMA), contributing significantly to the results reported in this work.

3.1 Initial Input Parameter Space for the Laser–Plasma Accelerator

To define the domains of the initial parameters to be optimized, a search was carried out to find LPA operating parameters that would produce VHEE beams suitable for radiotherapy application. As a result of this step, the study "Toward an effective use of laser-driven very high energy electrons for radiotherapy: Feasibility assessment of multi-field and intensity modulation irradiation schemes" (Labate et al., 2020a) was chosen for reference, since aimed to experimentally evaluate the feasibility of utilizing VHEE generated by LPAs for radiotherapy, specifically focusing on advanced irradiation schemes such as multi-field (MF) and intensity modulation (IM).

The experiments were conducted using the 220 TW Ti:Sa laser system at the The National Institute of Optics (CNR-INO) in Pisa, Italy. Laser pulses with energies of approximately 3 J and 30 fs duration were focused to an intensity of 6×10^{18} W/cm^2 (a0 $\simeq 1.7$) onto a 1.2 mm long gas-jet of He-N_2 mixture (2.5% N_2). Electron bunches were produced via Laser Wakefield Acceleration (LWFA), yielding a broad energy spectrum primarily within the 50 to 250 MeV range, which is ideal for treating deep-seated tumors. A passive collimator, designed with Monte Carlo simulations to minimize Bremsstrahlung photon contamination, was positioned about 38 cm downstream of the gas-jet to control the electron beam size. Dosimetric features were assessed using solid water plates and a water-filled tank with EBT3 gafchromic films as detectors. The study successfully demonstrated precise control over localized dose deposition and modulation, suitable for targeting volumes at depths of 5 to 10 cm with millimeter resolution, achieving doses up to 1.6 Gy within a few hundred shots.

Figure 3.1: Flowchart of the Bayesian optimization process in PIC simulations

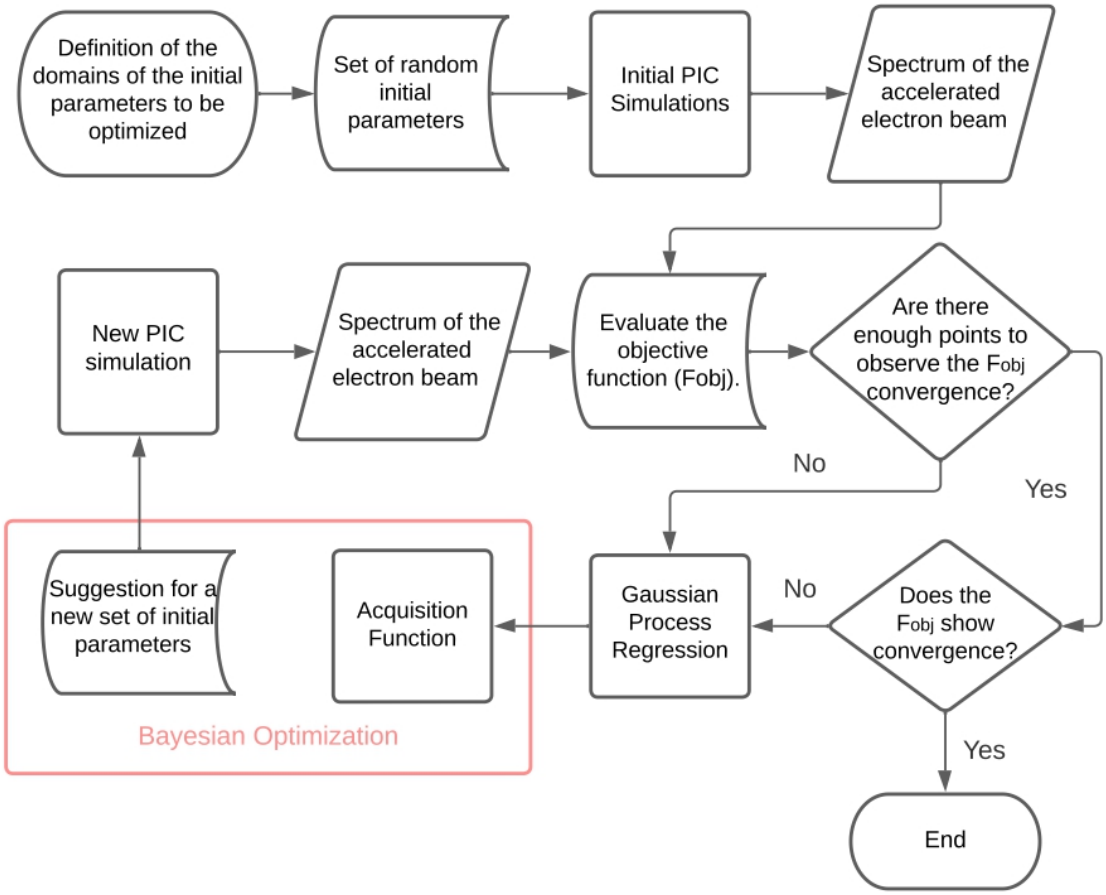

PIC simulations, performed with the Fourier-Bessel Particle-In-Cell (FBPIC) code on a 32GB NVIDIA Tesla V100 SXM2 GPU, were crucial for understanding the acceleration mechanism and validating experimental parameters. The simulations approximated the laser as a bi-Gaussian pulse and modeled the plasma density profile with linear ramps and a plateau. Ionization injection from nitrogen electrons was identified as the primary electron bunch formation process. The simulated electron spectrum, after applying a selection based on the experimental collimator, exhibited two broad peaks: one at approximately 50 MeV and another at roughly 200 MeV. This double-peaked structure was attributed to continuous electron injection and beam loading effects during acceleration. Monte Carlo (GEANT4) simulations further confirmed the experimental dose distributions for both MF and IM irradiation schemes, highlighting the excellent dose confinement properties of VHEE beams and demonstrating that photon dose contamination was negligible. Although shot-to-shot fluctuations in bunch charge (approximately 15% r.m.s.) were observed, the results validate the use of existing LPA technology as a platform for future pre-clinical studies in VHEE radiotherapy. The following tables depicts the details of

the simulation parameters used.

Table 3.1: PIC parameters.

Parameter	Value	Unit	Description
z_{min}	-70	µm	Initial boundaries of the longitudinal
z_{max}	0		simulation domain
r_1	80	µm	simulation domain radius
Δ_z	$\lambda_0/32$	nm	spatial resolution in z
Δ_r	$\lambda_0/12$	nm	spatial resolution in r
N_m	3	—	number of modes
N_{pz}	2	—	number of particles per cell along z
N_{pr}	2	—	number of particles per cell along r
$N_{p\theta}$	12	—	number of particles per cell along θ

Table 3.2: Laser parameters.

Parameter	Value	Unit	Description
P_L	220	TW	initial peak power
λ_0	800	nm	wavelength
z_0	-20	µm	pulse centroid
$c\tau$	1200	µm	pulse length (FWHM)
w_0	30	µm	waist
a_0	1.75	—	strength parameter

Table 3.3: Input parameters.

Parameter	Value	Unit	Description
z_{foc}	250	µm	laser focal position
n_{He}	0.397×10^{25}	m^{-3}	Helium density
n_{N}	0.003×10^{25}	m^{-3}	Nitrogen density
R_1	250	µm	up-ramp length
L_1	900	µm	plateau length
R_2	250	µm	down-ramp length

3.2 Fourier-Bessel Particle-In-Cell

The FBPIC code is a highly specialized numerical tool engineered for the simulation of relativistic plasma phenomena, particularly LWFA (Lehe et al., 2016a; Jalas et al., 2017). Its fundamental distinction from conventional PIC codes lies in its algorithmic core, which employs a spectral, quasi-cylindrical field representation (Lehe et al., 2016a). Instead of a 3D Cartesian grid, FBPIC utilizes a Fourier-Bessel decomposition, where fields are expanded into a series of azimuthal Fourier modes and radial Bessel functions (Lehe et al., 2016a). For physical systems exhibiting near-cylindrical symmetry, such as those typical in LWFA, this methodology

is exceptionally powerful. The full three-dimensional physics can be accurately captured by retaining only a small number of azimuthal modes, which confers the primary advantage of orders-of-magnitude greater computational efficiency and reduced memory requirements compared to standard 3D Cartesian codes, without sacrificing fidelity (Lehe et al., 2016a).

The rationale for employing FBPIC over a standard PIC implementation stems from its superior numerical properties and advanced capabilities tailored for LWFA. Conventional PIC codes often rely on Finite-Difference Time-Domain (FDTD) solvers, which are susceptible to spurious numerical dispersion that can lead to non-physical artifacts like Numerical Cherenkov Instability (NCI) (Jalas et al., 2017). FBPIC mitigates this critical issue by using a Pseudo-Spectral Analytical Time-Domain (PSATD) solver, which provides the significant advantage of intrinsic suppression of numerical dispersion and the associated Cherenkov radiation (Lehe et al., 2016a; Jalas et al., 2017). This ensures a more accurate representation of the underlying physics, which is crucial for sensitive predictions of beam quality (Jalas et al., 2017). Furthermore, FBPIC is optimized for computationally accelerated simulation techniques, most notably Lorentz-boosted frames, which can reduce simulation times dramatically (Kirchen et al., 2016; Lehe et al., 2016b). It uniquely incorporates a Galilean coordinate transformation that effectively eliminates the severe NCI that otherwise plagues boosted-frame simulations of relativistically drifting plasmas (Kirchen et al., 2016; Lehe et al., 2016b; Kirchen et al., 2020). This synergistic combination of a computationally efficient geometry, a high-fidelity dispersion-free solver, and a stable implementation of advanced acceleration techniques makes FBPIC a more accurate, robust, and powerful tool for LWFA research than generic PIC codes.

As previously noted, the investigation conducted by (Labate et al., 2020a) focused on the acceleration of VHEE within the bubble regime. The laser-plasma interaction and the acceleration process were simulated using the FBPIC code, which were used to achieve a better understanding of the acceleration mechanism and to compare the main experimental bunch parameters with the simulated ones.

Given the promising potential of employing BO to refine the intricate parameter space of particle accelerators and the proven potential of clinical VHEE application, this work specifically focuses on obtaining a quasi-monoenergetic bunch, i.e., a spectrum profile with a charge peak at a specific energy. To achieve this, input parameters, such as the specifications of the ramps, gas concentration, and plateaus that define the adopted gas density profile, along with the laser focal position, will be optimized. Other laser parameters will be kept fixed. The details of the simulation parameters utilized are presented in Table 3.4.

3.3 Bayesian optimization in PIC simulations

For each PIC simulation, the input parameters targeted for optimization include the specifications of the ramps and plateaus that characterize the chosen gas density profile, as well as the laser focal position. The output parameters are derived from the energy spectrum of the

Table 3.4: Laser-plasma interaction simulation parameters.

Parameter	Value or interval	Unit	Description
		1.1. PIC Parameters	
z_{min}	-33	μm	Initial boundaries of the longitudinal
z_{max}	0		simulation domain
r_{max}	80	μm	Simulation domain radius
Δ_z	$\lambda_0/32$	nm	Spatial resolution in z
Δ_r	$\lambda_0/12$	nm	Spatial resolution in r
$N_{m,pz,pr}$	2	—	Number of modes
$N_{p\theta}$	8	—	Number of particles per cell along θ
		1.2. Laser Parameters	
P_L	92.6	TW	Initial peak power
λ_0	800	nm	Wavelength
z_0	-15	μm	Pulse centroid
τ	30	fs	Pulse length (FWHM)
w_0	30	μm	Waist
		1.3. Input Parameters	
z_{foc}	25 , 1100	μm	Laser focal position
n_{He}	$0.25, 0.55$	$10^{19}\mathrm{cm}^{-3}$	Helium density
n_{N}	$0.0, 0.3$	$10^{19}\mathrm{cm}^{-3}$	Nitrogen density
R_1	50 , 350	μm	Up-ramp length
L_1	600 , 1400	μm	Plateau length
R_2	50 , 350	μm	Down-ramp length

accelerated beam, which is generated from the results of the PIC simulations. The proposed objective function F_{obj} depends on the product of the charge Q_i and another term that measures the obtained energies E_i reducing these values to near zero for energies far from the specified target energy, 200 MeV, with the reciprocal being true as well. For each PIC simulation, the obtained energy spectrum will be discretized by dividing the selected energy interval E_{sel} into N bins. If the i-th bin contains a nominal energy E_i and a given amount of charge Q_i, then the aforementioned quantities can be calculated as follows,

$$F_{obj} = \sum_{i=1}^{N_{bins}} Q_i e^{-0.1|E_i - E_{sel}|} \ . \tag{3.1}$$

This objective function is designed to promote the formation of a quasi-monoenergetic electron beam whose energy distribution is tightly centered on the target energy, E_{target}. To achieve this, each electron's contribution to F_{obj} is weighted by an exponential decay factor that increases with the distance of its energy from E_{target}. Consequently, electrons whose energies deviate from E_{target} contribute exponentially less, steering the optimization toward narrow, monoenergetic spectra focused on the desired energy.

4. ARTICLE

Bayesian optimization of a laser-plasma accelerator aiming the production of high-energy electron beams for VHEE radiotherapy

Article published in the Proceedings of the XXV Brazilian Symposium on Computing Applied to Health (SBCAS 2025), presenting the primary results of the methodology applied in this work.

Bayesian optimization of a laser-plasma accelerator aiming the production of high-energy electron beams for VHEE radiotherapy

Samara P. Santos[1,2], Bruno S. Nunes[2,3], Ricardo E. Samad[3], Nilson D. V. Jr.[3], Mirko S. Alva-Sanchez[1,2], Alexandre Bonatto[1,2]

[1]Graduate Program in Information Technology and Healthcare Management, Federal University of Health Sciences of Porto Alegre (UFCSPA), Porto Alegre 90050-170, Brazil

[2]Beam Physics Group, Federal University of Health Sciences of Porto Alegre (UFCSPA), Porto Alegre 90050-170, Brazil

[3]Nuclear and Energy Research Institute, IPEN–CNEN/SP, Sao Paulo 05508-000, Brazil

samaras@ufcspa.edu.br, abonatto@ufcspa.edu.br

Abstract. *Radiation therapy aims to maximize tumor dose while minimizing exposure to healthy tissues. Despite advances, normal tissue toxicity remains a significant obstacle. While proton therapy shows promise, its high cost limits widespread adoption. Very high-energy electrons (VHEE, 50-250 MeV) represent an alternative with deep tissue penetration suitable for conventional and FLASH radiotherapy, which enables higher curative doses while reducing normal tissue toxicity. Laser-plasma accelerators (LPAs) offer a compact and cost-effective approach to generating electron beams for VHEE radiotherapy, a modality with dosimetric advantages comparable to proton therapy but without requiring the large cyclotrons typically used for ion acceleration. This work implements Bayesian optimization to systematically tune particle-in-cell (PIC) simulations modeling an LPA, aiming to produce optimal electron beams for VHEE radiotherapy. Key findings include achieving a spectrum with two charge peaks at different energies and total integrated charge of 2.1 nC. Additionally, the Institute of Energy and Nuclear Research (IPEN) has recently received approval to acquire a 15 TW laser, making it the most powerful in the Southern Hemisphere. The framework developed in this work can be scaled to IPEN's laser system parameters to guide future VHEE radiotherapy experiments.*

1. Introduction

Radiotherapy (RT) is essential to treat most of malignant tumors, with the aim of providing enough radiation to eradicate cancer cells while minimizing damage to normal tissues [Lv 2022, Abdel-Wahab 2021]. Despite advances, dose-limiting toxicity to normal tissues remains a significant challenge [Lv 2022]. Although proton therapy shows promise, its high cost limits widespread adoption [Bulanov and Khoroshkov 2002, Kokurewicz 2017]. Current megavoltage electron beams (4-22 MeV) are limited to treating superficial tumors within 5 cm depth [IAEA 2005], however very high-energy electrons (VHEE, 50-250 MeV) offer superior tissue penetration for conventional and FLASH RT, with elevated

dose rates that potentially improves normal tissue tolerance while addressing tumor radiation resistance [Corsini 2021].

VHEE therapy provides reduced sensitivity to tissue heterogeneity, superior focusing capabilities, and flatter depth-dose profiles compared to X-rays and protons [Whitmore 2021]. Research shows that VHEE beams above 100 MeV provide uniform depth-dose distributions comparable to transmission proton beams, with VHEE energies of 150+ MeV achieving equivalent dosimetric quality to 250 MeV proton plans [Böhlen 2024], and can also be precisely focused at depths up to 15 cm [Kokurewicz 2021, Whitmore 2021]. Despite these advantages, VHEE technology remains in the developmental stage, with no commercially available clinical systems yet on the market. Laser-plasma accelerators (LPAs) represent a promising technology for generating VHEE beams more compactly and cost-effectively than conventional LINACs [Kokurewicz 2017, Corsini 2021]. While conventional accelerators are limited to gradients of 100 MeV/m, LPAs can achieve up to 100 GeV/m, with experimental results demonstrating 8 GeV electron beams in just 20 cm of plasma [Gonsalves 2019].

Given the complex dynamics governing LPA electron beam acceleration, this work proposes applying Bayesian Optimization (BO) to laser-plasma acceleration for generating electron beams suitable for VHEE RT, using Particle-in-Cell simulation data to optimize LPA parameters with an objective function that rewards the accumulation of charge at energies close to a selected target value. Although in a previous work an LPA operating in the self-modulated regime was optimized for the production of medical radioisotopes, prioritizing beam energy and charge over quality [Nunes 2025], this study specifically explores the bubble regime, aiming to produce high-quality beams suitable for RT applications.

The Institute of Energy and Nuclear Research (IPEN) has recently received approval to acquire a 15 TW laser, making it the most powerful in the Southern Hemisphere [Vieira Junior and Samad 2024]. This work will be scaled to IPEN's laser system parameters to guide future VHEE radiotherapy experiments.

2. The Model

In order to generate quasi-monoenergetic electron bunches for potential clinical applications, this study investigates VHEE acceleration in the bubble regime using the FBPIC code [Lehe 2015] to perform PIC simulations with fixed laser parameters and BO to optimize the simulation target. The internal parameters of the PIC simulations are presented in Table 1.1 and the laser pulse parameters are listed in Table 1.2, which are kept constant [Labate 2020]. The optimization aims to identify, within the intervals specified in Table 1.3, the values of the laser focal position (z_{foc}), the gas jet density profile (rising ramp, R_1; plateau, L_1; and falling ramp, R_2), and its composition (helium density, n_{He}, and nitrogen density, n_{N}) that maximize the electron charge with energies close to a predefined target value. These parameters physically characterize the LPA configuration.

The optimization process begins with a set of random experiments (n=5) with parameters assigned within specified ranges, then follows an iterative approach of selecting new sampling locations, collecting observations, and updating the model. In this study, the BO algorithm was employed through the Botorch library [Balandat 2020], with the objective of maximizing a function F_{obj}, defined in relation to the energy and charge of

Table 1. Laser-plasma interaction simulation parameters.

Parameter	Value or interval	Unit	Description
1.1. PIC Parameters			
z_{min}	-33	μm	Initial boundaries of the longitudinal
z_{max}	0		simulation domain
r_{max}	80	μm	Simulation domain radius
Δ_z	$\lambda_0/32$	nm	Spatial resolution in z
Δ_r	$\lambda_0/12$	nm	Spatial resolution in r
$N_{m,pz,pr}$	2	—	Number of modes
$N_{p\theta}$	8	—	Number of particles per cell along θ
1.2. Laser Parameters			
P_L	92.6	TW	Initial peak power
λ_0	800	nm	Wavelength
z_0	-15	μm	Pulse centroid
τ	30	fs	Pulse length (FWHM)
w_0	30	μm	Waist
1.3. Input Parameters			
z_{foc}	25 , 1100	μm	Laser focal position
n_{He}	$0.25, 0.55$	$10^{19} cm^{-3}$	Helium density
n_{N}	$0.0, 0.3$	$10^{19} cm^{-3}$	Nitrogen density
R_1	50 , 350	μm	Up-ramp length
L_1	600 , 1400	μm	Plateau length
R_2	50 , 350	μm	Down-ramp length

the beam accelerated by LPA. The upper confidence bound (UCB) acquisition function has been adopted. Figure 1 shows the details of this process.

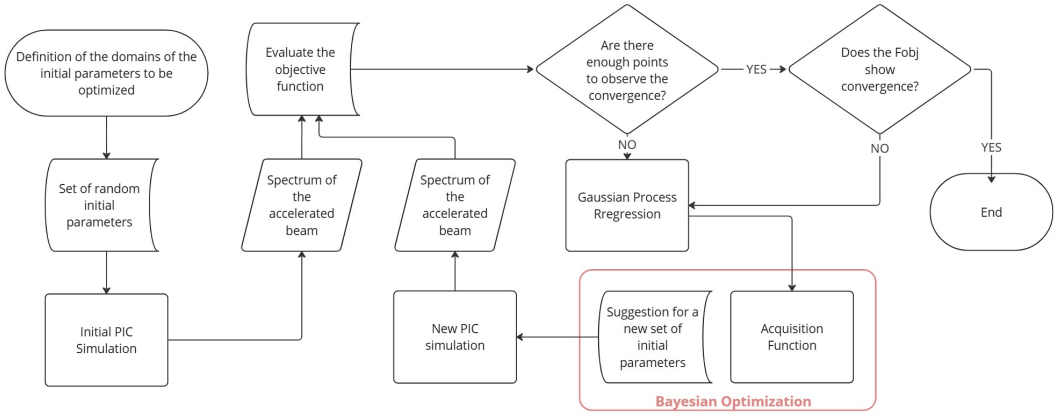

Figure 1. Flowchart of the BO process in PIC simulations.

Output parameters were derived from the energy spectrum of the accelerated electron beam generated by the simulations. The proposed F_{obj} combines the charge (Q) with a term that evaluates how closely obtained energies (E_i) match the target energy $E_t = 200\,\mathrm{MeV}$, chosen to provide sufficient penetration depth for treating deep-seated tumors. This approach allows the search for optimal parameters that result in a quasi-

monoenergetic bunch centered at the target energy. For analysis, the energy spectrum was discretized by dividing the selected energy interval into N bins. If the i-th bin contains a nominal energy E_i and a given amount of charge Q_i, then the aforementioned quantities can be calculated as follows,

$$F_{obj} = \sum_{i=1}^{N_{bins}} Q_i \, e^{-0.1|E_i - E_t|} \quad . \tag{1}$$

3. Results and Discussion

Figure 2(j) presents the achieved electron energy spectrum, spanning 50 to ∼450 MeV with a total charge of 2.1 nC. The spectrum features a bimodal distribution, with quasi-monoenergetic peaks at 75 MeV and 200 MeV, each reaching 15.0 pC per energy bin. This optimal spectrum results from the optimization based on the defined objective function F_{obj}, with $E_t = 200$ MeV, leading to a quasi-monoenergetic peak centered at E_t. Additionally, a second peak around 75 MeV was obtained. Magnetic fields could be employed to select which peak will be utilized, and their energies could be adjusted through attenuation.

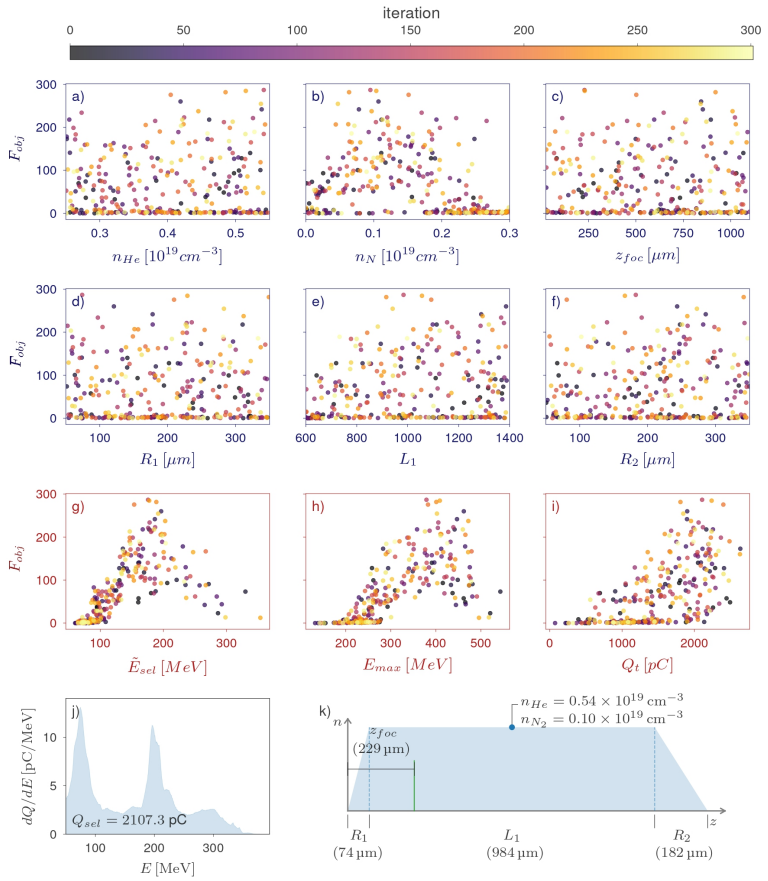

Figure 2. Bayesian Optimization Results, with a color scale indicating the algorithm iteration.

The FWHM energy spread per peak is 20–30 MeV (13–20% relative spreads for primary peaks) and a substantial high-energy tail extends beyond 300 MeV, reaching

nearly 450 MeV. This spectrum is particularly relevant for VHEE radiotherapy, where energies above 100 MeV ensure effective tissue penetration. The 2.1 nC charge supports high-dose or single-shot FLASH therapy, while energy-specific selection via magnetic filtering could optimize treatment planning. The observed spectral complexity underscores the advanced laser-plasma dynamics in the helium-nitrogen target, demonstrating the feasibility of LPAs for medical applications.

Figure 2 illustrates a systematic exploration of parameter space through BO across approximately 300 iterations. Panels a-f display the relationship between input parameters and the objective function value, which effectively weights charge by proximity to the selected energy. The helium density (n_{He}) distribution panel (a) shows peak objective function values around 0.5×10^{19} cm^{-3}, though significant variations suggest complex parameter interdependencies. For nitrogen doping panel (b), lower concentrations yield better results, indicating nitrogen acts as a controlled injection mechanism rather than a primary accelerator. The focusing position (z_{foc}) in panel c displays a non-monotonic trend, emphasizing the importance of precise laser focusing relative to plasma structure.

Geometric parameters R_1, L_1, and R_2 panels (d-f) exhibit scattered distributions, highlighting sensitivity to target geometry. In panel e, the plateau (L_1) at 1000 µm corresponds to peak objective function values. However, up-ramp (R_1) and down-ramp (R_2) optimizations panels (d, f) lack convergence, suggesting ramp configurations do not significantly affect final LPA optimization in the bubble regime.

Panels (g-i) reveal the direct proportional relationship between performance metrics and objective function values. Panel (g) shows a strong positive correlation between the selected energy ($\tilde{E}_{\mathrm{sel}}$) and the objective function up to 200 MeV, beyond which the performance declines, indicating an optimal energy window. Panel (h) displays a similar trend for the maximum energy (E_{max}), peaking at 300-400 MeV. The total charge (Q_t) in panel (i) reveals a clear positive correlation with the objective function throughout the explored range, with the highest values at charges exceeding 2000 pC.

4. Conclusions

The primary contribution of this study lies in optimizing simulation parameters using BO to produce clinically relevant electron beam characteristics for VHEE radiotherapy. By focusing on the bubble regime, the research demonstrated the production of quasi-monoenergetic electron bunches, resulting in an optimal spectrum with two quasi-monoenergetic peaks centered at 75 MeV and 200 MeV, respectively, which are appropriate for medical applications. The optimization approach yielded electron beams with approximately 2.1 nC total charge and distinctive spectral features.

Systematic exploration through 300 BO iterations revealed complex interdependencies between input parameters and beam characteristics. Future optimization efforts will prioritize the most influential parameters by analyzing their correlation with the objective function F_{obj}, while exploring alternative objective function formulations to enhance convergence and beam quality. Additionally, we plan to conduct a series of simulations with a 15TW laser system to prepare for experimental validation at IPEN, where this technology is expected to be operational by 2027.

These findings represent significant progress toward the practical implementation of compact laser-plasma-based accelerators for radiotherapy. The beam parameters

achieved, particularly the high charge at energies exceeding 100 MeV with reasonable energy spread, satisfy key requirements for the potential implementation of radiotherapy. The BO approach offers a powerful tool for navigating the complex parameter space of laser-plasma acceleration, potentially accelerating the development and clinical translation of this promising technology for cancer treatment.

References

Abdel-Wahab, e. a. (2021). Global radiotherapy: Current status and future directions—white paper. *JCO Global Oncology*, (7):827–842.

Balandat, Maximilian, e. a. (2020). BoTorch: A Framework for Efficient Monte-Carlo Bayesian Optimization. In *Advances in Neural Information Processing Systems 33*.

Böhlen, Till Tobias, e. a. (2024). Very high-energy electron therapy as light-particle alternative to transmission proton flash therapy – an evaluation of dosimetric performances. *Radiotherapy and Oncology*, 194:110177.

Bulanov, S. V. and Khoroshkov, V. S. (2002). Feasibility of using laser ion accelerators in proton therapy. *Plasma Physics Reports*, 28(5):453–456.

Corsini, Roberto, e. a. (2021). Status of vhee radiotherapy related studies at the clear user facility at cern. *Proceedings of the 12th International Particle Accelerator Conference*, IPAC2021:Brazil.

Gonsalves, A.J., e. a. (2019). Petawatt laser guiding and electron beam acceleration to 8 gev in a laser-heated capillary discharge waveguide. *Physical Review Letters*, 122(8).

IAEA (2005). *Radiation Oncology Physics*. Non-serial Publications. INTERNATIONAL ATOMIC ENERGY AGENCY, Vienna.

Kokurewicz, K., e. a. (2017). Laser-plasma generated very high energy electrons (vhees) in radiotherapy. In *Medical Applications of Laser-Generated Beams of Particles IV: Review of Progress and Strategies for the Future*. SPIE.

Kokurewicz, K., e. a. (2021). An experimental study of focused very high energy electron beams for radiotherapy. *Communications Physics*, 4(1).

Labate, Luca, e. a. (2020). Toward an effective use of laser-driven very high energy electrons for radiotherapy: Feasibility assessment of multi-field and intensity modulation irradiation schemes. *Scientific Reports*, 10(1).

Lehe, Remi, e. a. (2015). A spectral, quasi-cylindrical and dispersion-free particle-in-cell algorithm.

Lv, Yinghao, e. a. (2022). Flash radiotherapy: A promising new method for radiotherapy (review). *Oncology Letters*, 24(6).

Nunes, B. S., e. a. (2025). Bayesian optimization of laser wakefield acceleration in the self-modulated regime (sm-lwfa) aiming to produce molybdenum-99 via photonuclear reactions. *Physics of Plasmas*, 32(3).

Vieira Junior, N. D. and Samad, R. E. (2024). Implantação de um laser de altíssima intensidade como uma infraestrutura científica multiusuário no brasil.

Whitmore, L., e. a. (2021). Focused vhee (very high energy electron) beams and dose delivery for radiotherapy applications. *Scientific Reports*, 11(1).

5. DISCUSSION

5.1 Bayesian Optimization aiming molybdenum-99 production

The Beam Physics Group at UFCSPA developed a research on BO of an LPA, but without addressing beam quality and using the self-modulated regime. As an initial step to familiarize the author with the research methodology, a book chapter was prepared summarizing the preliminary results, along with contributions to the writing and review of a paper presenting the main findings. The book chapter entitled "Optimizing Laser-Plasma Accelerators for Medical Radioisotope Production" and the article entitled "Bayesian optimization of laser wakefield acceleration in the self-modulated regime (SM-LWFA) aiming to produce molybdenum-99 via photonuclear reactions", present in APPENDIX A and APPENDIX B respectively, are results of this stage. A brief overview of their main results is provided below.

The book chapter outlines a study on the optimization of a laser-plasma accelerator for the production of the medical radioisotope Molybdenum-99 (Mo^{99}). Bayesian optimization was applied to PIC simulations of a laser–plasma accelerator featuring a symmetric trapezoidal gas target, with the aim of maximizing a combined metric of beam energy and charge. A higher production yield of Mo^{99} is likewise achieved through the enhancement of these beam parameters. The significance of this isotope lies in its decay to Technetium99m (Tc^{99m}), the most prevalent radioisotope used in nuclear medicine diagnostics. The conventional method for producing Mo^{99} involves the fission of highly enriched uranium (U^{235}) in nuclear reactors, a process that carries concerns regarding radioactive waste management and nuclear proliferation. A promising alternative is photoactivation through the $Mo^{100}(\gamma, n)Mo^{99}$ photonuclear reaction. This reaction has a high cross-section for photons with energies in the 8 MeV to 20 MeV range, peaking at approximately 14.5 MeV. In this proposed scheme, these photons are generated as bremsstrahlung radiation when an electron beam, accelerated by a LWFA, impinges on a Tantalum (Ta) converter.

The optimization framework was designed around a 5 TW peak power laser system operating in the high-repetition-rate, self-modulated LWFA (SM-LWFA) regime. This system generated Gaussian pulses of 50 fs duration with a 7 μm waist radius. The complex plasma dynamics were modeled using PIC simulations performed with the FBPIC code on the Santos Dumont supercomputer. To find the optimal conditions, a BO algorithm, implemented via the Botorch package, was used to vary three key input parameters: the laser focal position, the ratio of plasma to laser angular frequencies, and the length of the gas density plateau. The target consisted of a symmetric trapezoidal density profile of Hydrogen (H_2) gas with fixed 80 μm ramps. The optimization was guided by an objective function that aimed to maximize the charge and energy of electrons accelerated beyond the 8 MeV threshold required for the photonuclear reaction.

The results of this optimization process showed convergence after approximately 150 iterations, with the objective function stabilizing at a value of 7.9±0.3 (arbitrary units). The optimal input parameters were found to be a laser focal position of approximately 57 μm and a plateau length of about 47.5 μm, while the frequency ratio required fine-tuning. This configuration yielded an optimized electron beam with a total charge of 544 pC and a median energy of 15.1 MeV, which is ideally centered on the peak cross-section of the target photonuclear reaction. The maximum electron energy achieved in the beam was 59 MeV. In conclusion, the objective of producing a tailored electron beam for Mo^{99} production was successfully achieved. Through the systematic application of BO to PIC simulations, an optimal set of accelerator parameters was identified. The resulting electron beam, with its high charge and ideal energy characteristics, is well-suited for driving a compact and efficient source of essential medical radioisotopes, representing a significant advancement toward a viable alternative to reactor-based production.

Following the same objective as the previous study, the paper "Bayesian optimization of laser wakefield acceleration in the self-modulated regime (SM-LWFA) aiming to produce molybdenum-99 via photonuclear reactions" explored different gas profiles. Three distinct gas density profiles were investigated, with lengths ranging from 200 to 400 μm, combining ramps and plateaus.

The first case investigated involves an asymmetric trapezoidal longitudinal gas density profile, characterized by independently optimizable up-ramp and down-ramp lengths, a central plateau, the laser focal position, and the plasma-to-laser frequency ratio. The optimization, conducted over more than 400 PIC simulations, converged after approximately 40 iterations, with the laser-to-beam efficiency stabilizing at $2.6 \pm 0.3\%$. The maximum efficiency achieved was 3.8% obtained with a focal position of 113.4 μm, a frequency ratio of 0.210, an up-ramp of 99.8 μm, a plateau of 59.8 μm, and a down-ramp of 62.1 μm. The resulting optimized electron beam (for energies > 8 MeV) featured a selected charge of approximately 601 pC, a median energy of 16.9 MeV, and a maximum energy of 73 MeV. Analysis of the laser-plasma dynamics revealed that Direct Laser Acceleration (DLA) was the dominant energy contribution mechanism for the highest-energy electrons. The estimated Mo^{99} yield from this beam was 0.513×10^6 atoms per pulse, which, at a 1 kHz repetition rate, would just surpass the 370 MBq activity required per patient after seven days of irradiation.

The second case introduced a stepped-down two-plateau profile, motivated by the goal of sustaining the acceleration bubble over a longer distance. This configuration significantly improved performance, with the optimization converging to an efficiency of $5.5 \pm 0.3\%$ and achieving a maximum value of 6.3% representing a 67% increase over Case 1. The optimal parameters included a focal position of 57.9 μm, plasma-laser frequency ratios of 0.216 and 0.208, and a long central down-ramp of 100.5 μm. The resulting electron beam exhibited a substantially higher charge of 999 pC, a median energy of 14.6 MeV, and a maximum energy of 81 MeV. The key physical difference was that the longer, less steep intermediate down-ramp promoted strong electron self-injection. In this scenario, both LWFA and DLA made signifi-

cant positive contributions to the final electron energy. Consequently, the Mo^{99} yield increased to 0.911×10^6 atoms per pulse, a level sufficient to reach the 740 MBq U.S. activity standard within seven days of irradiation at 1 kHz.

The third case further generalized the two-plateau profile by removing the constraint that the second plateau must have a lower density. This flexibility led to the best performance, with the efficiency converging to $7.6 \pm 0.4\%$ and reaching a maximum of 8.3%. The optimal configuration notably featured an intermediate ramp that became a long, steep up-ramp (118.2 μm), transitioning to a higher density second plateau. This profile generated the most impressive electron beam, with a charge of 1305 pC, a median energy of 16.7 MeV, and a maximum energy of 87 MeV. Its energy spectrum was unique, deviating from the typical exponential decay to show near-constant charge plateaus at high energies (60-80 MeV). In this regime, LWFA became the dominant acceleration mechanism, providing a sustained energy boost. This resulted in the highest Mo^{99} yield of 1.103×10^6 atoms per pulse, capable of exceeding the 740 MBq threshold in approximately 4.5 days of irradiation at 1 kHz.

In conclusion, this comparative study demonstrates a clear performance progression across the three gas density profiles. The generalized two-plateau profile (case 3) yielded the highest laser-to-beam efficiency (8.3%) and electron charge (1305 pC), establishing LWFA as the dominant acceleration mechanism. In contrast, the simpler asymmetric profile (case 1) was limited in performance and dominated by DLA, while the stepped-down profile (case 2) offered a significant improvement by enhancing electron self-injection through a balanced contribution from both LWFA and DLA. A strong correlation was observed between the total beam charge and the potential Mo^{99} yield, with Case 3 showing the most promise for practical applications. Despite these significant advancements, the simulated yields are not yet sufficient for immediate clinical use with a single laser system. Future work must address limitations such as the risk of unwanted photonuclear reactions, the need for fully 3D PIC simulations, and the validation of Monte Carlo yield estimates. Nonetheless, these results represent a critical step toward developing compact, laser-driven accelerators for medical isotope production.

5.2 Bayesian Optimization for VHEE-RT

In order to find a high-quality beam suitable for use in radiotherapy, the study was evolved to apply BO to an LPA operating in the bubble regime. As an initial result of this step, the paper "Bayesian optimization of a laser-plasma accelerator aiming the production of high-energy electron beams for VHEE radiotherapy", presented in chapter 5, was obtained. The primary objective was to implement BO to systematically tune PIC simulations of a LPA. This computational framework was applied to the bubble regime with the aim of producing optimal high-energy electron beams suitable for VHEE radiotherapy. The optimization process sought to maximize electron charge at a target energy of 200 MeV, a value chosen for its sufficient penetration depth for treating deep-seated tumors. To achieve this, the BO algorithm explored

a complex parameter space, including the laser focal position, the gas jet density profile (rising ramp, plateau, and falling ramp lengths), and the gas composition, specifically the respective densities of helium and nitrogen.

The study presented in Chapter 5 systematically explored the parameter space through approximately 307 BO iterations, revealing complex interdependencies. Analysis indicated that peak objective function values occurred with a helium density around $0.5 \times 10^{19}\text{cm}^{-3}$, while lower nitrogen concentrations yielded superior results, suggesting that nitrogen's primary role is to provide a controlled injection mechanism. A plateau length of 1000 µm consistently corresponded to peak performance; however, the optimizations for the up-ramp and down-ramp lengths lacked clear convergence, indicating their configurations did not significantly impact the final LPA optimization in the bubble regime. Strong positive correlations were observed between the objective function and both the selected energy (up to 200 MeV) and the total charge, which reached values exceeding 2.1 nC.

Although an asymptotic convergence toward the highest objective-function values was not achieved, the optimization successfully yielded an electron beam with a broad energy spectrum spanning from 50 MeV to approximately 450 MeV, carrying a total integrated charge of 2.1 nC. A key feature of the resulting spectrum is a bimodal distribution, which exhibits quasi-monoenergetic peaks centered at 75 MeV and 200 MeV, each contributing a charge of 15 pC per energy bin. The full width at half maximum (FWHM) energy spread for these peaks was between 20-30 MeV, corresponding to a relative spread of 13-20%. By comparison, a clinical RF linac's therapeutic 6 MeV electron beam emerges from the exit window with a FWHM of just 0.04 MeV ($\sim$0.62 %) and broadens to about 0.40 MeV ($\sim$6.4 %) at the phantom surface (Apaza Veliz et al., 2020), highlighting the tighter energy uniformity of conventional machines. Furthermore, VHEE beams based on RF linacs have energy dispersion mostly below 1% (Panaino et al., 2025). To bring an LWFA-driven beam in line with the $\lesssim 1$ % energy spread typical of radiotherapy, post-generation conditioning such as magnetic-dipole spectrometers with narrow slits for momentum selection (André et al., 2018) or passive absorptive collimators can be employed to scrape away off-energy tails and isolate a narrower, quasi-monoenergetic core. The high total charge is sufficient to support high-dose or single-shot FLASH therapy modalities, and the distinct energy peaks could be selected for treatment using magnetic fields or collimators.

As seen previously, although approximately 307 BO iterations resulted in an electron spectrum with characteristics that are relevant for the clinical application of VHEE radiotherapy, it was not possible to observe convergence of the parameter values and, therefore, it was not possible to find optimal values. Thus, the simulation cycle was continued, but with a greater number of iterations in order to seek convergence.

Figure 5.1 shows the results of 377 BO iterations. A comparative analysis between the initial results and the extended results shows improvements towards obtaining electron beams suitable for VHEE radiotherapy. The most significant evolution occurred in the characteristics

of the accelerated electron beam. An objective function targeting a quasimonoenergetic bunch at ∼200 MeV was employed. Following the first 307 PIC simulations, a bimodal energy spectrum was produced, featuring quasi-monoenergetic peaks at ∼75 MeV and ∼200 MeV. With the optimization extended by 70 additional simulations (377 total), the lower-energy peak was raised to ∼160 MeV, bringing the spectrum significantly closer to the ideal single peak at 200 MeV, as rewarded by the objective function. The total accelerated charge experienced a moderate reduction from 2.1 nC to approximately 1.86 nC , and the maximum energy of the spectrum decreased from a high-energy tail reaching nearly 450 MeV to a sharper cutoff around 300 MeV, which can be seen as positive, as it indicates less energy scattering in the high energy region, concentrating electrons more effectively around 200 MeV.

As discussed in subsection 2.2.2, the choice of gases employed as the LPA's plasma source upon ionization has significant implications for LPA performance, affecting electron beam quality, stability, and the acceleration mechanism. The effectiveness of H_2, N_2, and He as gas targets in LPAs varies considerably due to their ionization properties and the resulting impact on laser pulse propagation and wakefield formation (Monzac et al., 2024).

While the prior study of the self-modulating regime employing pure hydrogen achieved successful convergence, our present analysis - performed with a helium–nitrogen (He + N_2) mixture to mirror that reference — did not. Although in our study Bayesian optimization did not converge to optimal values, the best spectrum it produced still shows clear improvements over the reference spectrum presented in Figure 5.2. The spectrum derived from the recent optimization results (Figure 5.3) is defined by two quasi-monoenergetic peaks centered at energies of ∼160 MeV and ∼197 MeV, respectively. This configuration, which features a significantly lower charge component at energies below 100 MeV, demonstrates the success of the optimization process in concentrating the accelerated charge within the therapeutically relevant window. In stark contrast, the ancillary spectrum provided exhibits a multimodal distribution. This spectrum is dominated by a prominent peak at approximately 50-60 MeV and a substantial population of very low-energy electrons, with only a secondary, much smaller peak appearing at the 200 MeV target.

Consequently, the spectrum from the new optimization results is qualitatively superior for the intended application in VHEE radiotherapy. The resulting beam is significantly "cleaner," indicating that the acceleration process was effectively controlled to focus charge at the desired therapeutic energy for treating deep-seated tumors. Conversely, the reference spectrum represents a less optimized acceleration process, where the majority of the laser's energy was transferred to electrons outside the desired energy window.

5.2.1 Parameter correlation analysis

Correlation analyses were performed between input and output parameters — and between these parameters and the objective function — to assess how variations in the inputs influence the final spectrum and to identify the most impactful variables. Parameters identified as non-

Figure 5.1: Bayesian optimization results, with a color scale indicating the algorithm iteration. Input parameters versus iteration: (a) laser focal position (z_{foc}), (b) Helium density (n_{He}), (c) Nitrogen density (n_N), and parameters for the gas-density profile including (d) initial radius (R_1), (e) length (L_1), and (f) final radius (R_2). Output parameters versus iteration: (g) selected energy ($\tilde{E}_{sel}$), (h) maximum energy (E_{max}), and (i) total charge (Q_t). Optimal results are shown for the (j) energy spectrum, which achieved a selected charge (Q_{sel}) of 1862.4 pC, and (k) the gas-density profile, with the corresponding optimal input values of $n_{He} = 0.48 \times 10^{19}$ cm^{-3}, $n_N = 0.09 \times 10^{19}$ cm^{-3}, $z_{foc} = 815$ µm, $R_1 = 240$ µm, $L_1 = 1388$ µm, and $R_2 = 278$ µm.

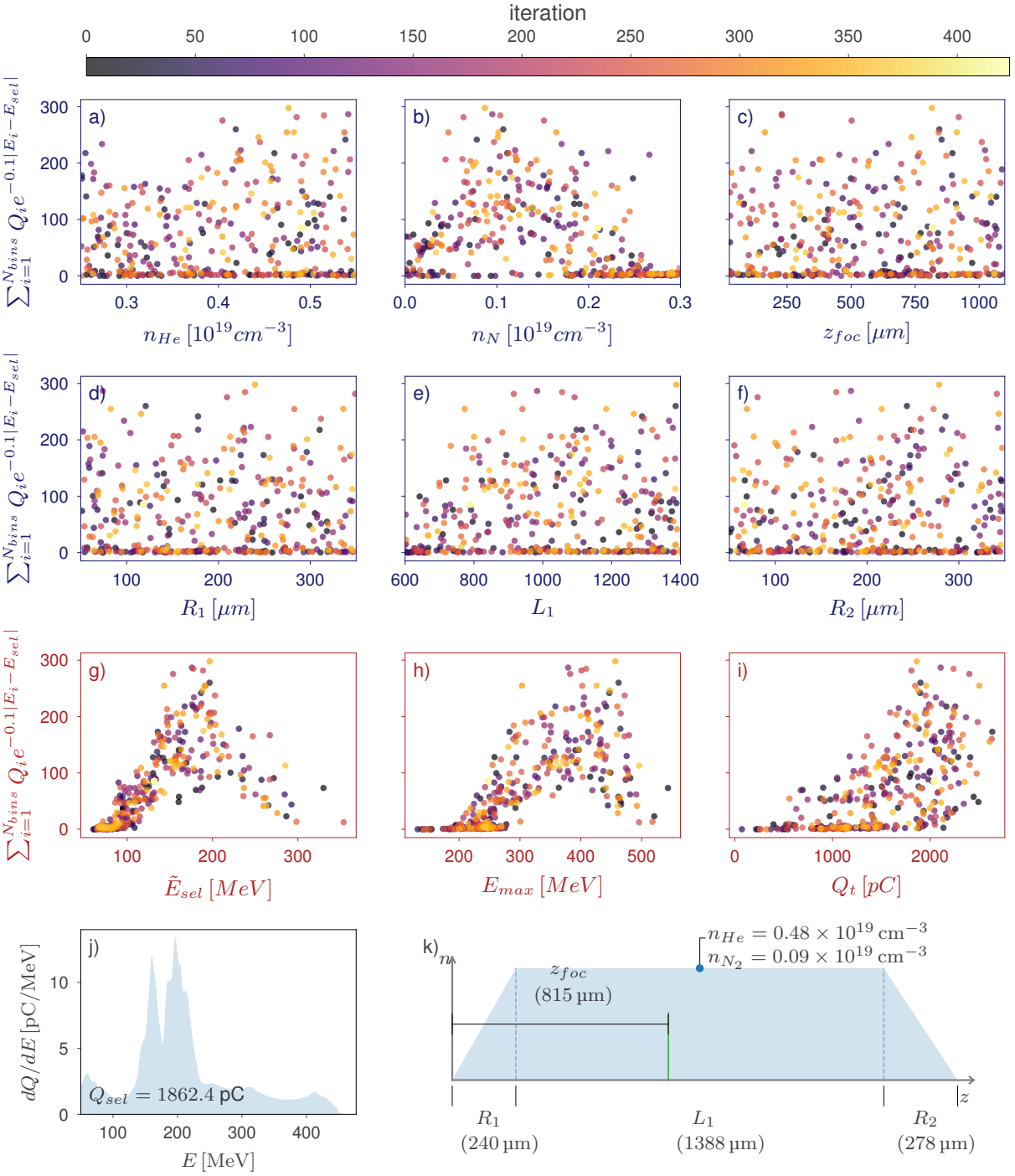

Source: Author

Figure 5.2: Electron spectrum of the reference study provided by their PIC simulation.

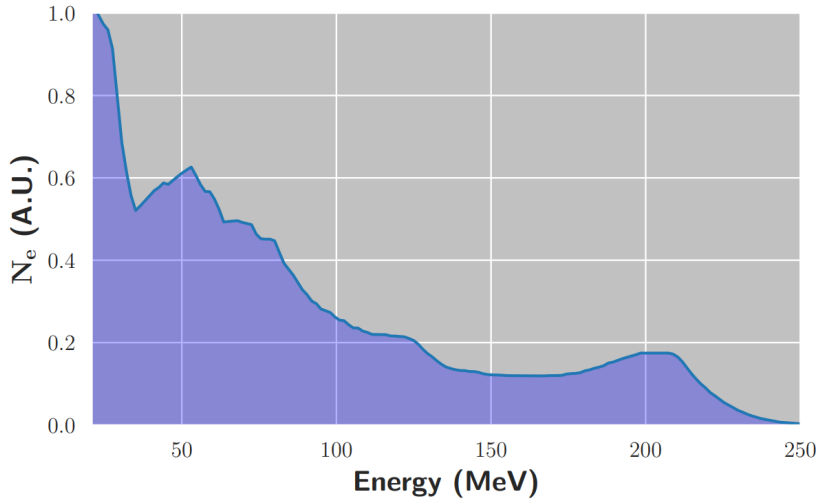

Source: (Labate et al., 2020b)

Figure 5.3: Optimal spectrum obtained from BO.

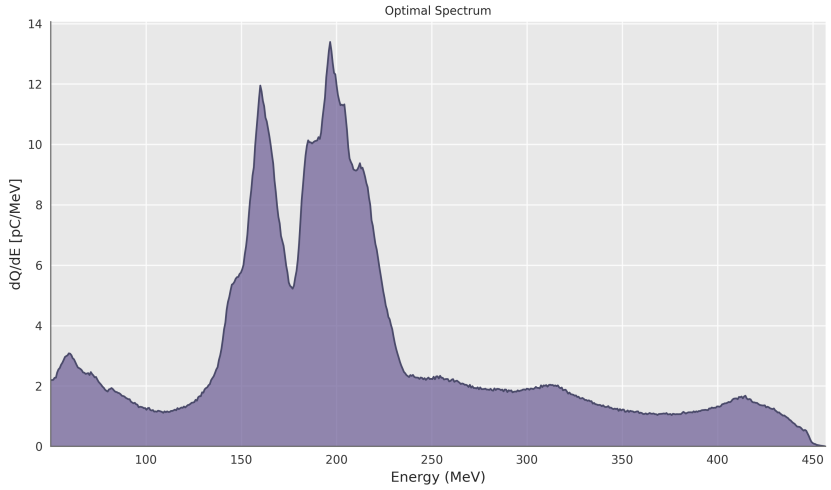

Source: Author

relevant or exhibiting collinearity through correlation analysis could be omitted from future simulation loops, thereby reducing computational cost. Among the methods for calculating correlation, Spearman's correlation is particularly useful for situations where a linear relationship between the data is not required. This non-parametric technique is employed when the assumption of data normality is violated, as it does not presuppose a specific distribution of the data. Additionally, the Spearman test is applicable to both ordinal and continuous data, provided they exhibit a monotonic relationship, meaning the direction of the relationship between the two variables remains consistent.

Spearman rank (r_s) order tests determine the strength and direction of the monotonic relationship between two variables measured at the ordinal, interval, or ratio level. In order to

measure the strength of the relationship, it is possible to follow the convention of table 5.1.

Table 5.1: Spearman rank (r_s) vs. correlation strength.

Spearman rank (r_s)	**Correlation strength**
$0 < r_s < \pm 0.3$	Weak monotonic relationship between the two variables
$\pm 0.4 < r_s < \pm 0.6$	Monotonic relationship of moderate strength between the two variables
$\pm 0.7 < r_s < \pm 1.0$	Strong monotonic relationship between the two variables

The correlation of input parameters from 377 simulations was analyzed. These parameters included helium and nitrogen densities, laser focal position, and the lengths of the ascent, plateau, and descent ramps, as well as output data such as the objective function, selected energy, maximum energy, and total load. To discern the characteristics of the most successful outcomes, the analysis was performed on the entire dataset as well as on elite subsets comprising the top 50 and top 20 with the higher objective functions. The results provide a quantitative foundation for understanding the parameter space and validating the focus of the Bayesian optimization algorithm. The correlation was calculated using the correlation function from the Pandas library in Python, specifying the 'spearman' method.

Figure 5.4 shows the correlations of input and output parameters with the objective function, while Figure 5.5 shows the pairwise correlation among the parameters. The primary determinants of the objective function are unequivocally the energy characteristics of the generated electron beam. A strong positive correlation was observed between the objective function and both the median energy ($E_{median}, r = 0.85$) and the maximum energy ($E_{max}, r = 0.80$). This confirms that the defined objective function effectively prioritizes the production of high-energy electron beams for all data, a fundamental requirement for applications in VHEE radiotherapy. However, for the top 50 and top 20 subsets, this pattern is not observed, indicating that, for the highest objective functions achieved, prioritization was not effective. While the total charge (Q_t) also exhibits a significant positive correlation in the full dataset ($r = 0.70$), its influence diminishes within the top-performing subsets, indicating that while charge is an important secondary metric, spectral energy is the paramount factor distinguishing optimal results.

Among the input parameters, the gas composition was identified as the most critical factor influencing the final beam energy and, consequently, the objective function. Specifically, the nitrogen density (n_N) demonstrates a moderate negative correlation with the objective function ($r = -0.41$), a relationship that intensifies markedly within the top 20 subset ($r = -0.57$). This is explained by the strong negative correlation between n_N and both median and maximum energy. Conversely, the helium density (n_{He}) exhibits a positive correlation with the objective function that strengthens for the top 50 ($r = 0.31$) and top 20 ($r = 0.34$) simulations. This opposing influence suggests that the optimization process converges towards a regime characterized by minimal nitrogen and elevated helium concentrations to maximize beam energy.

While gas density primarily governs beam energy, the analysis reveals that the plasma ramp

Figure 5.4: Correlations of input and output parameters with the objective function, showing a direct measure of what parameters lead to a successful outcome.

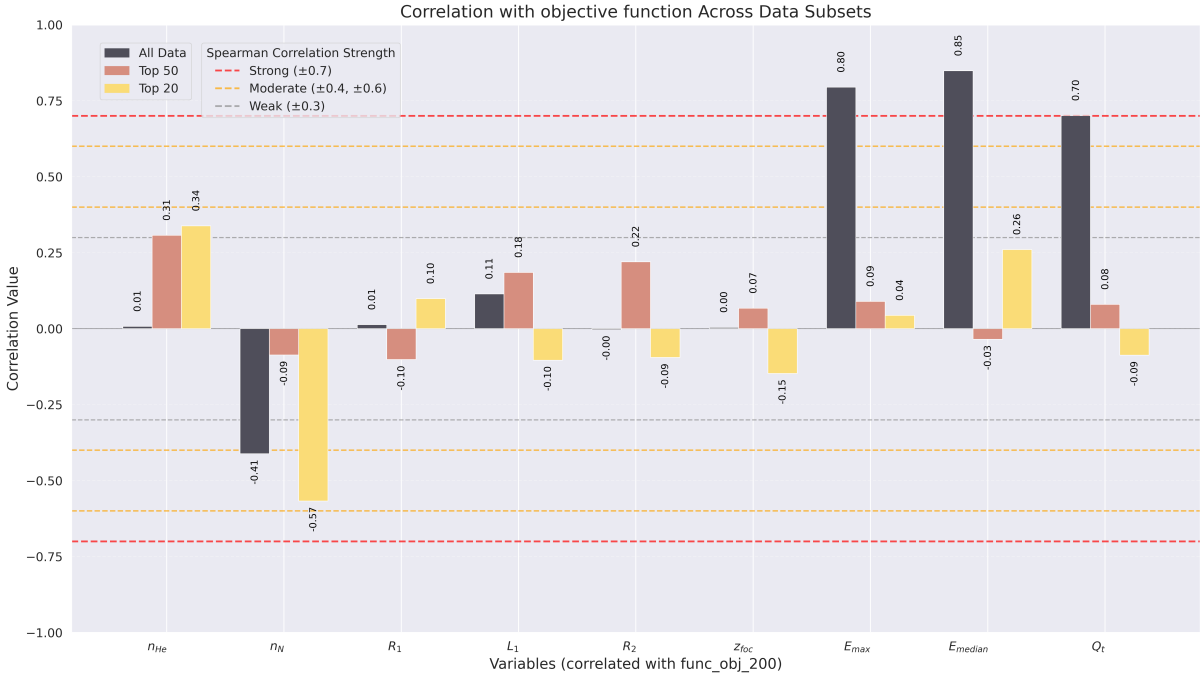

Source: Author

geometry is the principal control mechanism for the total accelerated charge (Q_t). A notably negative correlation emerges between "Q_t" and the descent ramp length (R_2), particularly within the top 20 results, where the correlation coefficient approximates $r = -0.70$. A similar, albeit weaker, positive trend is observed with the plateau length (L_1). This finding is of significant practical importance, as it decouples the optimization of charge from the optimization of energy. It suggests a clear strategy wherein the gas mixture is tuned to achieve the desired energy spectrum, while the plasma profile's trailing edge is diminished to maximize the total charge of the beam.

Regarding the Laser Focus Position, we can also see some significant influences. Regarding the gas composition, we see a moderate negative relationship of nitrogen density with z_{foc} and total charge, while we see a moderate positive force with respect to E_{max} and E_{median}.

The influence of parameters such as laser focus position, nitrogen concentration and gas density profile on the properties of a high-quality electron beam using LWFA, such as charge, energy and emittance, has already been investigated (Maity et al., 2024). The research use PIC simulations to examine a two-section gas cell target, a hydrogen-nitrogen mixture for ionization injection and pure hydrogen for acceleration.

The authors extensively investigated the influence of the laser focusing position on the accelerated electron beam properties. They observed that increasing laser focusing position generally leads to a decrease in both the net beam charge and the charge within the full width at half maximum (FWHM) of the energy histogram. Conversely, the peak energy of the accelerated electron

Figure 5.5: The pairwise correlation plots among parameters. Explain the underlying physics and parameter interactions that lead to the trends observed in the objective function analysis.

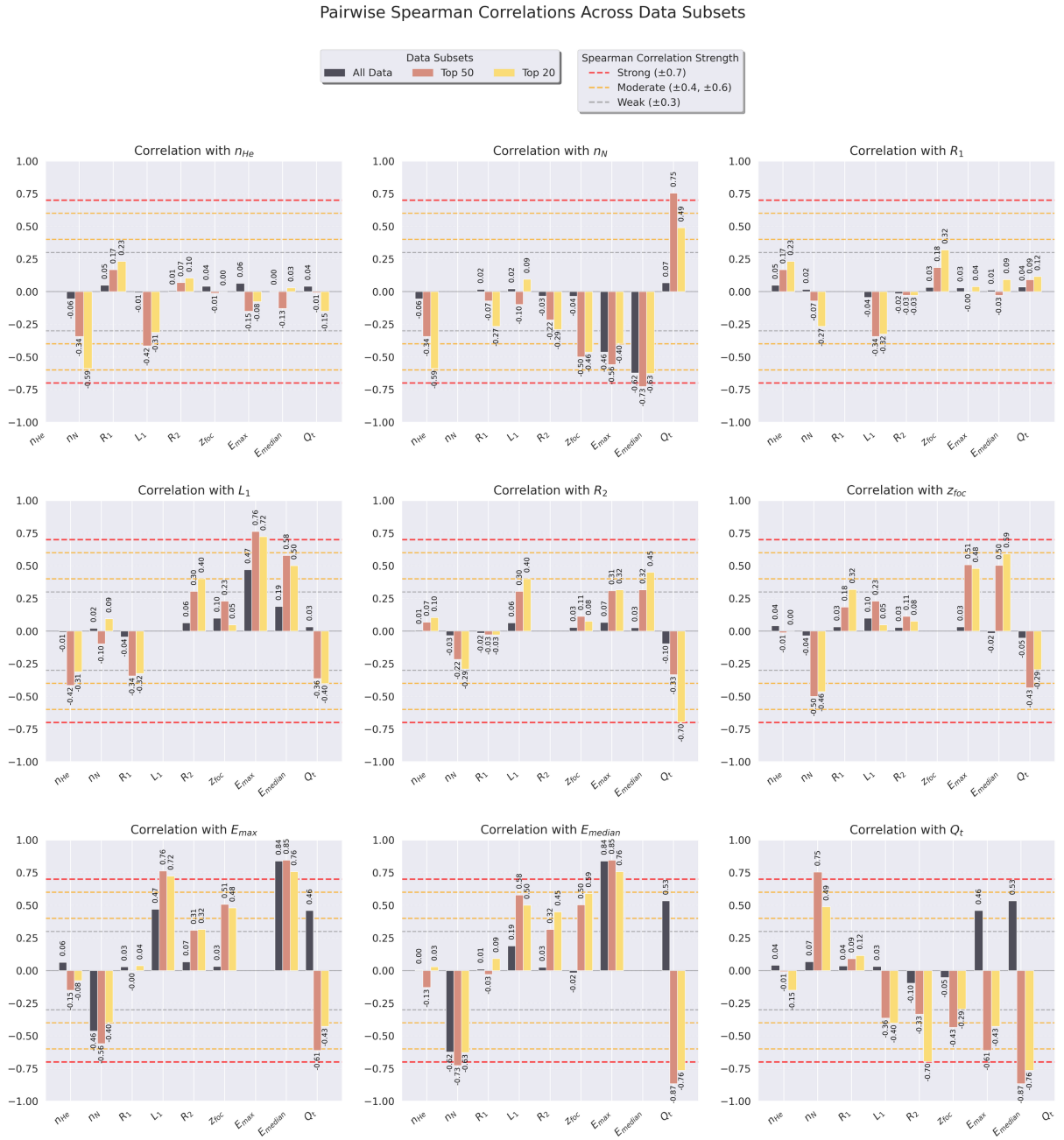

Source: Author

beam was found to increase monotonically with laser focusing position, with higher laser focusing position values yielding narrower energy distributions and higher maximum gained energy. The relative energy spread decreased as f increased, eventually saturating beyond approximately 3.7 mm. Furthermore, the normalized beam emittance consistently decreased with an increase in laser focusing position, and the beam divergence became narrower as laser focusing position increased. For lower values (e.g., 3.0 mm and 3.3 mm), a significant beam loading effect was observed, modifying the longitudinal electric field profile, which was less prominent or absent

at higher laser focusing position values (e.g., 3.7 mm). This collective behavior indicates that a higher laser focusing position can lead to lower charge but significantly improved energy and emittance characteristics, primarily by mitigating the beam loading effect. Similar results regarding energy and charge can be found analyzing the correlation with z_{foc} plot in Figure 5.5 for top 20 and top 50 subsets.

The nitrogen concentration in the first stage of the gas target also played a crucial role in shaping the electron beam's quality. As the gas concentration increased, both the net beam charge and the FWHM charge were observed to increase. This rise in charge is directly linked to an enhanced beam loading effect, where the space charge of the trapped electrons flattens the accelerating field within the bubble. Consequently, the peak energy of the beam decreased with increasing nitrogen concentration, as the reduced electric field gradient limited the maximum energy gain. Correspondingly, the relative energy spread increased with higher nitrogen concentration values. Similarly, the normalized beam emittance also increased with rising concentration, particularly for nitrogen concentration > 7%, where its evolution initially increased before decreasing and saturating. The beam divergence showed an increase with nitrogen concentration but generally remained within approximately 5 mrad. These findings highlight a trade-off where higher nitrogen concentrations facilitate greater electron injection and charge, but at the cost of lower energy, higher energy spread, and increased emittance due to pronounced beam loading. Similar results regarding energy and charge can be found analyzing the correlation with n_N plot in Figure 5.5, especially for top 50 subset.

In conclusion, this correlation analysis provides critical insights into the physics of the laser-plasma interaction and offers clear strategic guidance for the BO process. The results validate the algorithm's trajectory towards a parameter space defined by low nitrogen density and high helium density, which directly promotes higher beam energies. Furthermore, the analysis identifies the descent ramp length as a key, semi-independent parameter for enhancing total beam charge. The weak to moderate inter-correlation among the input parameters is also advantageous, as it allows for more efficient exploration of the parameter space by the optimization algorithm.

6. CONCLUSIONS

This work applied BO to PIC simulations of LPAs for medical applications, with a focus on transitioning from a previously performed optimization of an LPA for accelerating low-quality, high-energy, high-charge electron beams — aimed at producing radioisotopes via photonuclear reactions — to a beam with the quality and characteristics required for VHEE radiotherapy. This study aimed to generate electron beams in the 100–250 MeV range for VHEE radiotherapy. Specifically, the objective function was designed to produce an energy spectrum with a quasi-monoenergetic peak centered at 200 MeV. This required moving from the SM-LWFA to the bubble (blowout) regime, which enables the generation of quasi-monoenergetic beams. The gas target was changed from hydrogen (H_2) to a helium-nitrogen (He+N_2) mixture to allow controlled ionization injection.

Systematic exploration through 377 BO iterations produced an electron beam with approximately 1.86 nC total charge. The resulting energy spectrum is bimodal and quasi-monoenergetic, with peaks near 160 MeV and 197 MeV. Compared to a reference beam from the literature — characterized by a dominant low-energy peak (50–60 MeV) and a minor high-energy component - the beam obtained shows a reduced low-energy contribution and greater charge concentration in the therapeutic energy range. The result indicates improved alignment with VHEE therapy requirements, since the beam characteristics supported two clinical requirements: (1) sufficient charge for high-dose-rate FLASH therapy, and (2) localized, low-spread energy peaks that may enable depth-specific dose delivery using magnetic energy selection.

A correlation analysis using the Spearman coefficient was performed across all 377 simulations to examine the relationship between beam parameters and the optimization objective. The objective function showed strong positive correlations with both median ($r = 0.85$) and maximum ($r = 0.80$) electron energy. The analysis also identified a decoupling between the mechanisms controlling beam energy and beam charge.

The main limitation observed was the lack of convergence in the input parameters. This differs from the convergence achieved in the earlier Mo-99 study with a hydrogen target. The absence of convergence in the current study may be a consequence of the use of a He+N_2 gas mixture, which introduces additional ionization dynamics that affect laser propagation and bubble stability. Hence, rather than indicating a failure of the optimization algorithm, the absence of convergence may be caused by changes on the physical characteristics of the system. In the bubble regime, stable wakefield generation depends on forming a clean plasma cavity. Hydrogen facilitates this by being fully ionized early in the laser pulse, creating a uniform plasma channel. Helium, by contrast, has higher ionization thresholds, and its interaction with the laser pulse can distort the plasma structure, leading to instability or deviation from bubble-dominated acceleration. In some cases, acceleration in He+N_2 mixtures may occur through alternative mechanisms, such as direct laser acceleration (DLA).This outcome suggests that a future study

using a hydrogen and nitrogen (H_2 + N_2) mixture may be a viable path to achieving parameter convergence.

Future optimization efforts will prioritize the most influential parameters by analyzing their correlation with the objective function F_{obj}, while exploring other gas mixture and alternative objective function formulations to enhance convergence and beam quality. Additionally, the framework developed throughout this work will serve as the foundation for optimizing a LPA with parameters compatible with IPEN's forthcoming 15 TW laser system - expected to be operational in 2027 - aiming to guide the experimental development of LPA-based VHEE radiotherapy.

Bibliography

Abdel-Wahab, M., Gondhowiardjo, S. S., Rosa, A. A., Lievens, Y., El-Haj, N., Polo Rubio, J. A., Prajogi, G. B., Helgadottir, H., Zubizarreta, E., Meghzifene, A., Ashraf, V., Hahn, S., Williams, T., and Gospodarowicz, M. (2021). Global radiotherapy: Current status and future directions—white paper. *JCO Global Oncology*, (7):827–842.

Agnese Lagzda, R.M. Jones, D. A.-K. J. J. A. A. K. K. R. M. M. V. H. W. F. S. Z. (2017). Applications of Very High Energy Electrons (50-250 MeV) for radiotherapy. https://indico.cern.ch/event/577810/contributions/2491823/attachments/1424937/2185819/VHEEradiotherapy.pdf.

André, T., Andriyash, I. A., Loulergue, A., Labat, M., Roussel, E., Ghaith, A., Khojoyan, M., Thaury, C., Valléau, M., Briquez, F., Marteau, F., Tavakoli, K., N'Gotta, P., Dietrich, Y., Lambert, G., Malka, V., Benabderrahmane, C., Vétéran, J., Chapuis, L., El Ajjouri, T., Sebdaoui, M., Hubert, N., Marcouillé, O., Berteaud, P., Leclercq, N., El Ajjouri, M., Rommeluère, P., Bouvet, F., Duval, J. P., Kitegi, C., Blache, F., Mahieu, B., Corde, S., Gautier, J., Ta Phuoc, K., Goddet, J. P., Lestrade, A., Herbeaux, C., Évain, C., Szwaj, C., Bielawski, S., Tafzi, A., Rousseau, P., Smartsev, S., Polack, F., Dennetière, D., Bourassin-Bouchet, C., De Oliveira, C., and Couprie, M.-E. (2018). Control of laser plasma accelerated electrons for light sources. *Nature Communications*, 9(1).

Apaza Veliz, D. G., Wilches Visbal, J. H., Abrego, F. C., and Vega Ramírez, J. L. (2020). Monte carlo calculation of the energy spectrum of a 6 mev electron beam using penetration and energy loss of positrons and electrons code. *Journal of Medical Physics*, 45(2):116–122.

Arthur Accioly Rosa, Homero Lavieri Martins, L. P. M. S. C. S. M. V. I. O. (2022). *RT 2030: Plano de desenvolvimento da radioterapia para a próxima década*. Sociedade Brasileira de Radioterapia.

Assalmi, M., Alshreef, A., Jebbari, S., Arectout, A., Arce, P., and Diaf, E. Y. (2025). A novel approach with quadrupole magnets for precise deflection, scattering and focusing of very high energy electron beams (vhee). *Nuclear Analysis*, 4(2):100172.

Bakshy, Eytan; Kashin, K. B. M. (2019). Open-sourcing ax and botorch: New ai tools for adaptive experimentation. https://ai.meta.com/blog/open-sourcing-ax-and-botorch-new-ai-tools-for-adaptive-experimentation/.

Balandat, M., Karrer, B., Jiang, D. R., Daulton, S., Letham, B., Wilson, A. G., and Bakshy, E. (2020). BoTorch: A Framework for Efficient Monte-Carlo Bayesian Optimization. In *Advances in Neural Information Processing Systems 33*.

Bingham, R. and Trines, R. (2016). Introduction to plasma accelerators: the basics. *CERN Yellow Reports*, pages Vol 1 (2016): Proceedings of the 2014 CAS–CERN Accelerator School: Plasma Wake Acceleration.

Birdsall, C. K. and Langdon, A. B. (2004). *Plasma Physics via Computer Simulation*. Taylor Francis.

Bourhis, J., Montay-Gruel, P., Gonçalves Jorge, P., Bailat, C., Petit, B., Ollivier, J., Jeanneret-Sozzi, W., Ozsahin, M., Bochud, F., Moeckli, R., Germond, J.-F., and Vozenin, M.-C. (2019). Clinical translation of flash radiotherapy: Why and how? *Radiotherapy and Oncology*, 139:11–17.

Brigren, F. and Hallborn, H. (2021). Bayesian optimization of beam quality of plasma accelerated electron beams.

Bulanov, S. V. and Khoroshkov, V. S. (2002). Feasibility of using laser ion accelerators in proton therapy. *Plasma Physics Reports*, 28(5):453–456.

CERN (2022). Cern, chuv and theryq join forces for a world first in cancer radiotherapy. Technical report, CERN.

Corsini, R., Dyks, L., Farabolini, W., Gilardi, A., Korysko, P., and Sjobak, K. (2021). Status of vhee radiotherapy related studies at the clear user facility at cern. *Proceedings of the 12th International Particle Accelerator Conference*, IPAC2021:Brazil.

Esarey, E., Schroeder, C. B., and Leemans, W. P. (2009). Physics of laser-driven plasma-based electron accelerators. *Reviews of Modern Physics*, 81(3):1229–1285.

Favaudon, V., Caplier, L., Monceau, V., Pouzoulet, F., Sayarath, M., Fouillade, C., Poupon, M.-F., Brito, I., Hupé, P., Bourhis, J., Hall, J., Fontaine, J.-J., and Vozenin, M.-C. (2014). Ultrahigh dose-rate flash irradiation increases the differential response between normal and tumor tissue in mice. *Science Translational Medicine*, 6(245).

Giaccaglia, C., Bayart, E., Dubail, M., Varma, C., Heinrich, S., Gautier, J., Tafzi, A., Kononenko, O., Goddet, J.-P., Lamarre, I., Fouillade, C., and Flacco, A. (2025). Multiscale radiobiological assessment of laser-driven very high energy electrons versus conventional electrons.

Gonsalves, A., Nakamura, K., Daniels, J., Benedetti, C., Pieronek, C., de Raadt, T., Steinke, S., Bin, J., Bulanov, S., van Tilborg, J., Geddes, C., Schroeder, C., Tóth, C., Esarey, E., Swanson, K., Fan-Chiang, L., Bagdasarov, G., Bobrova, N., Gasilov, V., Korn, G., Sasorov, P., and Leemans, W. (2019). Petawatt laser guiding and electron beam acceleration to 8 gev in a laser-heated capillary discharge waveguide. *Physical Review Letters*, 122(8).

Hathaway, W., Kangas, R. A., and Raj, P. K. (1999). Clean air program : design guidelines for bus transit systems using hydrogen as an alternative fuel. https://rosap.ntl.bts.gov/view/dot/8427/dot_8427_DS1.pdf.

Hazra, D., Moorti, A., Mishra, S., Upadhyay, A., and Chakera, J. A. (2019). Direct laser acceleration of electrons in a high-z gas target and the effect of threshold plasma density on electron beam generation. *Plasma Physics and Controlled Fusion*, 61(12):125016.

INCA (2022). Brasil - estimativa dos casos novos: Estimativas para o ano de 2023. Technical report, Instituto Nacional do Câncer.

J Ferlay, M Laversanne, M. E. F. L. M. C. L. M. M. P. A. Z. I. S. F. B. (2024). Global cancer observatory: Cancer tomorrow. Technical report, Lyon, France.

Jaccard, M., Durán, M. T., Petersson, K., Germond, J., Liger, P., Vozenin, M., Bourhis, J., Bochud, F., and Bailat, C. (2018). High dose-per-pulse electron beam dosimetry: Commissioning of the oriatron ert6 prototype linear accelerator for preclinical use. *Medical Physics*, 45(2):863–874.

Jalas, S., Dornmair, I., Lehe, R., Vincenti, H., Vay, J.-L., Kirchen, M., and Maier, A. R. (2017). Accurate modeling of plasma acceleration with arbitrary order pseudo-spectral particle-in-cell methods. *Physics of Plasmas*, 24(3):033115.

Jalas, S., Kirchen, M., Messner, P., Winkler, P., Hübner, L., Dirkwinkel, J., Schnepp, M., Lehe, R., and Maier, A. R. (2021). Bayesian optimization of a laser-plasma accelerator. *Physical Review Letters*, 126(10).

Khan, F. M. (2003). *14. Electron Beam Therapy*, page 297–356. LIPPINCOTT WILLIAMS WILKINS, third edition.

Kim, H., Pathak, V., Hojbota, C., Mirzaie, M., Pae, K., Kim, C., Yoon, J., Sung, J., and Lee, S. (2021). Multi-gev laser wakefield electron acceleration with pw lasers. *Applied Sciences*, 11(13):5831.

Kirchen, M., Jalas, S., Messner, P., Winkler, P., Eichner, T., Hübner, L., Hülsenbusch, T., Jeppe, L., Parikh, T., Schnepp, M., and Maier, A. R. (2021). Optimal beam loading in a laser-plasma accelerator. *Physical Review Letters*, 126(17).

Kirchen, M., Lehe, R., Godfrey, B. B., Dornmair, I., Jalas, S., Peters, K., and Vay, J.-L. (2016). Stable discrete representation of relativistically drifting plasmas. *Physics of Plasmas*, 23(10):100704.

Kirchen, M., Lehe, R., Jalas, S., Shapoval, O., Vay, J.-L., and Maier, A. R. (2020). Scalable spectral solver in Galilean coordinates for eliminating the numerical Cherenkov instability in particle-in-cell simulations of streaming plasmas. *Physical Review E*, 102(1):013202.

Kokurewicz, K., Brunetti, E., Curcio, A., Gamba, D., Garolfi, L., Gilardi, A., Senes, E., Sjobak, K. N., Farabolini, W., Corsini, R., and Jaroszynski, D. A. (2021). An experimental study of focused very high energy electron beams for radiotherapy. *Communications Physics*, 4(1).

Kokurewicz, K., Brunetti, E., Welsh, G. H., Wiggins, S. M., Boyd, M., Sorensen, A., Chalmers, A. J., Schettino, G., Subiel, A., DesRosiers, C., and Jaroszynski, D. A. (2019). Focused very high-energy electron beams as a novel radiotherapy modality for producing high-dose volumetric elements. *Scientific Reports*, 9(1).

Kokurewicz, K., Welsh, G. H., Brunetti, E., Wiggins, S. M., Boyd, M., Sorensen, A., Chalmers, A., Schettino, G., Subiel, A., DesRosiers, C., and Jaroszynski, D. A. (2017). Laser-plasma generated very high energy electrons (vhees) in radiotherapy. In Ledingham, K. W. D., editor, *Medical Applications of Laser-Generated Beams of Particles IV: Review of Progress and Strategies for the Future*. SPIE.

Labate, L., Palla, D., Panetta, D., Avella, F., Baffigi, F., Brandi, F., Di Martino, F., Fulgentini, L., Giulietti, A., Köster, P., Terzani, D., Tomassini, P., Traino, C., and Gizzi, L. A. (2020a). Toward an effective use of laser-driven very high energy electrons for radiotherapy: Feasibility assessment of multi-field and intensity modulation irradiation schemes. *Scientific Reports*, 10(1).

Labate, L., Palla, D., Panetta, D., Avella, F., Baffigi, F., Brandi, F., Di Martino, F., Fulgentini, L., Giulietti, A., Köster, P., Terzani, D., Tomassini, P., Traino, C., and Gizzi, L. A. (2020b). Toward an effective use of laser-driven very high energy electrons for radiotherapy: Feasibility assessment of multi-field and intensity modulation irradiation schemes supplementary materials. *Scientific Reports*.

Lehe, R., Kirchen, M., Andriyash, I. A., Godfrey, B. B., and Vay, J.-L. (2016a). A spectral, quasi-cylindrical and dispersion-free Particle-In-Cell algorithm. *Computer Physics Communications*, 203:66–82.

Lehe, R., Kirchen, M., Vay, J.-L., Jalas, S., and Peters, K. (2016b). Numerical dispersion of spectral solvers and its mitigation in the Galilean frame. *Physical Review E*, 94(5):053305.

Lin, B., Gao, F., Yang, Y., Wu, D., Zhang, Y., Feng, G., Dai, T., and Du, X. (2021). Flash radiotherapy: History and future. *Frontiers in Oncology*, 11.

Lv, Y., Lv, Y., Wang, Z., Lan, T., Feng, X., Chen, H., Zhu, J., Ma, X., Du, J., Hou, G., Liao, W., Yuan, K., and Wu, H. (2022). Flash radiotherapy: A promising new method for radiotherapy (review). *Oncology Letters*, 24(6).

Maity, S., Mondal, A., Vishnyakov, E., and Molodozhentsev, A. (2024). Parametric analysis of electron beam quality in laser wakefield acceleration based on the truncated ionization injection mechanism. *Plasma Physics and Controlled Fusion*, 66(3):035012.

Maldonado, E. P., Samad, R. E., Zuffi, A. V. F., dos Santos, J. R., and Dias Vieira, N. (2023). Impact of he+n2 concentration on self-modulated laser wakefield acceleration driven by pulses of a few tw. *Journal of the Optical Society of America B*, 40(4):C141.

Maughan, R. L. (2022). Proton Therapy: Behind the Scenes | OncoLink — oncolink.org. https://www.oncolink.org/cancer-treatment/radiation/types-of-radiation-therapy/proton-therapy/overviews-of-proton-therapy/proton-therapy-behind-the-scenes.

Monzac, J., Smartsev, S., Huijts, J., Rovige, L., Andriyash, I. A., Vernier, A., Tomkus, V., Girdauskas, V., Raciukaitis, G., Mackevičiūtė, M., Stankevic, V., Cavagna, A., Kaur, J., Kalouguine, A., Lopez-Martens, R., and Faure, J. (2024). Optical ionization effects in khz laser wakefield acceleration with few-cycle pulses. *Physical Review Research*, 6(4).

New Jersey Department of Health (2006). Hazardous substance fact sheet. https://nj.gov/health/eoh/rtkweb/documents/fs/0972.pdf.

Nunes, B. S. (2023). Bayesian optimization of beam quality of plasma accelerated electron beams.

Panaino, C. M. V., Piccinini, S., Andreassi, M. G., Bandini, G., Borghini, A., Borgia, M., Di Naro, A., Labate, L. U., Maggiulli, E., Portaluri, M. G. A., and Gizzi, L. A. (2025). Very high-energy electron therapy toward clinical implementation. *Cancers*, 17(2):181.

Pukhov, A., Gordienko, S., Kiselev, S., and Kostyukov, I. (2004). The bubble regime of laser–plasma acceleration: monoenergetic electrons and the scalability. *Plasma Physics and Controlled Fusion*, 46(12B):B179–B186.

Ring, R., Stott, J., and Hales, C. (2008). Modeling the risk of fire/explosion due to oxidizer/fuel leaks in the ares i interstage.

Svendsen, K., Guénot, D., Svensson, J. B., Petersson, K., Persson, A., and Lundh, O. (2021). A focused very high energy electron beam for fractionated stereotactic radiotherapy. *Scientific Reports*, 11(1).

Tajima, T. and Dawson, J. M. (1979). Laser electron accelerator. *Physical Review Letters*, 43(4):267–270.

Vieira Junior, N. D. and Samad, R. E. (2024). Implantação de um laser de altíssima intensidade como uma infraestrutura científica multiusuário no brasil.

Vozenin, M.-C., Hendry, J., and Limoli, C. (2019). Biological benefits of ultra-high dose rate flash radiotherapy: Sleeping beauty awoken. *Clinical Oncology*, 31(7):407–415.

Wang, J. (2020). An intuitive tutorial to gaussian process regression.

Wenz, J. and Karsch, S. (2020). Physics of laser-wakefield accelerators (lwfa).

Whitmore, L., Mackay, R. I., van Herk, M., Jones, J. K., and Jones, R. M. (2021). Focused vhee (very high energy electron) beams and dose delivery for radiotherapy applications. *Scientific Reports*, 11(1).

Yan, S., Ngoma, T. A., Ngwa, W., and Bortfeld, T. R. (2023). Global democratisation of proton radiotherapy. *The Lancet Oncology*, 24(6):e245–e254.

A. APPENDIX A - BOOK CHAPTER

Optimizing Laser-Plasma Accelerators for Medical Radioisotope Production

16 Optimizing Laser-Plasma Accelerators for Medical Radioisotope Production

Samara Prass dos Santos
Bruno Silveira Nunes
Ricardo Elgul Samad
Nilson Dias Vieira Jr.
Mirko Salomón Alva-Sánchez
Alexandre Bonatto

Abstract:
Radiopharmaceuticals, used in nuclear medicine, are formed by drugs and radioisotopes, the latter being mainly produced by nuclear fission of highly enriched uranium, which produces a large amount of radioactive waste. A promising alternative for producing ^{99}Mo, which decays to ^{99m}Tc – the most used radioisotope in nuclear medicine – without relying on uranium fission, is photoactivation via laser-plasma accelerators. In light of these factors, this work proposes using Bayesian optimization in particle-in-cell simulations of a symmetric gas target for a laser-plasma accelerator, to enhance the radioisotope ^{99}Mo yield. To produce Gaussian pulses with a length of 15 μm (50 fs) and 7 μm in waist radius, a laser with a peak power of 5 TW was chosen, operating with high repetition rates in the self-modulated regime. It was possible to obtain an electron beam with a charge of 544 pC, 15.1 MeV of median energy, and 59 MeV of maximum energy, all considering electrons above the threshold of 8 MeV, for producing of bremsstrahlung photons to photoactivate the nuclear reaction to generate the ^{99}Mo.
Keywords: Bayesian optimization, particle-in-cell simulation, laser-plasma acceleration, photoactivation, electron beam.
Sustainable Development Goals (SDG): 3. Good Health and Well-being; 9. Industry, Innovation, and Infrastructure; 12. Responsible Consumption and Production.

16.1 Introduction

16.1.1 Radioisotopes in nuclear medicine

The clinical scenario in health centers is characterized by the need to use technologies capable of diagnosing and treating illnesses, such as neurological and cardiac diseases and certain types of cancer [IAEA, 2017]. For this purpose, nuclear medicine, a specialized medical field, employs radiopharmaceuticals that can be administered to patients either intravenously or orally. [SHNEIDER, 2005].

Radiopharmaceuticals are radioisotopes linked to medicines, and each organ will capture and metabolize these radioactive compounds in a specific way. In this way, radiopharmaceutical allows the observation of physiological functions and metabolic activity, as well as exploring the health of organs individually and promoting their treatment [IAEA, 2017]. This feat is possible due to the emission of radiation (electromagnetic and/or corpuscular waves) from the specific location at which the radiopharmaceutical is fixed in the human body [ELISA, 2018].

In general, for diagnostic purposes, radioisotopes that emit β^+ particles and/or γ rays are used, while, for therapy, radioisotopes that emit Auger electrons and β^- particles are administered. Considering a global scope, Technetium-99m (^{99m}Tc, half-life of 6h) is the most used, mostly being applied in scintigraphy procedures [World Nuclear Association, 2023].

^{99m}Tc is produced in ^{99}Mo/^{99m}Tc generators, while ^{99}Mo (half-life of 66h) is mainly produced in nuclear reactors through the fission of highly-enriched uranium (^{235}U) [IAEA 2001], which results in the formation of different radioisotopes, including ^{99}Mo (~6% of the yield [ZOLLE, 2007]. However, this method has several aggravating factors, the main ones being the generation of radioactive waste (especially the radioisotopes with long decay times) [World Nuclear Association, 2023], the need to transport highly radioactive material over long distances [CHO, 2010], and the elimination of highly-enriched uranium due to international nuclear non-proliferation policies [National Research Council, 2009]. Therefore, it is necessary to encourage research aimed at exploring alternatives to uranium-based production methods to find more ecological solutions that meet the growing demand for ^{99m}Tc.

16.1.2 Laser wakefield accelerators and photoactivation

A promising alternative for producing the radioisotope ^{99}Mo without the need for radioactive uranium and, consequently, excluding the aforementioned challenges, is by photonuclear reactions (photoactivation). In particular, the ^{100}Mo(γ, n)^{99}Mo reaction route has a high cross-section for photons with energies between 8 MeV and 20 MeV, peaking at approximately 14.5 MeV. Bremsstrahlung photons with energies within this range could be generated by impinging an SM-LWFA-accelerated electron beam in a tantalum (Ta) converter, positioned prior to a Mo target. For this application, low-quality electron beams, with high divergence and energy spread, may suffice, provided they can generate a high flux of bremsstrahlung photons. Such beams could be produced using compact laser wakefield accelerators (LWFA), capable of providing acceleration gradients in the order of hundreds of GeV/m [TAJIMA, 1979; ESAREY, 2009]. Moreover, modern laser systems, with peak powers ranging from 1 TW to 10 TW could be used to build laser wakefield accelerators in the self-modulated regime (SM-LWFA) [KRALL, 1993; FISHER, 1996; MALDONADO, 2021], operating at repetition rates of a few kHz [ROVIGE, 2020].

16.1.3 Particle-In-Cell Simulations and Bayesian Optimization

Despite impressive experimental results, LWFA technology is still under development. Hence, there is currently no straightforward methodology to address the complexity and instabilities that arise from the intricate, nonlinear laser-plasma coupled dynamics. One way to simulate and understand the phenomena of laser-plasma electron acceleration is through particle-in-cell (PIC) simulations, which can describe the self-consistent dynamics of charged particles in electromagnetic fields. However, due to the high computational cost of PIC simulations, and the large parameter space associated with the laser and plasma characteristics that will determine the acceleration of electrons in an SM-LWFA, conventional parameter scans – in which a large number of simulations are executed to cover a vast grid of possible combinations – is not an efficient approach. On the other hand, Bayesian Optimization, which is an algorithm capable of optimizing non-trivial multidimensional functions [BROCHU, 2010], may be an excellent alternative for this purpose [JALAS, 2021]. By using Bayesian optimization, the input values to be adopted in the next PIC simulation are determined by the algorithm, based on the previous existing results, aiming to maximize an objective function based on the desired

LWFA output properties such as the energy and charge of the LWFA-accelerated electron beam.

Enabling the production of ^{99}Mo via LWFA-accelerated electrons (rather than using highly-enriched uranium for this purpose) would have a positive impact on the environment, allowing the improvement of quality of life and health by using and producing resources responsibly, as well as promoting innovation in this industry, these being crucial points in UN sustainable development goals [UN, 2018]. Thus, to make plausible the attainment of an electron beam with the necessary characteristics to enable the production of the radioisotope ^{99}Mo via photoactivation, this chapter aims to determine the optimal parameters of a laser-driven plasma accelerator using the Bayesian Optimization algorithm, based on data from PIC simulations.

16.2 Optimization of a Symmetric Trapezoidal Gas Profile

The workflow of this work is depicted in Figure 2.1. As an initial step, a database is formed, initiating the optimization algorithm from a set of results from PIC simulations executed with input parameter values randomly chosen within their previously determined variation ranges. The objective function value is then calculated using the output parameters of each PIC simulation, in this case, obtained from the energy spectrum of the accelerated electron beam. Based on the available data points, the objective function is approximated using a probabilistic model, in this case, Gaussian process regression (GPR), enabling the use of Bayesian optimization. The acquisition function, computed from GPR parameters, determines the next set of input parameters to be sampled. Each iteration of the optimization process generates the initial condition (a set of input parameters) for a new PIC simulation, whose results will be used to calculate the objective function and update the database. This loop is repeated until convergence – of the objective function, around the highest observed values – is attained.

Figure 2.1. Flowchart of the Bayesian optimization process, coupled with PIC simulations.

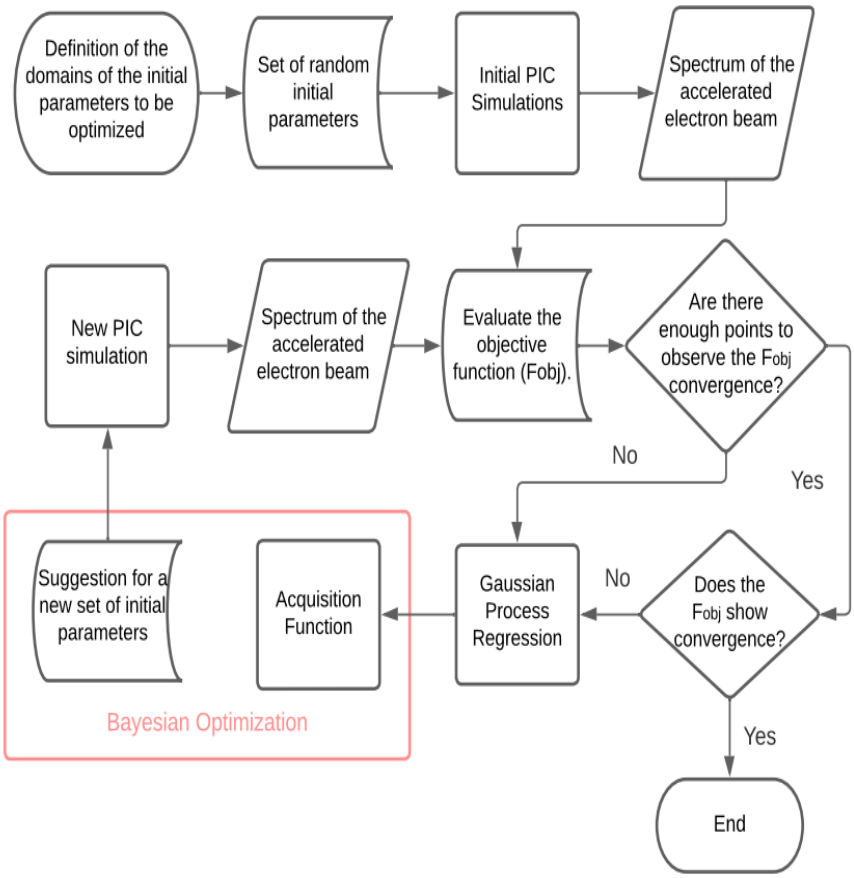

The Fourier-Bessel Particle-In-Cell (FBPIC) code [LEHE, 2016] was employed in this study. It is developed in the Python programming language and utilizes a cylindrical grid, which is suitable for the laser pulse envelope due to the inherent symmetries in this coordinate system. Simulations were conducted on the Santos Dumont Supercomputer at the Laboratório Nacional de Computação Científica (LNCC). To avoid excessive disk space usage, only two files were saved per simulation during the Bayesian optimization process, with the first file saved at the initial simulation time and the second file recorded at the final time.

A crucial step for the application of Bayesian optimization is the definition of an objective function. In order to establish a connection between the initial quantities in PIC simulations and the resulting electron beam in each simulation, the objective function was defined as

$$F_{obj} = \max \sum_{i}^{N_{bins}} E_i Q_i, \quad E_i > 8\,\mathrm{MeV},$$

where E_i [MeV], Q_i [nC], and N_{bins} are, respectively, the energy, the total charge of particles with that energy, and the number of bins in the histogram (energy spectrum) of the accelerated beam. In this work, N_{bins} = 200 was adopted. Among the available kernels, the Matérn kernel with the parameter nu ($\boldsymbol{\nu}$), which controls the smoothness of the learned function, was employed with a value of 2.5. The upper confidence bound was defined as the acquisition function. Ten initial random simulations were performed. The target gas was H_2, with the symmetric trapezoidal profile presented in the work of Maldonado et al. This profile, illustrated in Figure 2.2, can be understood as a linear approximation of a Gaussian profile.

Figure 2.2. Initial gas density profile before ionization, with the focal position of the laser pulse represented by the green line.

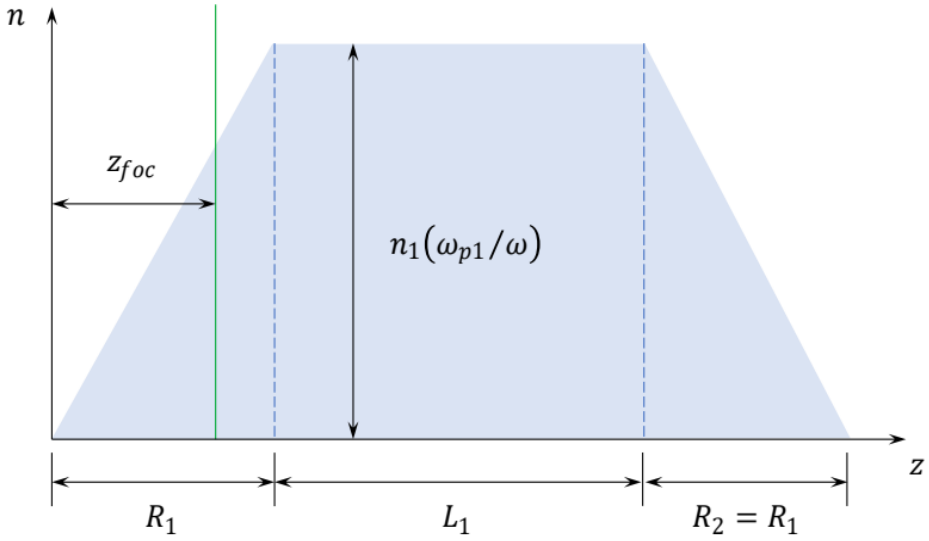

For the simulation, the following values were employed for the laser pulse: peak power P = 5 TW, Gaussian beam with a longitudinal length (FWHM) $c\tau$ = 15 μm, and waist radius r_0 = 7 μm. The laser was simulated to impinge on a gas with the profile shown in Fig. 2.2, which has a maximum density n_1 on the plateau, and up- and down-ramps with fixed horizontal lengths, R_1 = R_2 = 80 μm. As shown in Table 2.1, three input parameters were varied: the ratio between the plasma and laser angular frequencies, ω_{p1} / ω, the plateau length, L_1, and the laser focal position, z_{foc}. Each combination of these parameters creates an electron beam with specific characteristics. Table 2.1 also displays the variation ranges (intervals) of these input parameters, chosen based on previous existing studies of SM-LWFA [MALDONADO, 2021].

Table 2.1. List of input parameters and their variation intervals.

Parameter	Interval	Unit	Description
ω_{p1}/ω	0.15 , 0.40	–	Plasma and laser frequencies ratio at the plateau
L_1	30 , 60	µm	Plateau length
z_{foc}	30 , 60	µm	Laser pulse focal position

16.2.1 Results and discussion

Bayesian Optimization was applied using the Botorch package, which converged after approximately 150 iterations around $F_{obj} \approx (7.9 \pm 0.3)$ arb. unit, as shown in Figure 2.3. The non-convergence to the highest value attained, $F_{obj} \approx 9.6$ arb. unit, at iteration 135, can be explained by the significant impact of small variations in the initial parameters on the objective function output. Figure 2.4 summarizes these factors.

Figure 2.3. Evolution of the objective function (Fobj) along the iterations of the optimization algorithm. Convergence around (7.9 ± 0.3) arb. unit is observed after approximately 150 iterations.

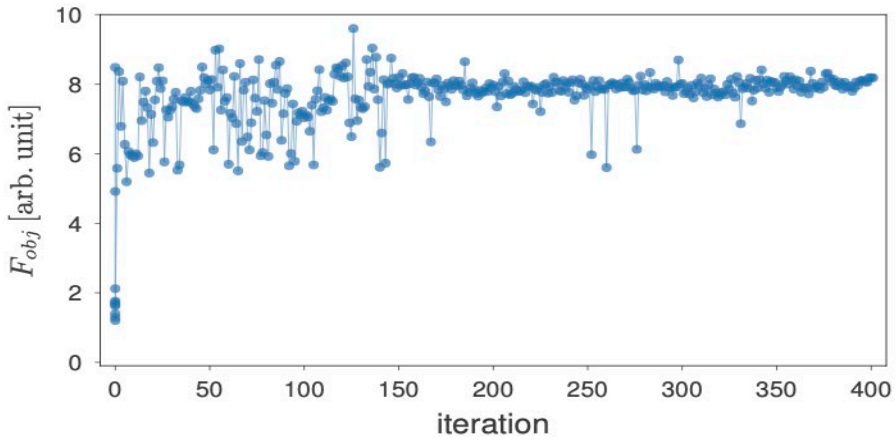

Analyzing Figure 2.4, rapid convergence is observed for the laser focal position ($z_{foc} \approx$ 57 µm), the ratio between plasma and laser angular frequencies (with fine-tuning in this parameter), and the plateau length ($L_1 \approx$ 47.5 µm). Figure 2.4(d) highlights the convergence towards an electron beam with a median energy of $\tilde{E} \approx$ 14.5 MeV. Additionally, in panel (e), convergence is observed for a range of maximum particle energies with 64 MeV < E_{max} < 70 MeV, and in image (f), convergence is seen for the total charge selected in the range of 450 pC < Q_{sel} < 500 pC, with a value of $Q_{sel} \approx$ 550 pC for the highest F_{obj} attained along the optimization. Finally, the lower panels, Figures 2.4(g) and (h), depict the optimal energy spectrum and gas-density profile.

Figure 2.4. Summary of results. Scatter plots of the objective function compared to (a) the laser focal position (z_{foc}), (b) plasma and laser frequencies ratio (ω_{p1}/ω), (c) plateau length (L_1), (d) median energy above 8 MeV ($\bar{E}_{sel}$), (e) maximum energy (E_{max}), and total charge above 8 MeV (Q_{sel}). Additionally, panels (g) and (h) show the optimal energy spectrum and gas-density profile, respectively. The optimal values for the input parameters are indicated in panel (h) as well.

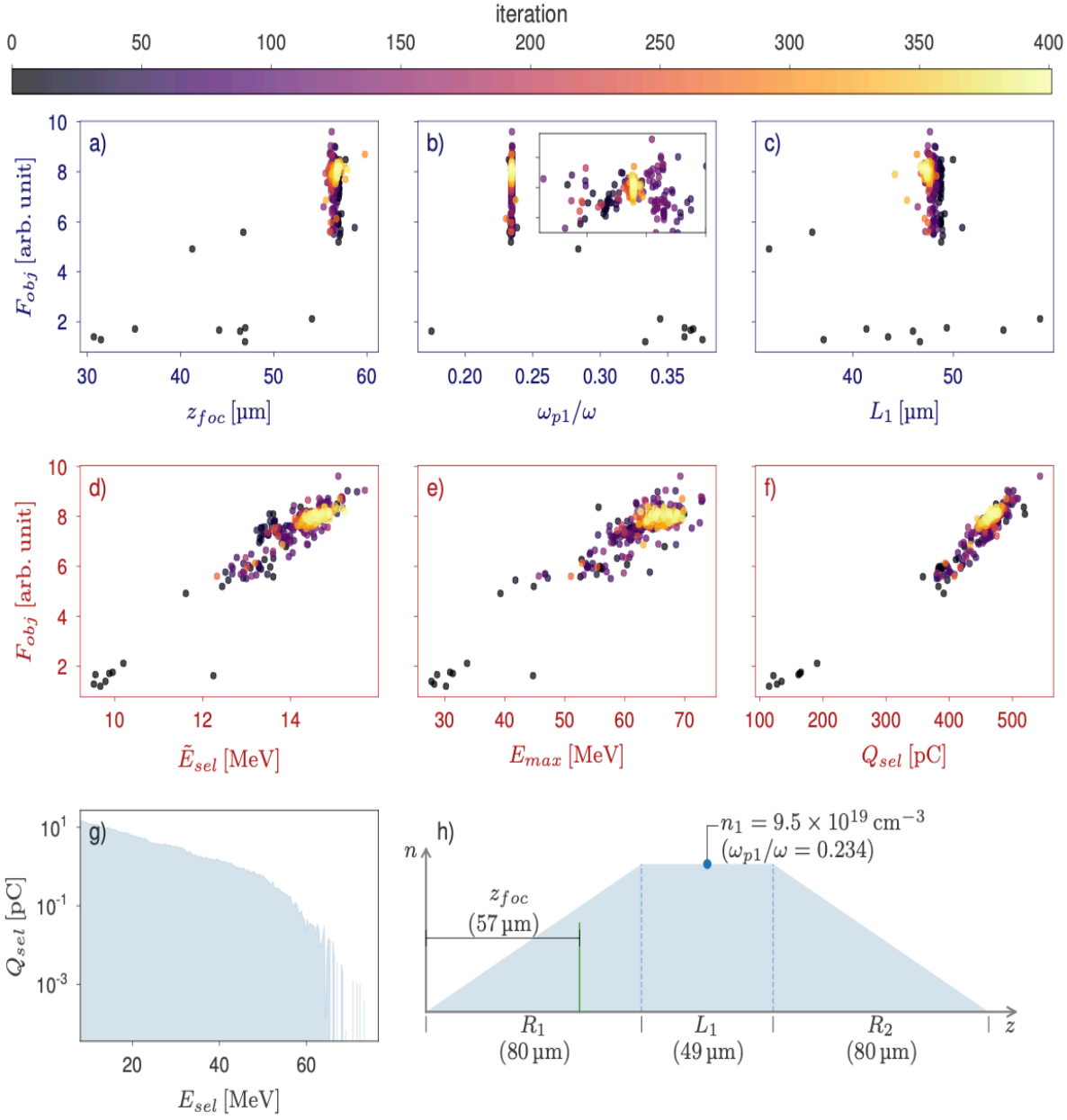

16.3 Conclusion and Future Directions

The objective of this work was to obtain an electron beam capable of generating photons with sufficient energy to produce the radioisotope ^{99}Mo through the ^{99}Mo(γ,n)^{100}Mo reaction pathway, using a Bayesian optimization algorithm based on PIC simulations. With the application of the algorithm in the described case, it was possible to achieve an electron beam

with a charge of 544 pC, a median energy of 15.1 MeV, and a maximum energy of 59 MeV, considering the 8 MeV threshold for bremsstrahlung photon production via photoactivation.

In future works, the intention is to use the optimal spectrum obtained in the TOPAS code to simulate the production and activity of the ^{99}Mo radioisotope. Additionally, it is worthwhile to explore different profiles, such as asymmetric trapezoidal profiles, given the influence of various plasma density regions on the dynamics of these systems.

16.4 Acknowledgments

The authors acknowledge the National Laboratory for Scientific Computing (LNCC/MCTI, Brazil) for providing HPC resources of the SDumont supercomputer (project LPA-FARMA), which were essential to the realization of this work.

References

BROCHU, E.; CORA, V.M.; DE FREITAS, N. A Tutorial on Bayesian Optimization of Expensive Cost Functions, with Application to Active User Modeling and Hierarchical Reinforcement Learning. 2010. DOI 10.48550/ARXIV.1012.2599. Available in: https://arxiv.org/abs/1012.2599

CHO, W-K. Radiation risk assessment for the transport of radioisotopes using KRI-BGMB(U) type containers. International Atomic Energy Agency: IAEA, In: Proceedings of IRPA12: 12. Congress of the International Radiation Protection Association: Strengthening Radiation Protection Worldwide - Highlights, Global Perspective and Future Trends 2010.

ELISA CRESTONI, M. Radiopharmaceuticals for Diagnosis and Therapy. Reference Module in Chemistry, Molecular Sciences and Chemical Engineering. [S.l.]: Elsevier, 2018. DOI 10.1016/b978-0-12-409547-2.14205-2. Available in: http://dx.doi.org/10.1016/B978-0-12-409547-2.14205-2.

ESAREY, E.; SCHROEDER, C. B.; LEEMANS, W. P. Physics of laser-driven plasma-based electron accelerators. Reviews of Modern Physics. [S. l.]: American Physical Society (APS), 27 ago. 2009. DOI 10.1103/revmodphys.81.1229. Available at: http://dx.doi.org/10.1103/RevModPhys.81.1229.

FISHER, D. L.; TAJIMA, T. Enhanced Raman forward scattering. Physical Review E. [S. l.]: American Physical Society (APS), 1 fev. 1996. DOI 10.1103/physreve.53.1844. Available in: http://dx.doi.org/10.1103/PhysRevE.53.1844.

IAEA Factsheet - Human Health. Nuclear Medicine for Diagnosis and Treatment. IAEA, 2017. Available in: https://www.iaea.org/sites/default/files/nuclear-medicine-for-diagnosis-and-treatment.pdf.

JALAS, S. et al. Bayesian Optimization of a Laser-Plasma Accelerator. Physical Review Letters, v. 126, n. 10, 11 mar. 2021.

KRALL, J.; TING, A.; ESAREY, E.; SPRANGLE, P. Enhanced acceleration in a self-modulated-laser wake-field accelerator. Physical Review E. [S. l.]: American Physical Society (APS), 1 set. 1993. DOI 10.1103/physreve.48.2157. Available in: http://dx.doi.org/10.1103/PhysRevE.48.2157.

LEHE, R.; KIRCHEN, M.; ANDRIYASH, I.A.; GODFREY, B.B.; VAY, J.-L. A spectral, quasi-cylindrical and dispersion-free Particle-In-Cell algorithm. Computer Physics Communications. [S. l.]: Elsevier BV, jun. 2016. DOI 10.1016/j.cpc.2016.02.007. Available in: http://dx.doi.org/10.1016/j.cpc.2016.02.007.

MALDONADO, E. P.; SAMAD, R. E.; BONATTO, A.; NUNES, R. P.; BANERJEE, S.; VIEIRA, N. D., Jr.. Study of quasimonoenergetic electron bunch generation in self-modulated laser wakefield acceleration using TW or sub-TW ultrashort laser pulses. AIP Advances. [S. l.]: AIP Publishing, 2021. DOI 10.1063/5.0052831. Available at: https://doi.org/10.1063/5.0052831.

National Research Council (US) Committee on Medical Isotope Production Without Highly Enriched Uranium. Medical Isotope Production without Highly Enriched Uranium. Washington D.C.: National Academies Press, 2009.

ROVIGE, L.; HUIJTS, J.; ANDRIYASH, I.; VERNIER, A.; TOMKUS, V.; GIRDAUSKAS, V.; RACIUKAITIS, G.; DUDUTIS, J.; STANKEVIC, V.; GECYS, P.; OUILLE, M.; CHENG, Z.; LOPEZ-MARTENS, R.; FAURE, J. Demonstration of stable long-term operation of a kilohertz laser-plasma accelerator. Physical Review Accelerators and Beams. [S. l.]: American Physical Society (APS), 14 set. 2020. DOI 10.1103/physrevaccelbeams.23.093401. Available in: http://dx.doi.org/10.1103/PhysRevAccelBeams.23.093401

SCHNEIDER, P.; BIKO, J.; HÄNSCHEID, H.; HILLIGER, S.; KOUTSAMPELAS, C.; KRANZFELDER, M.; LADNER, S.; REINERS, C.. The route of administration (oral vs intravenous) does not influence dose or outcome in Graves' disease and unifocal autonomy. European Journal of Nuclear Medicine and Molecular Imaging. [S. l.]: Springer Science and Business Media LLC, 10 mar. 2005. DOI 10.1007/s00259-005-1769-0. Available in: http://dx.doi.org/10.1007/s00259-005-1769-0.

TAJIMA, T.; DAWSON, J. M. Laser Electron Accelerator. Physical Review Letters. [S.l.]: American Physical Society (APS), 23 jul. 1979. DOI 10.1103/physrevlett.43.267. Available in: http://dx.doi.org/10.1103/PhysRevLett.43.267.

The Applications of Research Reactors: Report of an Advisory Group Meeting Held in Vienna, 4-7 October 1999. Vienna: IAEA, 2001.

United Nations, The 2030 Agenda and the Sustainable Development Goals: An opportunity for Latin America and the Caribbean (LC/G.2681-P/Rev.3), Santiago, 2018.

World Nuclear Association. Storage and Disposal of Radioactive Waste. Available in: https://worldnuclear.org/information-library/nuclear-fuel-cycle/nuclear-waste/storage-and-disposalof-radioactive-waste.aspx. Accessed in: december, 2023.

ZOLLE, I. Performance and Quality Control of the 99Mo/99mTc Generator. Technetium 99m Pharmaceuticals. [S. l.]: Springer Berlin Heidelberg, [s. d.]. DOI 10.1007/978-3-540-33990-8_5. Available in: http://dx.doi.org/10.1007/978-3-540-33990-8_5.

A. APPENDIX B - ARTICLE

Bayesian optimization of laser wakefield acceleration in the self-modulated regime (SM-LWFA) aiming to produce molybdenum-99 via photonuclear reactions

RESEARCH ARTICLE | MARCH 03 2025

Bayesian optimization of laser wakefield acceleration in the self-modulated regime (SM-LWFA) aiming to produce molybdenum-99 via photonuclear reactions

B. S. Nunes ; S. P. Santos ; R. P. Nunes ; C. Bonţoiu ; M. S. Alva-Sánchez ; R. E. Samad ; N. D. Vieira, Jr. ; G. Xia ; J. Resta-López ; A. Bonatto

Phys. Plasmas 32, 033101 (2025)
https://doi.org/10.1063/5.0244268

Physics of Plasmas ARTICLE pubs.aip.org/aip/pop

Bayesian optimization of laser wakefield acceleration in the self-modulated regime (SM-LWFA) aiming to produce molybdenum-99 via photonuclear reactions

Cite as: Phys. Plasmas **32**, 033101 (2025); doi: 10.1063/5.0244268
Submitted: 17 October 2024 · Accepted: 2 February 2025 ·
Published Online: 3 March 2025

B. S. Nunes,[1,2,3,a)] S. P. Santos,[2,3] R. P. Nunes,[3,4] C. Bonţoiu,[5,6] M. S. Alva-Sánchez,[2,3] R. E. Samad,[1] N. D. Vieira, Jr.,[1] G. Xia,[6,7] J. Resta-López, [8] and A. Bonatto[2,3,a)]

AFFILIATIONS

[1]Nuclear and Energy Research Institute, IPEN–CNEN/SP, São Paulo 05508-000, Brazil
[2]Graduate Program in Information Technology and Healthcare Management, Federal University of Health Sciences of Porto Alegre (UFCSPA), Porto Alegre 90050-170, Brazil
[3]Beam Physics Group, Federal University of Health Sciences of Porto Alegre (UFCSPA), Porto Alegre 90050-170, Brazil
[4]Federal University of Rio Grande do Sul (UFRGS), Porto Alegre 90035-190, Brazil
[5]Department of Physics, University of Liverpool, Liverpool L69 7ZE, United Kingdom
[6]The Cockcroft Institute, Sci-Tech Daresbury, Warrington WA4 4AD, United Kingdom
[7]Department of Physics and Astronomy, University of Manchester, Manchester M13 9PL, United Kingdom
[8]Instituto de Ciencia de los Materiales (ICMUV), Universidad de Valencia, 46071 Valencia, Spain

[a)]**Authors to whom correspondence should be addressed:** brunosnunes@usp.br and abonatto@ufcspa.edu.br

ABSTRACT

While laser wakefield acceleration (LWFA) in the bubble regime demands ultra-short, high-peak-power laser pulses, operation in the self-modulated regime (SM-LWFA) works with more relaxed pulse conditions, albeit at the cost of lower beam quality. Modern laser systems can deliver few-terawatt pulses with tens of femtoseconds at kilohertz repetition rates. These systems are well-suited for developing SM-LWFA applications where high average energy and charge are prioritized over beam quality. Such beams could be used to generate high-energy bremsstrahlung photons, capable of triggering photonuclear reactions to produce radioisotopes like molybdenum-99. This isotope decays into technetium-99m, the most widely used medical radioisotope, with over 30 million applications worldwide per year. This work explores the use of Bayesian optimization to maximize the energy and charge of electron beams accelerated via SM-LWFA. Particle-in-cell (PIC) simulations model a 5 TW, ∼60 fs-long (FWHM) Gaussian laser pulse, propagating through tailored hydrogen gas-density profiles. In these simulations, over multiple iterations, the algorithm optimizes a set of input parameters characterizing the gas-density profile and the laser focal position. Three distinct profiles, with lengths ranging from 200 to 400 μm and combining ramps and plateaus, were investigated. Optimal configurations produced electron beams with median energies ranging from 14 to 17 MeV and charges of 600 to 1300 pC, considering electrons with energies above 8 MeV. Preliminary estimates of molybdenum-99 yields for the optimal beams were obtained using their phase space data from PIC simulations as radiation sources in Monte Carlo simulations irradiating a tantalum-molybdenum target.

I. INTRODUCTION

Plasma-based accelerators[1] can provide gigavolts per meter accelerating fields, driven by either laser pulses[2] or charged particle beams[3] in plasmas. In both cases, as the driver propagates, it perturbs the plasma electron density in its wake, leading to the formation of high-amplitude wakefields that can be harnessed for charged-particle acceleration. Beam-driven wakefield accelerators (PWFA) have been employed as boosters to greatly increase the energy of a witness beam

at the expense of the driver's energy loss.[4,5] Another distinctive application of PWFA has been implemented in the AWAKE experiment,[6,7] in which a 400 GeV proton bunch drives a wakefield to accelerate electrons through a 10-m-long plasma. Nevertheless, while PWFA applications require a pre-accelerated beam driver, often generated by sizable accelerators, laser-driven wakefield accelerators (LWFA) have shown the capability of producing 8 GeV electron beams, self-injected from the plasma over a propagation distance of 20 cm.[8] Hence, laser-driven schemes might take greater advantage of the compactness anticipated in plasma-based accelerator applications.

Among the distinct regimes in which a LWFA can operate, the blowout or bubble regime[1] is known for being capable of producing high-energy electron beams, with low energy spread and emittance.[8] However, this regime typically requires laser pulses with high peak power, and lengths considerably shorter than the plasma wavelength. Such laser systems are costly, and often limited to operate at low repetition rates, in the sub-Hertz to Hertz domain. These properties may limit/restrict the use of the nonlinear regime for LWFA applications. On the other hand, the self-modulated regime (SM-LWFA), extensively explored in the 1990s[9–11] and later (with the advancement of laser technology) supplanted by the adoption of ultrashort pulses and the blowout regime, is now feasible with cost-effective laser systems at high repetition rates ($\sim$ kHz). However, this comes at the expense of producing lower quality beams, with larger energy spreads and higher emittances if compared to the blowout regime.[1,12]

In the SM-LWFA, the laser self-focusing effect produces a near diffraction limited spot, enhancing nonlinearities that cause the self-modulation phenomenon, leading to laser-plasma resonant interaction. When the self-focusing phenomenon balances the diffraction for several plasma periods, acceleration of multi-MeV bunched electron beams can be obtained, albeit with broader energy spectra and greater divergences compared to the blowout regime. Despite the lower beam quality, the SM-LWFA can be achieved using longer laser pulses (compared to the plasma wavelength) with relatively low (sub-terawatt to few-terawatt) peak powers. Since pulses with these properties can now be obtained at high ($\sim$ kHz) repetition rates,[13,14] the SM-LWFA might be suitable for applications that are not sensitive to the beam quality, such as the production of medical radioisotopes via photonuclear reactions. Among the possibilities, the production of molybdenum-99 (^{99}Mo, with a half-life of 66 h) stands out, as it subsequently decays into technetium-99m (^{99m}Tc, with a half-life of 6 h), the most widely used radioisotope in nuclear medicine, with over 30 million applications worldwide per year. Hence, obtaining ^{99}Mo via photonuclear reactions could enable an alternative, highly enriched-uranium-free production route for such radioisotope, thereby mitigating environmental and security concerns.[15]

^{99}Mo can be produced through the reaction ^{100}Mo(γ,n)^{99}Mo,[16–18] whose cross section is higher for photons with energies between 8 and 20 MeV, peaking at approximately 14.5 MeV. Bremsstrahlung photons with energies within this range could be generated by impinging a SM-LWFA-accelerated electron beam in a tantalum (Ta) converter, positioned prior to a Mo target. For this application, low-quality electron beams—with high divergence and energy spread—may suffice, provided they can generate a high flux of such bremsstrahlung photons. Due to the complex underlying physics of the SM-LWFA regime, the laser pulse dynamics, as well as the dominant acceleration mechanisms strongly depend on the laser and plasma-density initial profiles. Hence, it is a non-trivial task to determine the optimal conditions that allow for producing electron beams with the highest energies and charge for a given scenario.

A useful approach for examining how initial laser and plasma conditions affect the acceleration of electron beams is to combine particle-in-cell (PIC) simulations[19] with artificial intelligence algorithms. In particular, Bayesian optimization[20] can efficiently explore the extensive parameter space of laser and plasma settings, identifying conditions that may lead to improved outcomes toward in terms of the charge and energy spectrum of the electron beams. Bayesian optimization is known for its capability to handle functions with numerous inputs and unknown functional forms. It operates by incrementally building a dataset of function values, each new entry informing the next step in the search process. By using this iterative method, the algorithm can more effectively suggest parameter settings, even in scenarios with complex or less understood underlying relationships. This approach provides a balanced and steady progression toward finding more optimal configurations of laser and plasma parameters.

Machine learning algorithms have been applied to improve laser-plasma systems for a while.[21] Particularly, Bayesian optimization has recently been applied in two distinct LWFA experiments, in which the algorithm was used to control the parameters of a laser-plasma accelerator in laboratory.[22,23] In addition, studies demonstrated the use of multi-objective and multi-fidelity[24] and multitask[25] Bayesian optimization in PIC simulations.

In this study, Bayesian optimization is employed to determine the optimal values of multiple input parameters, characterizing the gas-density profile (target) and laser focal position in particle-in-cell (PIC) simulations modeling a SM-LWFA. These optimal values correspond to those maximizing an objective function based on the charge and energy spectrum of the accelerated electron beams, obtained as outputs from PIC simulations. This study is structured as follows. Section II describes the physical model, detailing the adopted PIC simulation parameters and providing an overview of the Bayesian Optimization algorithm employed. Sections III, IV, and V introduce three distinct hydrogen gas-jet density profiles, referred to as cases 1, 2, and 3, as well as the corresponding Bayesian optimization results. The optimized density profiles for each case are then compared in Sec. VI. In addition to the properties of the optimal beams, this comparison examines the roles of the two "competing" acceleration schemes – LWFA and direct laser acceleration (DLA)[26–28]—and provides yield estimates of ^{99}Mo for each optimized profile. Finally, in Sec. VII, the conclusions and future directions are discussed.

II. THE MODEL

The physical system simulated in this work consists of a Gaussian laser pulse propagating through a transverse-homogeneous and longitudinally varying density distribution of non-ionized hydrogen, simulating targets that could be obtained by using supersonic gas jets,[29] either in continuous flow[30] or powered by rapid valves, enabling operation at frequencies on the order of kilohertz (kHz). While the laser initial peak power, pulse duration, and transverse size at focus (waist) are kept constant, its focal position along the target length is one of the parameters to be optimized. Moreover, to ensure the system remains in the SM-LWFA regime, the lower bound of the plasma-density domain to be investigated is defined in such way that its plasma wavelength is shorter than the laser pulse length (FWHM) associated with the chosen pulse duration.

Regarding the target geometry, three gas-density profiles are proposed and will be clearly defined and illustrated in the forthcoming figures: an asymmetric trapezoid (case 1), a profile featuring two plateaus connected by a down-ramp (case 2), and a profile also comprising two plateaus, connected by either an up-ramp or a down-ramp (case 3). The utilization of asymmetric de Laval nozzles,[31,32] featuring designs that are adjustable,[33] modular,[34] or staged,[35] enables the creation of tailored asymmetric gas-density profiles with distinct combinations of up- and down-ramps and plateaus, such as those investigated in this work. The height (i.e., the plasma density) and length of a plateau affect the wakefield amplitude and the LWFA dephasing length.[1] Up-ramps, on the other hand, serve a dual purpose. They not only can increase the energy gain by extending the dephasing length but also can help control the collimation and emittance of LWFA-accelerated electron bunches.[36,37] Conversely, down-ramps can cause the injection of a substantial quantity of electrons into the acceleration bubble, effectively increasing the bunch charge.[38,39] Additionally, a plasma-density decrease diminishes the phase velocity of the plasma wave,[40] affecting the dephasing length as well.[41] Given the complex dynamics of the laser pulse in the SM-LWFA, predicting the optimal lengths and heights of such ramps and plateaus is not straightforward. Hence, in this work the parameter space is systematically explored using Bayesian optimization, to identify configurations that maximize the energy and charge of the LWFA-accelerated electron bunches. This approach allows for the most favorable conditions to be determined in a data-driven manner, significantly reducing the computational efforts required for optimizing the SM-LWFA.

A. PIC simulations

PIC simulations were carried out using the Fourier-Bessel PIC (FBPIC) code,[42] which adopts a spectral solver that uses a set of 2D (RZ) grids, each of them representing an azimuthal mode m. Among the notable features of FBPIC are the mitigation of spurious numerical dispersion by its spectral solver algorithm, including the zero-order numerical Cherenkov effect,[43] and the implementation of the openPMD metadata standard.[44] The simulation domain, spatial resolution, number of azimuthal modes, and number of particles per cell adopted in the PIC simulations presented in this work are listed in Table I. To ensure reproducibility and minimize the effects of random fluctuations on the Bayesian optimization algorithm, a fixed random seed, arbitrarily selected, was adopted for all simulations, except where specified otherwise.

In all simulations, a 5 TW peak power laser pulse, linearly polarized in the x axis, propagates (along the z coordinate) through a density profile of non-ionized hydrogen. The laser pulse is defined as a Gaussian beam, focused to a waist of $w_0 = 7$ μm at a given focal position. As the laser propagates through the neutral-gas target, the local density of plasma electrons is calculated using the ADK ionization model.[45] In addition to being consistent with previous studies,[12,46–48] these parameters are compatible with the design of a SM-LWFA under development at the Center for Lasers and Applications of the Nuclear and Energy Research Institute (IPEN-CNEN/SP, Brazil).[49] Table II provides the set of laser parameters adopted in all PIC simulations performed. The laser focal position and the target profile, which are the parameters to be optimized, will be introduced in Sec. II B.

TABLE I. PIC parameters.

Parameter	Value	Unit	Description
z_{min}	−100	μm	Initial boundary of the longitudinal simulation domain
z_{max}	0	μm	Final boundary of the longitudinal simulation domain
r_1	20	μm	Simulation domain radius (case 1)
r_2, r_3	50	μm	Simulation domain radius (cases 2 and 3)
Δ_z	27	nm	Spatial resolution in z
Δ_r	33	nm	Spatial resolution in r
N_m	3	⋯	Number of azimuthal modes
N_{pz}	2	⋯	Particles per cell along z
N_{pr}	2	⋯	Particles per cell along r
$N_{p\theta}$	12	⋯	Particles per cell along θ

TABLE II. Laser parameters.

Parameter	Value	Unit	Description
P_L	5	TW	Initial peak power
λ_0	800	nm	Wavelength
z_0	−50	μm	Pulse centroid
τ	58.9	fs	Pulse duration (FWHM)
w_0	7	μm	Waist
a_0	1.74	⋯	Strength parameter
E_ℓ	313	mJ	Pulse energy

B. Bayesian optimization

In this study, the Bayesian optimization algorithm was implemented using the Botorch library,[50] aiming to maximize an objective function, F_{obj}, to be defined in terms of the energy and charge of the LWFA-accelerated beam. Utilizing data from an initial set of simulations, performed with input parameters randomly chosen within their variation ranges, the algorithm constructs a surrogate model via Gaussian process regression,[51] in order to predict the behavior of the objective function. Through iterative refinement, the Bayesian optimization algorithm efficiently explores the parameter space, progressively improving the surrogate model to identify the optimal parameters that maximize F_{obj}. Given $x_1, \ldots, x_k$ as the values of the k input parameters to be optimized, this model estimates the mean $\mu(x_1, \ldots, x_k)$ and standard deviation $\sigma(x_1, \ldots, x_k)$ of F_{obj} at unexplored points, representing its expected value and associated uncertainty, respectively. These results are then utilized to evaluate an acquisition function, which in turn is used to infer a new set of input parameters for the subsequent PIC simulation. In this work, the Upper Confidence Bound (UCB)[52] acquisition function has been adopted,

$$UCB = \mu(x_1, \ldots, x_k) + \sqrt{\beta_i}\,\sigma(x_1, \ldots, x_k), \tag{1}$$

$$\beta_i = 2\log\frac{N(i\pi)^2}{6\delta}, \tag{2}$$

TABLE III. Case 1: input parameters.

Parameter	Range	Unit	Description
z_{foc}	20, 160	μm	Laser focal position
ω_{p1}/ω	0.15, 0.40	⋯	Plasma-to-laser frequency ratio
R_1	40, 120	μm	Up-ramp length
L_1	40, 80	μm	Plateau length
R_2	40, 120	μm	Down-ramp length

where β_i is the trade-off parameter between mean and covariance,[52] which adjusts the balance between exploring new areas and exploiting known regions. Although β_i can be set as a constant, the functional form adopted here depends on the iteration number i, the total number of data points N, and a user-specified parameter δ, which affects the level of confidence in exploration, selected within the range $0 < \delta \leq 1$ (in this work, $\delta = 1$ was adopted). This adaptive approach aims to mitigate the risk of the optimization process becoming trapped in local maxima. By allowing β_i to increase over iterations, the method promotes exploration of less-explored regions, even if an early maximum is identified. However, this enforced exploration will impact the convergence process by increasing oscillations around the optimal value.

For each PIC simulation, the input parameters to be optimized are the ramps and plateaus specifications that define the adopted gas-density profile, alongside the laser focal position. Tables III, IV, and V list the input parameters associated with the three distinct profiles, cases 1, 2, and 3, respectively, to be examined in the following sections. The output parameters are extracted from the energy spectrum of the accelerated beam, obtained from PIC simulation results. Each spectrum is built as a 200-bin histogram, being Q_i and E_i the charge and kinetic energy, respectively, associated with the i-th bin. Regarding the optimization, an interesting choice of parameter to maximize is the laser-to-beam energy conversion efficiency,[53,54] η. This quantity can be expressed as the ratio of the total beam energy, $E_b = N_e\langle E\rangle$, to the laser pulse energy, E_ℓ, where N_e is the number of particles in the beam and $\langle E\rangle$ is the average energy per particle

$$\eta \equiv \frac{E_b}{E_\ell} = \frac{N_e\langle E\rangle}{E_\ell} = \frac{N_e}{E_\ell}\left(\frac{\sum_i Q_i E_i}{Q_t}\right) = \frac{1}{eE_\ell}\sum_i Q_i E_i. \tag{3}$$

Hence, while this work adopts the sum of charge-weighted energies as the objective function,

$$F_{\text{obj}} = \sum_i^{N=200} Q_i E_i, \quad E_i \geq 8\,\text{MeV}, \tag{4}$$

the optimization results are presented in terms of η, expressed as a percentage of the laser pulse energy. In Eq. (4), the threshold of 8 MeV ensures the production of electrons capable of contributing to photon production via the $^{100}\text{Mo}(\gamma, n)^{99}\text{Mo}$ reaction route[17] and prevents the algorithm from prioritizing low-energy bins with higher charge. To indicate the use of the 8 MeV threshold, the energy and charge are denoted as E_{sel} and Q_{sel}, respectively, in quantities and figures where the threshold is applied.

TABLE IV. Case 2: input parameters.

Physical parameter	Variation range	Unit	Description
z_{foc}	5, 200	μm	Laser focal position
ω_{p1}/ω	0.15, 0.40	⋯	Plasma and laser frequencies ratio at the first plateau
ω_{p2}/ω	0, ω_{p1}/ω	⋯	Plasma and laser frequencies ratio at the second plateau
R_1	10, 120	μm	First ramp length
L_1	0, 80	μm	First plateau length
R_2	10, 120	μm	Second ramp length
L_2	0, 60	μm	Second plateau length
R_3	0, 120	μm	Third ramp length

TABLE V. case 3: input parameters.

Physical parameter	Variation range	Unit	Description
z_{foc}	5, 200	μm	Laser focal position
ω_{p1}/ω	0.15, 0.40	⋯	Plasma and laser frequencies ratio at the first plateau
ω_{p2}/ω	0, 1	⋯	Plasma and laser frequencies ratio at the second plateau
R_1	10, 120	μm	First ramp length
L_1	0, 80	μm	First plateau length
R_2	10, 120	μm	Second ramp length
L_2	0, 60	μm	Second plateau length
R_3	0, 120	μm	Third ramp horizontal length

III. OPTIMIZATION OF A TRAPEZOIDAL GAS-DENSITY PROFILE (CASE 1)

The first investigated profile has a longitudinal trapezoidal shape, with up- and down-ramps free to have distinct, independently-optimized lengths, generalizing the symmetric profiles adopted in previous studies[12,36,55] to model the gas flow of submillimetric supersonic nozzles.[29,31] In this profile, illustrated in Fig. 1, a linear up-ramp increases the density of hydrogen atoms from zero to n_1, over a length R_1. The density remains constant at n_1 along a plateau of length L_1, linearly decreasing to zero over a down-ramp of length R_2. Figure 1 also illustrates the laser focal position, z_{foc}, and shows n_1 as a function of the plasma-to-laser frequency ratio, $n_1(\omega_{p1}/\omega)$. Since each hydrogen atom has a single electron, upon complete ionization, n_1 also represents the plasma electron density. Hence, a plasma frequency $\omega_{p1} = \sqrt{n_1 e^2/(\varepsilon_0 m_e)}$, where e is the elementary charge, ε_0 is the vacuum permittivity, and m_e is the electron rest mass, can be associated with n_1. Because this ratio characterizes the plasma's response to the laser pulse propagation (underdense for $\omega_{p1}/\omega < 1$, critical density at $\omega_{p1}/\omega = 1$, and overdense for $\omega_{p1}/\omega > 1$), it is adopted here as an input parameter rather than directly using the electron density n_1. Furthermore, for a given ω_{p1}/ω, the density n_1 can be readily calculated using the expression $n_1 = (\omega_{p1}/\omega)^2(2\pi c/\lambda)^2(\varepsilon_0 m_e/e^2)$, where c is the speed of light and λ is the laser wavelength. Table III specifies the ranges for optimizing z_{foc}, ω_{p1}/ω, R_1, L_1, and R_2, chosen based on initial simulations and typical values used in LWFA experiments and simulations with gas nozzle targets. The range interval for ω_p/ω presented in Table III corresponds to gas densities ranging from $n = 0.4 \times 10^{20}$ to $2.8 \times 10^{20}\,\mathrm{cm}^{-3}$, which can be experimentally obtained with de Laval nozzles.

Figure 2(a) depicts the iterative evolution of the objective function over more than 400 PIC simulations, each conducted with input parameters defined by the Bayesian optimization algorithm. While η initially exhibits a wide range of values, after approximately 40 iterations it stabilizes around an average of $\eta \simeq (2.6 \pm 0.3)$ %. The absence of a further increasing trend, even after 400 simulations, indicates that the algorithm has likely converged η to this value.

The post-convergence oscillations of η are affected by the choice of β_i, which was intended to mitigate the risk of the optimization becoming trapped in a local maximum. This parameter progressively increases the weight of $\sigma(x_1, \ldots, x_k)$, reinforcing exploration around the optimal regions identified by the algorithm. In order to evaluate the physical significance of these oscillations, the energy spectra of two

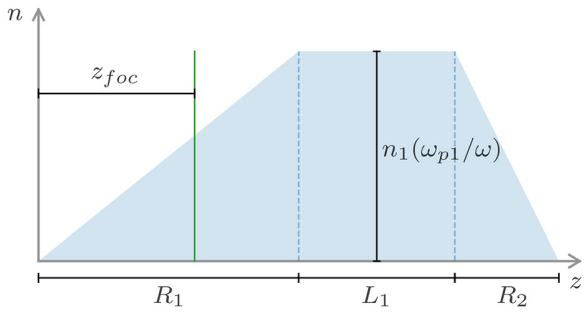

FIG. 1. Trapezoidal gas-density profile (case 1).

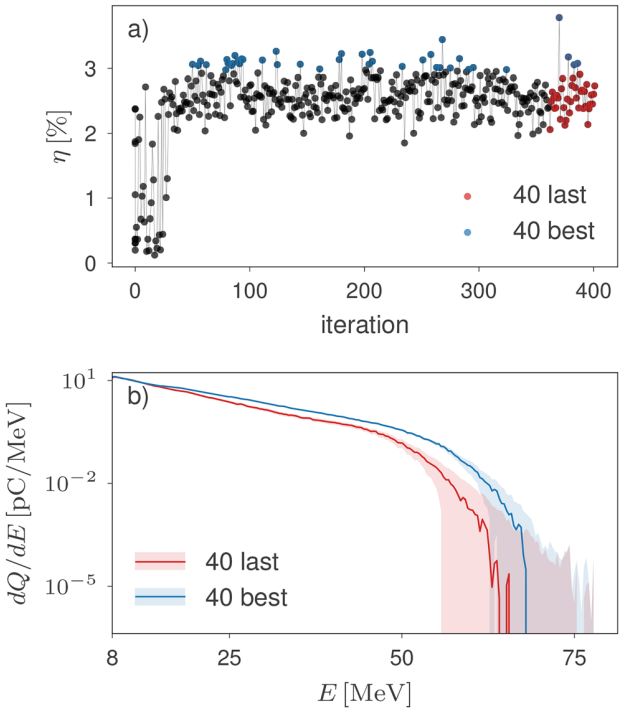

FIG. 2. (a) η along the optimization of case 1. Blue and red dots represent the 40 best and 40 last simulations, respectively. (b) Average energy spectra of the 40 best (blue line) and 40 last (red line) simulations, with shaded areas representing their 95% confidence intervals.

representative groups of 40 simulations (approximately 10% of the total number of simulations) are compared. The first group comprises the 40 simulations with the highest η values (40 best results), shown as blue dots in blue in Fig. 2(a), and the second group comprises the last 40 simulations (40 last results), shown as red dots in the same figure. Figure 2(b) shows the median spectra for both groups alongside their 95% t-student confidence intervals (colored areas). The 40 last features $\eta = 2.6\%$ and $Q_{sel} \simeq 380$ pC, whereas the 40 best presents $\eta = 3.1\%$ and $Q_{sel} \simeq 450$ pC, indicating a 20% increase in the laser-to-beam conversion efficiency and a 20% rise in selected charge for the 40 best group. Despite a close match at lower energies, discrepancies widen at higher energies, with the of the 40 best simulations showing greater charge than the 40 last ones. While the maximum energy in the 40 best also surpasses the 40 last, the difference is not statistically significant, as evidenced by the considerable overlap of the confidence intervals beyond approximately 60 MeV. Despite the aforementioned differences, the distributions of the input parameters for both groups, shown in Fig. 3, suggest they are physically similar.

Figures 4(a)–4(f) present scatter plots that track the evolution of the objective function with respect to each input parameter listed in Table III, throughout the iterations of the Bayesian optimization algorithm. The total length of the gas-density profile, L_{total}, plotted in Fig. 4(f), although not listed in Table III, is the sum of the up-ramp, plateau, and down-ramp lengths. The color scale is associated with the iteration number, with lighter colors corresponding to later iterations.

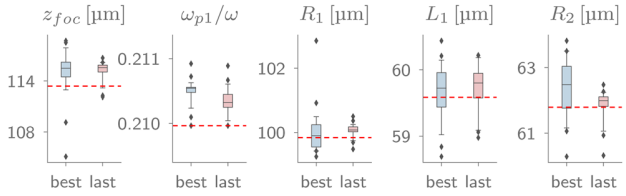

FIG. 3. Input parameter distributions for the 40 best (blue boxplots) and 40 last (light-red boxplots) simulations of case 1. The red dashed lines indicate the optimal values for each parameter.

In all panels, clusters of light-colored points, particularly at higher values of η, suggest convergence of the algorithm for the respective input parameters. Similar plots are shown in Figures 4(g)–4(i) for the output parameters, to characterize the accelerated electron beam in each simulation. Figure 4(g) shows the median energy above 8 MeV, $\tilde{E}_{sel}$. In this panel, a cluster of light-colored points indicates that beams with median energies between 13 and 17 MeV, and corresponding values of η between 2% and 3.5%, were produced following the convergence of the algorithm. Moreover, $\tilde{E}_{sel} = 16.9$ MeV was obtained for the highest value of η achieved. Figure 4(h) presents the maximum energies (E_{max}) obtained in each simulation. Although this parameter is not statistically significant, as only a few electrons achieve such energies, it is interesting to observe that, during convergence, maximum energies between 60 and 80 MeV were obtained, with $E_{max} = 73$ MeV for the simulation with the highest value of η achieved. Figure 4(i) depicts the selected charge (Q_{sel}) of the beams, considering only particles exceeding 8 MeV in energy. Selected charges between 400 and 600 pC were achieved during convergence, with the highest value obtained in the optimal simulation, that maximized η. Figures 4(g)–4(i) depict a clear improvement due to optimization, with darker dots at lower parameter values transitioning to brighter, clustered dots at higher values. Figure 4 is concluded with panels (j) and (k) presenting the optimal beam energy spectrum and gas-density profile, respectively.

The underlying physics of the optimal simulation of case 1 can be assessed by backtracking the trajectories and energy evolution of the electrons that constitute the accelerated beam, specifically those exiting the gaseous target with energies exceeding 8 MeV. Figures 5(a)–5(d) illustrate the plasma electron density normalized by the density of the first plateau, n_e/n_1, in a blue gradient scale. Backtracked electrons are depicted as colored dots, with a yellow-purple color scale representing their energies at each location. Additionally, contour lines for the laser strength parameter a_0, ranging from 1 (outermost) to 4 (innermost) in unitary steps, were added to show the laser envelope. Each panel is plotted at a distinct propagation distance z along the gas-density profile, illustrated in the upper, unlabeled panel of Fig. 5. In the labeled panels, the moving coordinate $\xi \equiv z - v_w t$ is adopted, where v_w is the velocity of the simulation moving window, chosen to approximately lock the laser pulse in the frame. Because the plasma density evolves along the pulse propagation, this velocity was approximated as the arithmetic mean of the initial (lower) velocity in the unperturbed plasma and the subsequent (higher) velocity in the perturbed plasma, $v_w = (c/2)\left(\sqrt{1-(\omega_p/\omega)^2} + \sqrt{1-0.2\,(\omega_p/\omega)^2}\right)$.

Figure 5(a) reveals a long and tightly focused laser pulse at the beginning of the density plateau ($z = 100\,\mu$m), evident from the a_0 contour lines. Within the laser pulse, the intense fields cause a near-complete depletion of the normalized plasma electron density (n_e/n_1), visualized as a white region. Despite this depletion, a small fraction of the electrons that will contribute to the final accelerated beam, most of them still with energies below 10 MeV (yellow to orange dots), can be seen gaining kinetic energy within this region, via DLA, as it will be discussed in Sec. VI. Along the plateau, the laser pulse drives an intense wakefield (not shown in Fig. 5), with a wavelength shorter than the laser envelope. The interaction between the long pulse and the disturbed plasma leads to laser self-modulation,[1] a process where the laser intensity becomes longitudinally modulated within the pulse envelope. The a_0 contour lines in Fig. 5(b), plotted at the end of the plateau ($z = 160\,\mu$m), depict laser pulse fragments with lengths comparable to the wakefield wavelength. These fragments act as a train of shorter pulses, driving bubbles in the normalized electron density (n_e/n_1) that roughly resemble those driven by a single short laser in the nonlinear regime. However, the variation and irregularity of these fragments during propagation degrade the wakefield and bubbles, significantly reducing the quality of the accelerated beam compared to the nonlinear regime. Within the bubbles, particularly the two central ones ($-55\,\mu\text{m} \le \xi \le -40\,\mu$m), electrons are self-injected at the rear, drifting rightward as they are accelerated to energies close to 50 MeV. Oscillations of the accelerated electrons around the propagation axis are likely induced by the laser's transverse fields, possibly with an additional contribution from betatron motion.[56] Along the down-ramp, as the density decreases, the wakefield wavelength and, consequently, the bubbles, become longer and eventually merge. Figure 5(c), plotted halfway through the down-ramp, depicts this process. While the contour lines show a laser envelope similar to the one observed in the previous panel, the effect of reducing the plasma density can be seen in the normalized electron density n_e/n_1. The two central bubbles shown in Fig. 5(b) have merged in a single longer bubble in Fig. 5(c), loaded with almost continuously distributed electrons along its length. While the contour lines depict a laser envelope similar to the one observed in the previous panel, the effect of reducing the plasma density can be seen in the normalized electron density n_e/n_1. The two central bubbles shown in Fig. 5(b) have merged into a single, longer bubble in Fig. 5(c), filled with a nearly continuous distribution of electrons along its length. The two regions containing electrons exceeding 50 MeV of kinetic energy (purple dots) were previously accelerated in individual bubbles before they merged. A key finding, unique to the optimal simulations, is the seamless transition of accelerated electrons between bubbles as they expand and merge, with the electrons maintaining their structure throughout their passage across the plasma. Figure 5(d) shows the electrons with energies exceeding 8 MeV ejected from the gas target after exiting the down-ramp. The backtracked electrons presented in the previous panels were selected from this panel. Outside the gas target, the beam transversely expands due to the absence of focusing forces.

IV. OPTIMIZATION OF A GAS-DENSITY PROFILE WITH TWO DESCENDING PLATEAUS (CASE 2)

If the long, fully loaded bubble observed in Fig. 5(c) could be maintained for a longer distance, the trapped electrons could potentially be accelerated to higher energies. This could be achieved by adding a second plateau, lower than the first one, at some point along the down-ramp. Such is the motivation for optimizing the gas-density profile shown in Fig. 6, with two plateaus connected by a down-ramp, resembling two merged asymmetric trapezoidal profiles. The input

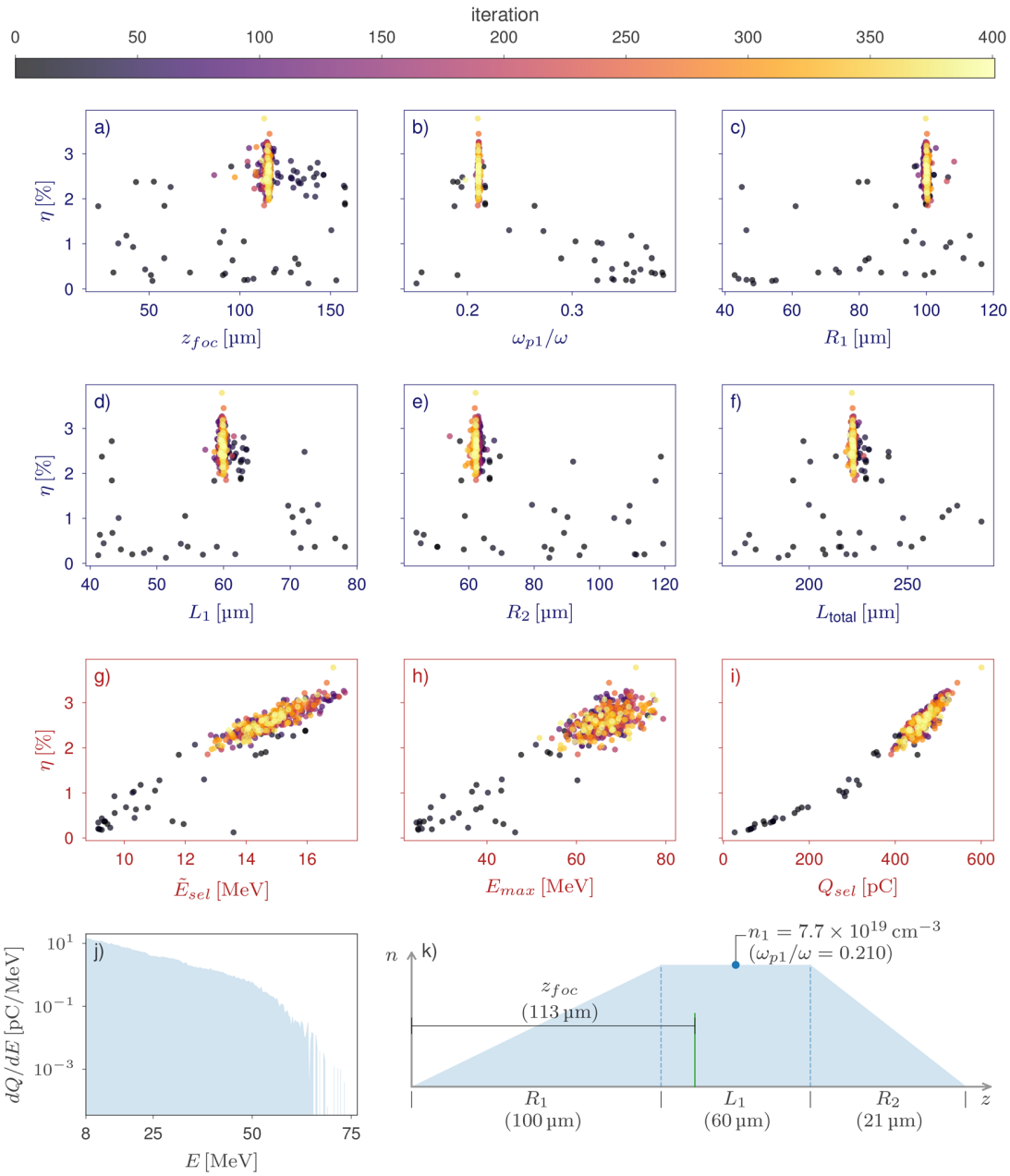

FIG. 4. Bayesian optimization of case 1, with a color scale indicating the algorithm iteration. Input parameters: η vs the (a) laser focal position, (b) plasma-to-laser frequency ratio at the plateau, and lengths of the (c) up-ramp, (d) plateau, and (e) down-ramp sections of the gas-density profile, along with the (f) total length of the profile. Output parameters: η vs the (g) median energy (above 8 MeV) $\tilde{E}_{sel}$ (h) maximum energy, and (i) selected charge Q_{sel}. Case 1 optimal: (j) energy spectrum and (k) gas-density profile, with the optimal values for the input parameters.

parameters, increased from six to eight with the addition of a second plateau and down-ramp, are listed in Table IV along with their respective variation ranges. While the first plateau maintains the limits specified in Table III, i.e., $0.15 \leq \omega_{p,1}/\omega \leq 0.40$, the second plateau's upper bound is constrained by the first, with $0 \leq \omega_{p,2}/\omega \leq \omega_{p,1}/\omega$.

Figure 7(a) illustrates the evolution of the objective function over the iterations while optimizing case 2. In the initial iterations, lower and highly variable values of η are observed as the algorithm explores the parameter space. However, after approximately 100 iterations, η values stabilize around $5.5 \pm 0.3\%$. This latter region, with reduced

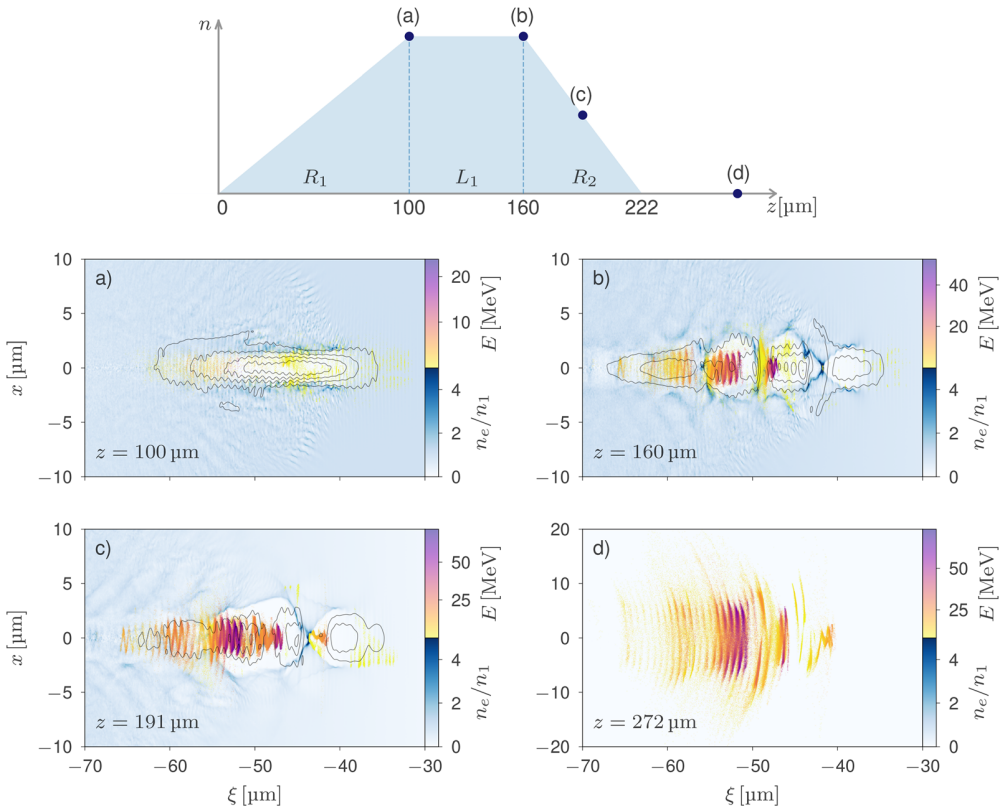

FIG. 5. Spatial evolution of the optimal simulation, case 1. The upper panel shows the propagation distances at which panels (a) to (d) were plotted. In these panels, the plasma electron density (normalized by the plateau density) is shown using a blue gradient scale, and the backtracked electrons, which will attain energies exceeding 8 MeV after ejection, are depicted as colored dots with a yellow-purple color scale representing their energies at the current propagation distance. Additionally, contour lines for a_0 ranging from 1 (outermost) to 4 (innermost), in unitary steps, depict the laser envelope at these distances.

variability compared to the initial iterations, indicates the exploitation phase, where the optimization process refines its search around higher values of the objective function, demonstrating an effective convergence toward more optimal solutions. The optimal simulation (iteration 373) attained $\eta \approx 6.3\%$, a value 67% higher than the best result obtained for case 1. The average spectra for the 40 best (blue dots) and 40 last (red dots) simulations, shown in Fig. 7(b), do not exhibit any statistically significant differences. The distributions of their input parameters, as illustrated in Fig. 8, are also compatible.

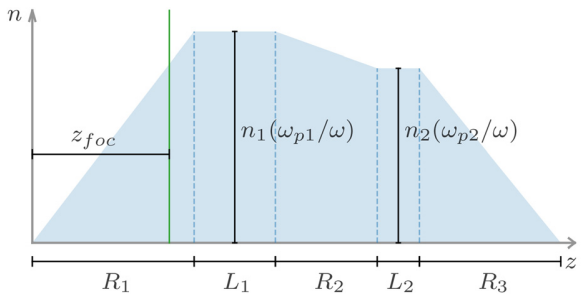

FIG. 6. Gas-density profile with two descending plateaus (case 2).

Figures 9(a)–9(i) show scatter plots of the objective function against the input parameters listed in Table IV, with the total length L_{total} obtained by adding the length of all ramps and plateaus. In all panels, narrow clusters of light-colored dots, located at higher values of η, indicate the optimal values of the input parameters. Figures 9(j)–9(l) present the beam output parameters accordingly. After convergence, Fig. 9(j) shows median energies (above 8 MeV) between 13 and 16 MeV, while Fig. 9(k) depicts maximum energies between 75 and 120 MeV. Additionally, Fig. 9(l) highlights selected charges from 800 to 1200 pC after convergence. In the optimal simulation of case 2 ($\eta = 6.3\%$), a median energy $\tilde{E}_{sel} = 14.6$ MeV, maximum energy $E_{max} = 81$ MeV, and selected charge $Q_{sel} = 999$ pC were attained. Despite the lower median energy compared to case 1, the 67% increase in the optimal charge in case 2 led to a higher value for the objective function. Additionally, the longer total length L_{total} also benefited case 2. To conclude Fig. 9, panels (m) and (n) display the optimal beam energy spectrum and gas-density profile, respectively.

Figure 10 displays the laser and plasma dynamics for the optimal simulation of case 2. Panels (a) to (c), plotted along the first plateau (L_1), exhibit behavior qualitatively comparable to Figs. 5(a) and 5(b),

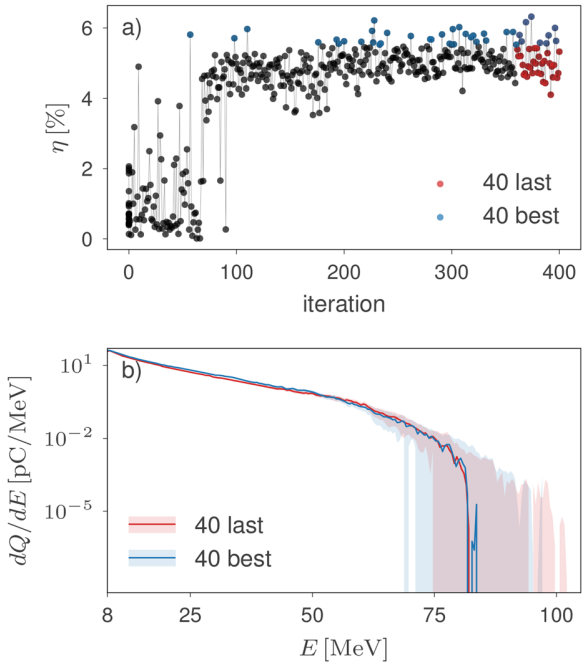

FIG. 7. (a) η along the optimization of case 2. Blue and red dots represent the 40 best and 40 last simulations, respectively. (b) Average energy spectra of the 40 best (blue line) and 40 last (red line) simulations, with shaded areas representing their 95% confidence intervals.

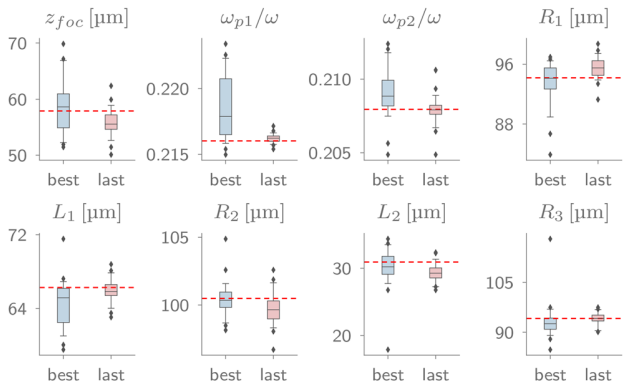

FIG. 8. Input parameter distributions for the 40 best (blue boxplots) and 40 last (light-red boxplots) simulations of case 2. The red dashed lines indicate the optimal values for each parameter.

showing the same region of the optimal profile in case 1. However, additional contour lines of a_0 reveal higher-intensity laser fragments after the self-modulation in case 2. Figures 10(d) and 10(e) show the laser descending the first density down-ramp (R_2). In panel (d), plotted in the middle of the descent, the plasma still contains three bubbles. Additionally, the more intense laser fragments are capable of accelerating electrons to higher energies, above 50 MeV, as indicated by the purple dots. Panel (e) shows that, at the end of the ramp and the beginning of the second plateau (L_2), the second and third bubbles, counted in the decreasing direction of ξ, are now merging into a single longer one. A notable difference observed in the optimal simulation of case 2, compared to case 1, is that the presence of a longer and less steep down-ramp allowed for a strong self-injection of electrons within the merging bubbles. Regarding the laser along the down-ramp R_2, while panel (d) still shows intense fragments, with lengths comparable to the bubbles, panel (e) displays a larger number of shorter fragments, with lengths now proportional to the laser wavelength. Although most of these fragments have lower intensities ($a_0 \gtrsim 1$), fragments with $a_0 \gtrsim 3$ are still capable of driving the observed bubbles up to the end of second plateau (L_2), as shown in Fig. 10(f). The eccentricity observed in this panel—the second bubble is slightly off-axis—intensifies in panels (g) and (f), plotted halfway down the final down-ramp (R_3) and outside the gaseous target, respectively. As a consequence, the accelerated beam, shown in the latter panel, exhibits significant transverse spreading.

V. OPTIMIZATION OF A GENERALIZED TWO-PLATEAU GAS-DENSITY PROFILE (CASE 3)

While case 2 constrains the second density plateau to be always lower than the first one ($0 \leq \omega_{p2}/\omega \leq \omega_{p1}/\omega$), case 3, illustrated in Fig. 11, adopts a generalized two-plateau gas-density profile. In this case, the second plateau is allowed to vary within a fixed range ($0 \leq \omega_{p2}/\omega \leq 1$, as shown in Table V), eliminating the variable, ω_{p1}/ω-dependent upper limit previously adopted.

Figure 12(a) shows convergence around $\eta \approx 7.6 \pm 0.4\%$ after approximately 70 iterations, with the optimal simulation (at iteration 142) achieving $\eta = 8.3\%$. In contrast to previous cases, optimization in case 3 stopped at 200 iterations. Given the achieved convergence and considering the behavior of previous cases, this early termination reduced computational costs without compromising the analysis. As shown in Fig. 12(b), the average spectra of the 40 best and 40 last simulations are statistically equivalent. In the previous two cases, the typical logarithmic decay shows a negative slope, indicating an exponential decrease in charge distribution dQ/dE with increasing energy, However, in case 3, this decay flattens out over certain energy ranges, forming distinct plateaus. There is an almost constant charge distribution between approximately 40 and 60 MeV, followed by a higher plateau between approximately 60 and 80 MeV. Figure 13 exhibits the input parameter distributions of the 40 best and 40 last simulations.

Figures 14(a)–14(i) show scatter plots of the laser-to-beam conversion efficiency against the input parameters from Table V, plus the total target length (L_{total}). By removing the constraint of a lower density in the second plateau from case 2, the optimization in case 3 resulted in a distinct configuration. The central ramp (R_2) transitioned from a down-ramp in case 2 to a longer and steeper up-ramp in case 3. Despite this, the optimal total length in case 3 (362 μm) is shorter than in case 2 (386 μm). Regarding the output beams, Fig. 14(j) shows median energies (above 8 MeV) converging around 16 MeV, with the optimal simulation achieving $\tilde{E}_{sel} = 16.7$ MeV. Figure 14(k) depicts maximum energies ranging from 80to 110 MeV after convergence, with the optimal simulation reaching a maximum energy of 87 MeV. In Fig. 14(l), total charges (above 8 MeV) varied from 1050 to 1310 pC after convergence, with $Q_{sel} = 1305$ pC for the optimal simulation (an approximate 30% increase compared to case 2). The optimal electron beam spectrum and the corresponding gas-density profile are presented in (m) and (n), respectively.

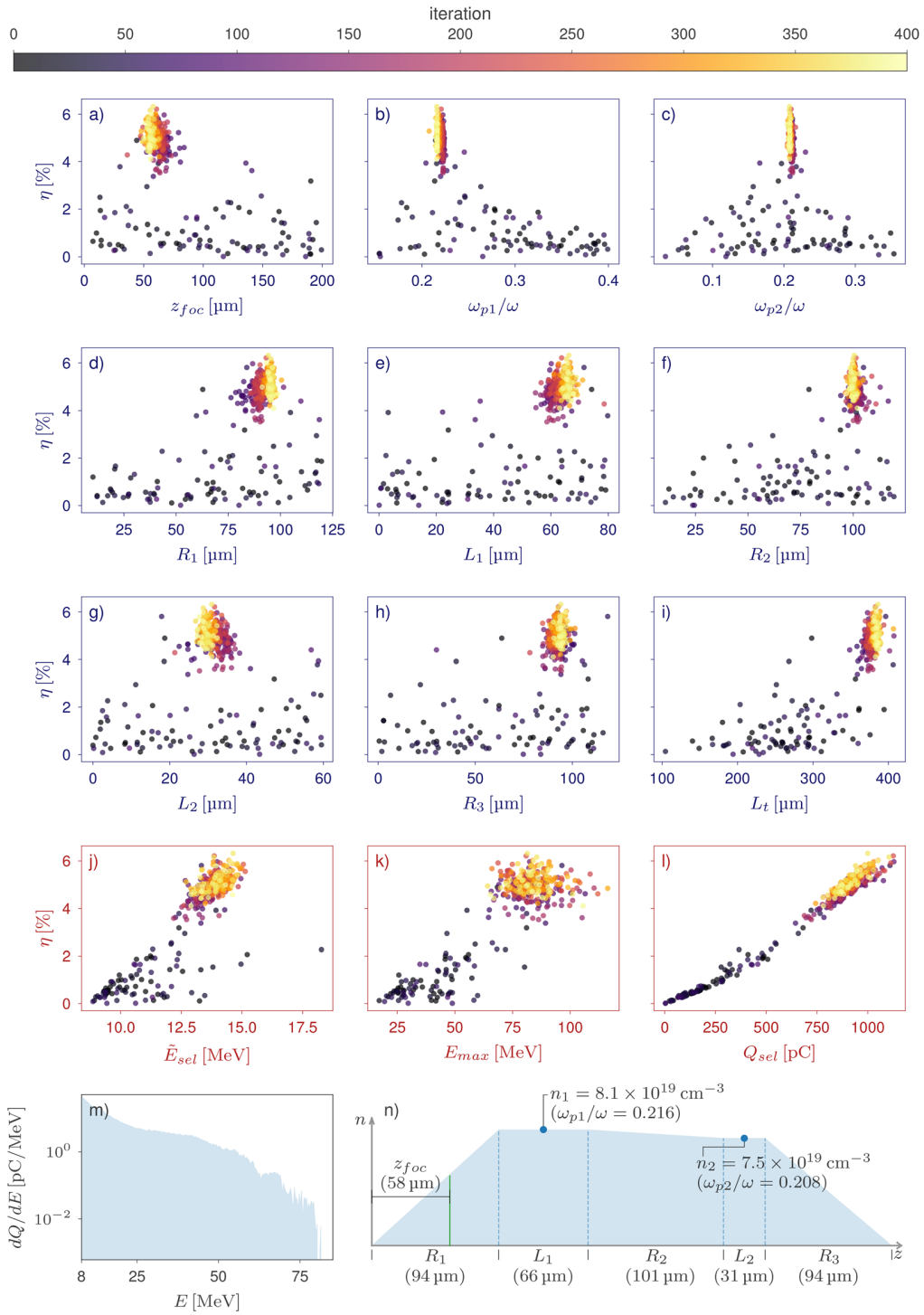

FIG. 9. Bayesian optimization of case 2, with a color scale indicating the algorithm iteration. Input parameters: η vs the (a) laser focal position, plasma-to-laser frequency ratio in the (b) first and (c) second plateaus, lengths of the (d) first ramp, (e) first plateau, (f) central ramp, (g) second plateau, (h) last ramp, and (i) total profile. Output parameters: η vs the (j) median energy (above 8 MeV) $\tilde{E}_{sel}$, (k) maximum energy, and (l) selected charge. Case 2 optimal: (m) energy spectrum and (n) gas-density profile, with optimal input parameters.

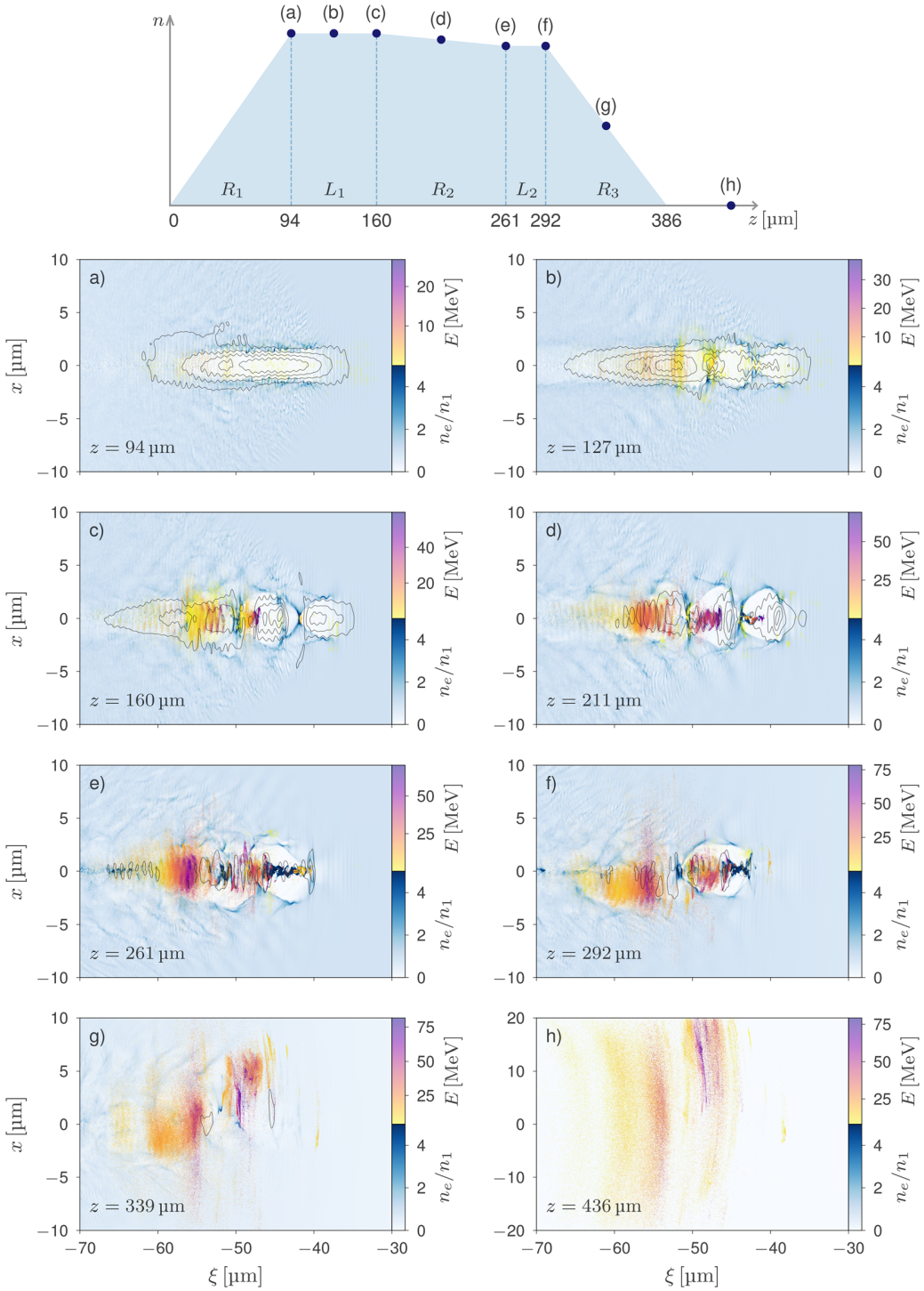

FIG. 10. Spatial evolution of the optimal simulation, case 2. The upper panel shows the propagation distances at which panels (a) to (h) were plotted. In these panels, the plasma electron density, normalized by the plateau density, is shown using a blue gradient scale. The backtracked electrons, which will attain energies exceeding 8 MeV after ejection, are depicted as colored dots with a yellow-purple color scale representing their energies at the current propagation distance. Additionally, contour lines for a_0 ranging from 1 (outermost) to 4 (innermost) were added to show the laser envelope at these distances.

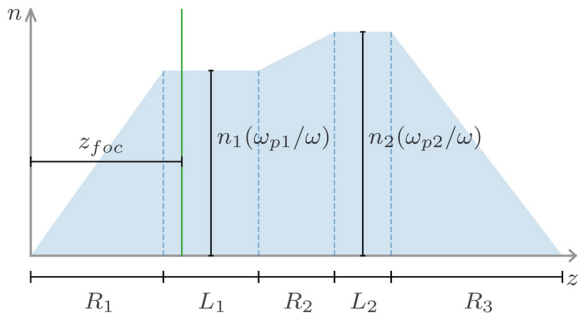

FIG. 11. Generalized two-plateau gas-density profile (case 3).

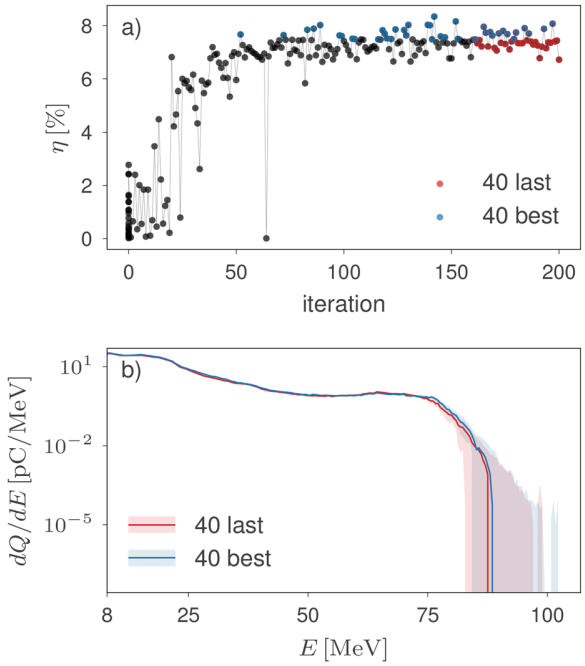

FIG. 12. (a) η along the optimization of case 3. Blue and red dots represent the 40 best and 40 last simulations, respectively. (b) Average energy spectra of the 40 best (blue line) and 40 last (red line) simulations, with shaded areas representing their 95% confidence intervals.

The laser and plasma dynamics for the optimal simulation of case 3 are depicted in Fig. 15. Figures 15(a)–15(c) illustrate the system along the first plateau (L_1). Compared to case 2, the laser self-modulates later due to the longer focal position in case 3 ($z_{foc} = 112\ \mu$m, as opposed to 58 μm in case 2). At the end of L_1, shown in panel (c), two continuous external contour lines ($a_0 = 1$ and $a_0 = 2$) still envelop four peaks exceeding $a_0 = 3$. Despite this, the plasma density shows well-formed bubbles, and a small fraction of backtracked electrons has already reached energies above 75 MeV. As depicted in panels (d) and (e), the self-modulation intensifies as the laser propagates along the up-ramp (R_2) and reaches the second plateau (L_2). During this process, the bubble structure of the plasma electrons is preserved, and a significant

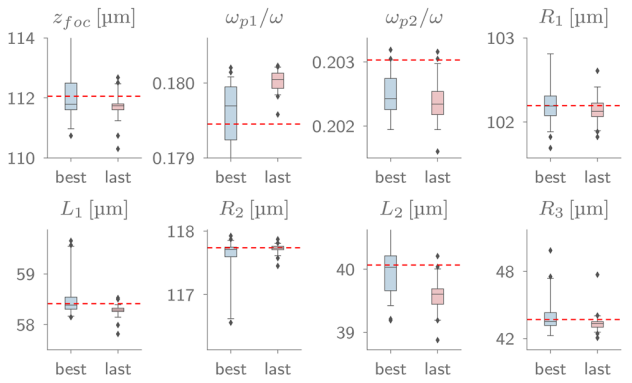

FIG. 13. Input parameter distributions for the 40 best (blue boxplots) and 40 last (light-red boxplots) simulations of case 3. The red dashed lines indicate the optimal values for each parameter.

injection of backtracked electrons is observed in this region. Moreover, because the wakefield amplitude scales with the increased density, a greater fraction of these electrons is accelerated to higher energies. At the end of the second plateau, as depicted in panel (f), the system resembles a laser wakefield accelerator (LWFA) operating in the nonlinear regime, with a train of short and intense laser fragments driving well-defined bubbles filled with high-energy electrons. Panel (g) shows that halfway down the final ramp (R_3), which is approximately 50% shorter than the corresponding ramp in case 2, the main laser fragments and the accelerating structure remain well-defined. As observed in the optimal simulations of previous cases, there is a seamless transition of accelerated electrons between bubbles as they expand and merge, facilitated due to the decreasing density. The final panel of Fig. 15, panel (h), depicts the accelerated beam after ejection from the plasma.

VI. COMPARISON OF THE THREE OPTIMIZED GAS-DENSITY PROFILES

Table VI presents the optimal input and output parameters for cases 1, 2, and 3, illustrating the differences across these scenarios. Case 1 exhibits the least favorable performance, with laser-to-beam conversion efficiency of 3.8%, a median selected energy $\tilde{E}_{sel}$ of 16.9 MeV, and a selected charge Q_{sel} of approximately 600 pC. In contrast, case 2, despite having a lower median energy, $\tilde{E}_{sel} = 14.6$ MeV, achieves a significantly higher efficiency, $\eta = 6.3\%$. This improvement is attributed to a substantial 67% increase in the charge, with $Q_{sel} \simeq 1000$ pC. Case 3 exhibits the best performance among the three cases, with $\eta = 8.3\%$. Although the median energy $\tilde{E}_{sel} = 16.7\ MeV$ in case 3 is higher than in case 2, it did not reach the 16.9 MeV attained in case 1. However, a 30% increase in the charge, $Q_{sel} \simeq 1300$ pC, ensured significant improvement of case 3 over case 2. Figure 16 corroborates the consistence of these findings by comparing the distributions of the objective function and the output parameters from the last 40 simulations of each case, with the optimal values marked by red dashed lines.

Figure 17(a) displays the gas-density profiles of the optimal gas configurations for the three cases. The shorter total length of case 1 contributes for its lower performance, as the electrons are accelerated over a shorter distance. Up to the end of the first plateau (L_1), the

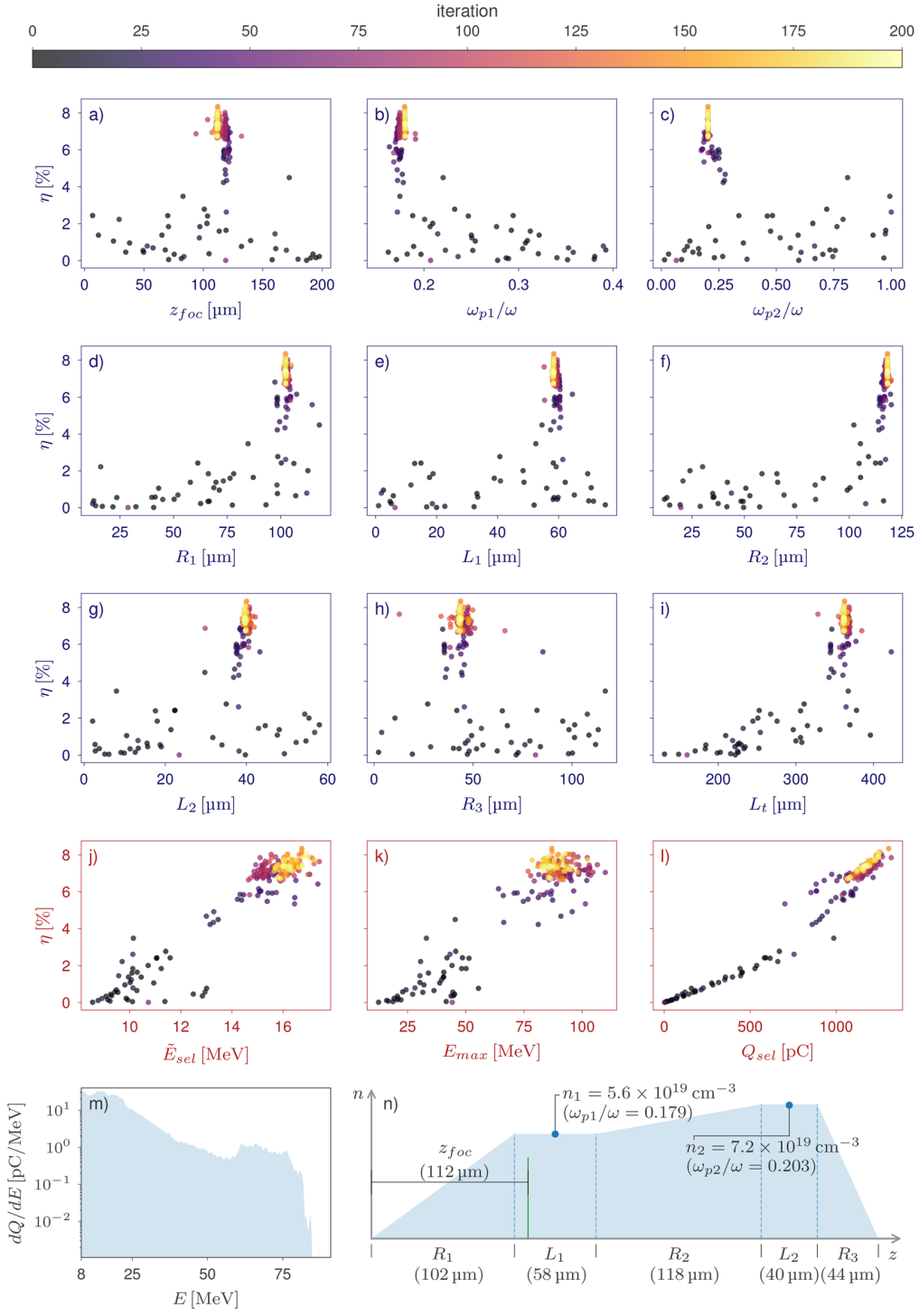

FIG. 14. Bayesian optimization of case 3, with a color scale indicating the algorithm iteration. Input parameters: η vs the (a) laser focal position, plasma-to-laser frequency ratio in the (b) first and (c) second plateaus, lengths of the (d) first ramp, (e) first plateau, (f) central ramp, (g) second plateau, (h) last ramp, and (i) total profile. Output parameters: η vs the (j) median energy (above 8 MeV) $\tilde{E}_{sel}$ (k) maximum energy, and (l) selected charge. Case 2 optimal: (m) energy spectrum and (n) gas-density profile, with optimal input parameters.

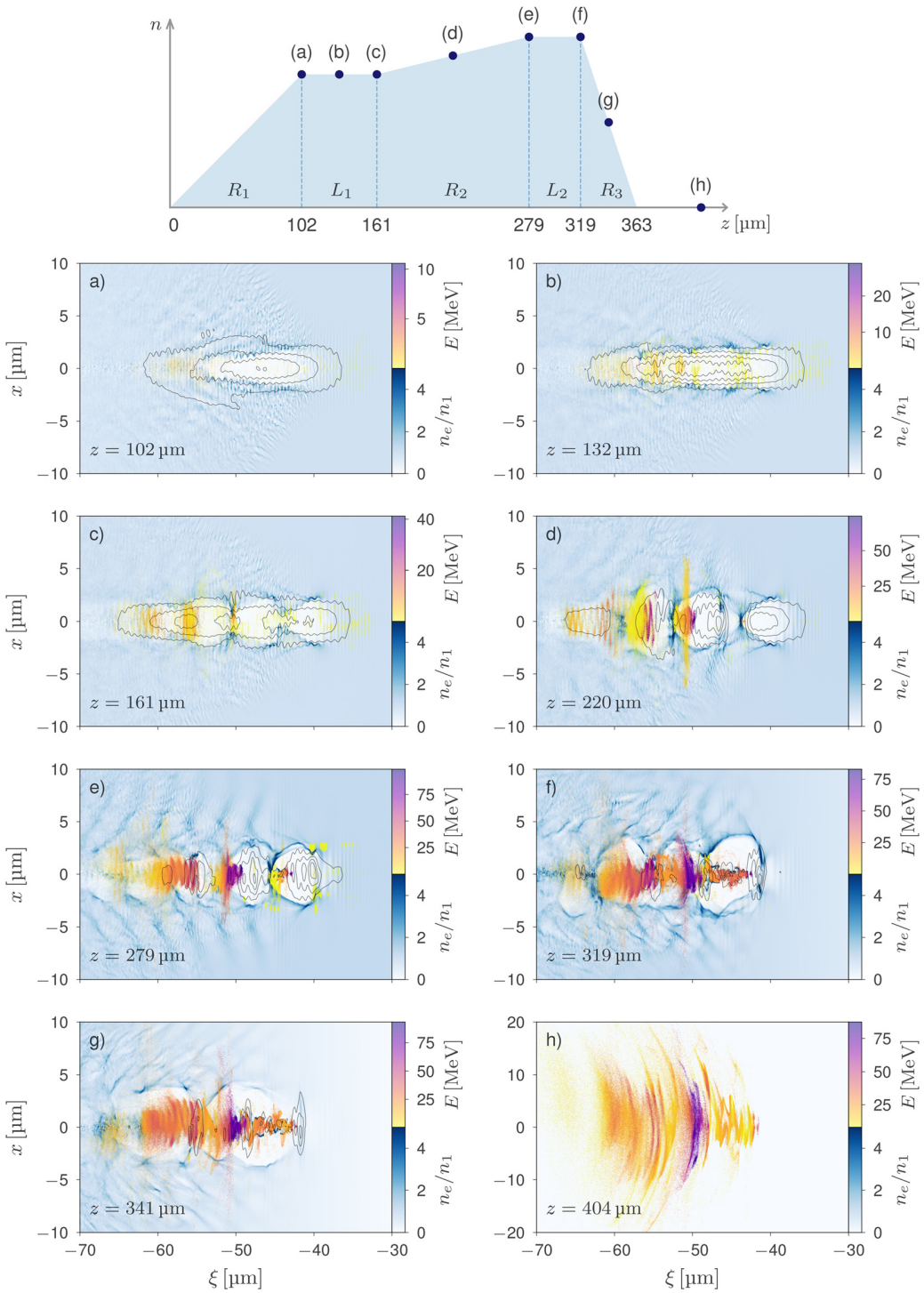

FIG. 15. Spatial evolution of the optimal simulation, case 3. The upper panel shows the propagation distances at which panels (a) to (h) were plotted. In these panels, the plasma electron density, normalized by the plateau density, is shown using a blue gradient scale. The backtracked electrons, which will attain energies exceeding 8 MeV after ejection, are depicted as colored dots with a yellow-purple color scale representing their energies at the current propagation distance. Additionally, contour lines for a_0 ranging from 1 (outermost) to 4 (innermost) were added to show the laser envelope at these distances.

TABLE VI. Optimal input and output parameters.

Parameter	Unit	Case 1	Case 2	Case 3
z_{foc}	μm	113.4	57.9	112.1
ω_{p1}/ω	⋯	0.210	0.216	0.179
ω_{p2}/ω	⋯	⋯	0.208	0.203
R_1	μm	99.8	94.2	102.3
L_1	μm	59.8	66.3	58.4
R_2	μm	62.1	100.5	118.2
L_2	μm	⋯	30.9	40.1
R_3	μm	⋯	94.1	43.7
η	%	3.8	6.3	8.3
$\tilde{E}_{sel}$	MeV	16.9	14.6	16.7
E_{max}	MeV	73	81	87
Q_{sel}	pC	601	999	1305

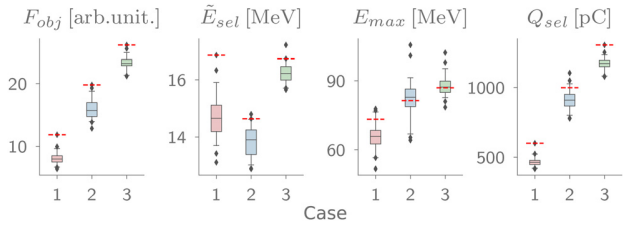

FIG. 16. Output parameter distributions from the 40 last simulations of cases 1, 2, and 3 (optimal values are marked with red dashed lines).

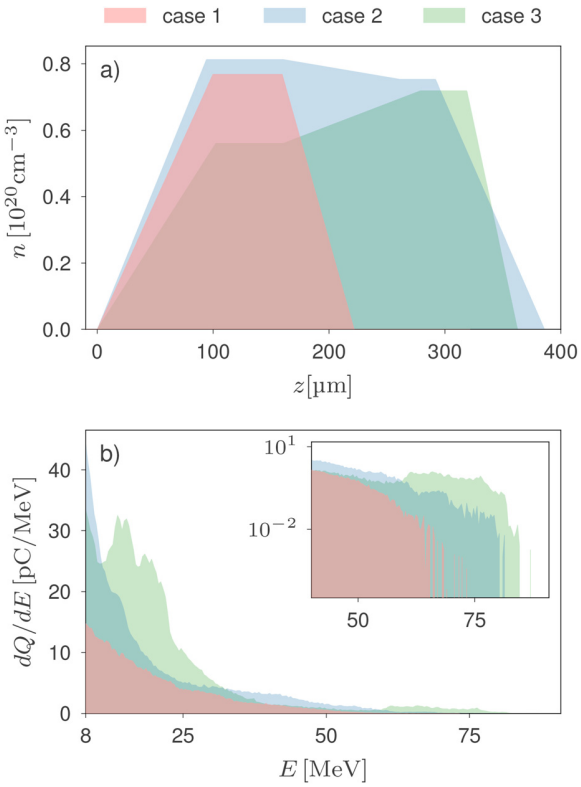

FIG. 17. Optimal (a) profiles and (b) energy spectra, with higher energies displayed in a log-scale inset.

profile in case 2, despite its higher density, is comparable to that of case 1. However, in case 2, L_1 is followed by a longer and less steep down-ramp (R_2) connecting the first plateau to a second one (L_2), which is shorter and has a slightly lower density. The profile then concludes with a final down-ramp (R_3), with length and declivity similar to those in case 1. In case 2, the addition of a second, lower-density plateau starting from the down-ramp aimed at increasing the acceleration length while maintaining the system configuration established along the down-ramp. Although this intended goal was not fully achieved, as evidenced by the lower median energy in case 2 compared to case 1, the proposed profile significantly enhanced the self-injection of plasma electrons. This enhancement was particularly effective in the down-ramps, where decreasing density allows the bubbles to elongate and capture more electrons at their rear. This mechanism, depicted in Fig. 10, was identified by the algorithm as the optimal strategy to maximize the objective function by increasing the beam charge. In case 3, the constraint of having the second plateau with a lower density than the first one was removed. This change allowed the algorithm to find a distinct optimal profile, with an up-ramp connecting a lower-density plateau to a higher-density one. This configuration produced a 30% increase in charge compared to the optimal result of case 2, and yielded a spectrum favorable for producing bremsstrahlung photons with energies capable of triggering the desired photoactivation reaction.

Figure 17(b) depicts the optimal energy spectra for the three cases. Case 3 clearly outperforms cases 1 and 2, deviating from the typical exponential decay commonly observed in electron beam spectra accelerated via SM-LWFA. The charge peak within the 8–25 MeV range in case 3 is particularly interesting, as it might increase the yield of photons with optimal energies for the ^{100}Mo(γ,n)^{99}Mo reaction, enhancing the production of ^{99}Mo. Additionally, the optimal spectrum of case 3 exhibits a distinct high-charge plateau at energies exceeding $\sim$ 50 MeV, as highlighted in the inset of Fig. 17. This can be attributed to the up-ramp placed after the wakefield and bubbles were established along the first plateau.[36]

To visualize how the ramps and plateaus affect the accelerated beams, Figs. 18(a)–18(c) display histograms of the propagation distances at which the backtracked electrons (comprising the accelerated beams) originated along the optimal profiles. These histograms are stratified and color-coded by energy ranges that cover the corresponding optimal spectra, displayed on the right side of each panel. Additionally, the fraction of charge contained within each energy range, denoted as Q/Q_{sel}, is also displayed. Figure 18(a) shows that, in case 1, the majority of electrons of the accelerated beam originated along the plateau L_1, with exceptions being a small fraction of high-energy particles from the up-ramp R_1, and a low-energy fraction from the down-ramp R_2. Additionally, the histograms indicate that backtracked electrons with higher energies originated from earlier positions of L_1, likely because they were accelerated over longer distances. In case 2, Fig. 18(b) shows that while most of the backtracked electrons originated along the first plateau L_1, an appreciable fraction also originated halfway down the ramp R_2, across most energy ranges.

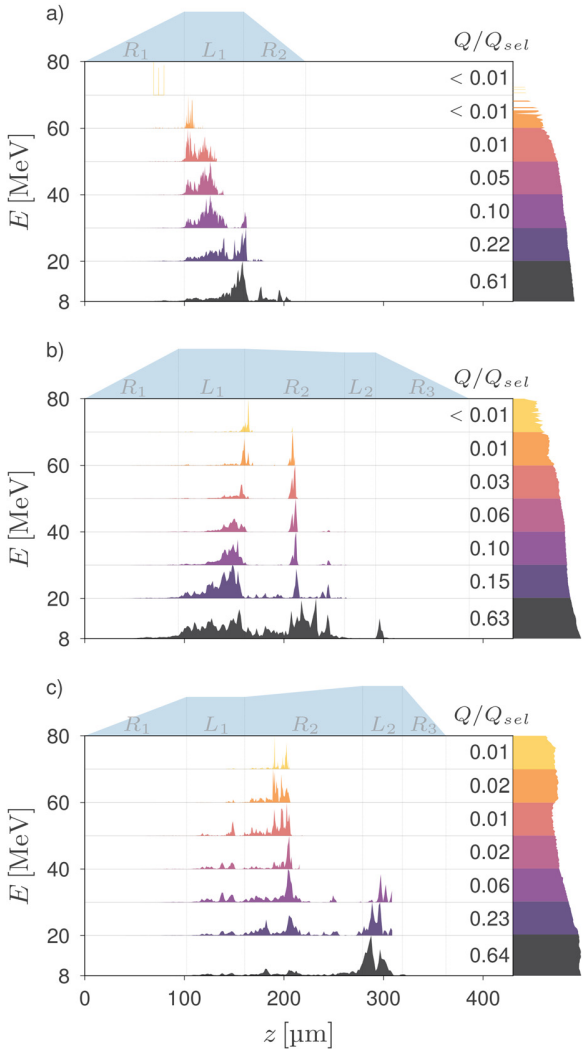

FIG. 18. Propagation distances at which the backtracked electrons (comprising the accelerated beams) originated along the optimal profiles: (a) case 1, (b) case 2, and (c) case 3.

Interestingly, in contrast to case 1, electrons originated from later positions in L_1 achieved higher energies in the accelerated beam. In case 3, Fig. 18(c) illustrates that, despite the contribution from the plateau L_1, the up-ramp R_2 plays a crucial role in forming the accelerated beam, contributing appreciable charge across all energy ranges. The second plateau L_2 also contributes a large fraction of the beam charge, mostly in the lower energy ranges. Since these ranges coincide with the maximum cross-Sec. for the ^{99}Mo(γ, n)^{100}Mo reaction, these particles may play a relevant role in the production of ^{99}Mo.

A. LWFA vs DLA

The observed results stem from a complex interplay between two accelerating mechanisms, LWFA and DLA, whose relative contributions are determined by the coupled laser-plasma dynamics and influenced by variations in the gas-density profile and laser self-modulation. The kinetic energy of an electron can be expressed as $E_k = m_e c^2(\gamma - 1)$, where $\gamma^2 = \Gamma_\parallel + \Gamma_\perp + 1$. In this expression, $\Gamma_\parallel$ is the normalized longitudinal energy gain of the electron, primarily driven by the wakefield in the LWFA process, and $\Gamma_\perp$ is the normalized transverse energy gain, attributed to the laser's transverse electric field (DLA). These energy gains can be quantified as follows:[57,58]

$$\Gamma_\parallel = \frac{-2e}{(mc)^2}\int_0^t \vec{E}_\parallel \cdot \vec{p}_\parallel dt' \ , \ \Gamma_\perp = \frac{-2e}{(mc)^2}\int_0^t \vec{E}_\perp \cdot \vec{p}_\perp dt'. \qquad (5)$$

Figure 19 presents the energy contributions of LWFA and DLA. For all three cases, the histories of γ^2, $\Gamma_\parallel$, and $\Gamma_\perp$ are displayed for high-energy electrons, with energies approximately evenly distributed

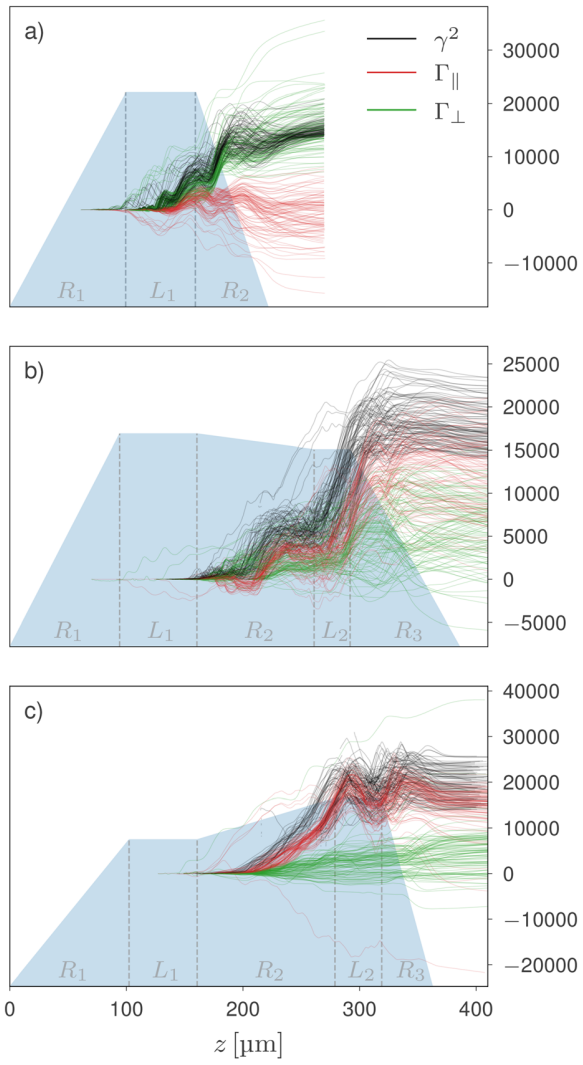

FIG. 19. LWFA and DLA energy gain comparison of the most energetic electrons in: (a) case 1, (b) case 2, and (c) case 3.

between 60 MeV and the maximum energy observed in each case. In case 1, depicted in Fig. 19(a), DLA dominates as the primary acceleration mechanism, whereas LWFA performs negative work on a significant fraction of high-energy particles, as evidenced by the large number of electrons with $\Gamma_{\parallel} < 0$. Figure 19(b) shows that, in case 2, both LWFA and DLA significantly contribute to the final energy of the selected electrons. LWFA's influence is particularly notable in two regions: the middle of R_2 ($206 \lesssim z \lesssim 236\,\mu$m) and from the center of L_2 to the beginning of R_3 ($270 \lesssim z \lesssim 315\,\mu$m), where particles experience substantial energy gain driven by $\Gamma_{\parallel}$. By the end of the target, LWFA's contribution slightly surpasses that of DLA. Nevertheless, both mechanisms play critical roles in acceleration, as reflected in the overlap of the red and green lines within the range $6000 \lesssim \Gamma_{\parallel}, \Gamma_{\perp} \lesssim 13\,000$. Figure 19(c) illustrates that, in case 3, LWFA is the dominant acceleration mechanism. From the middle of R_2 to the beginning of L_2, LWFA drives a sustained increase in particle energy. By the end of the process, LWFA contributes the majority of the final energy for the selected particles. However, DLA's contribution remains significant, as evidenced by the green lines showing that some particles achieve $\Gamma_{\perp} \approx 10\,000$.

B. Estimates of ^{99}Mo yields

To conclude the comparison, preliminary estimates for the production of ^{99}Mo were obtained for the three cases, using Monte Carlo simulations executed with the TOPAS[59,60] code. For each optimal beam, 10^8 electrons were randomly sampled from their FBPIC phase space, taking into account the macroparticle weights. These electrons were then used in TOPAS as the radiation source to irradiate a cylindrical target made of natural molybdenum, measuring 5 cm in length and 10 cm in radius, positioned 10 cm from the source in vacuum. The front face of the target features a 4.5 mm-thick layer of tantalum to convert the impinging electrons into photons through bremsstrahlung. The *g4em-standard_opt4* and *g4em-extra* physics lists were used, and an *OriginCount* volume scorer was set to count the ^{99}Mo yield within the target.

Table VII displays the number of ^{99}Mo isotopes (N) produced by a single shot from each optimal beam. Despite the qualitative variations in the optimal energy spectra shown in Fig. 17(b), Table VII reveals a strong scaling between the ^{99}Mo yield and the beam charge. This is evident from the normalized quantities N/N_1 and $Q/Q_{sel,1}$, with N_1 and $Q_{sel,1}$ representing case 1's ^{99}Mo yield and beam charge, respectively.

The administered activity of a given radiopharmaceutical depends on the intended medical procedure. For ^{99m}Tc, the daughter isotope of ^{99}Mo, a typical activity of 370 MBq per patient is often used, although US standards suggest doubling this to 740 MBq.[18,61] Given the longer half-life of ^{99}Mo (66 h) relative to ^{99m}Tc (6 h), the activity of the daughter isotope, though slightly lower, is similar to that of its parent. Hence, the ^{99}Mo activities illustrated in Fig. 20, derived from the yields listed in Table VII assuming an SM-LWFA operating at 1 kHz, can also be used as estimates for those of ^{99m}Tc. From Fig. 20, after 7 days of irradiation, case 1 barely surpasses 370 MBq, while case 2 reaches the 740 MBq threshold. Case 3 shows the best performance, exceeding this threshold in approximately 4.5 days. Although these results are not yet practical for clinical applications, they represent a significant improvement over those reported in a previous computational study using LWFA-accelerated electrons.[18] Moreover, employing multiple laser systems could substantially reduce the irradiation time. For instance, working with five laser systems in parallel and using case 3 optimal parameters, the 740 MBq threshold could be reached in approximately 13.7 h of irradiation.

TABLE VII. Number of ^{99}Mo isotopes (including the standard deviation) produced by a single shot of each optimal beam.

Case	Q_{sel} (pC)	$N \times 10^6$ (atoms of ^{99}Mo)	$Q_{sel}/Q_{sel,1}$	N/N_1
1	601	0.513 ($\pm$0.004)	1	1
2	999	0.911 ($\pm$0.008)	1.66	1.78
3	1305	1.103 ($\pm$0.009)	2.17	2.15

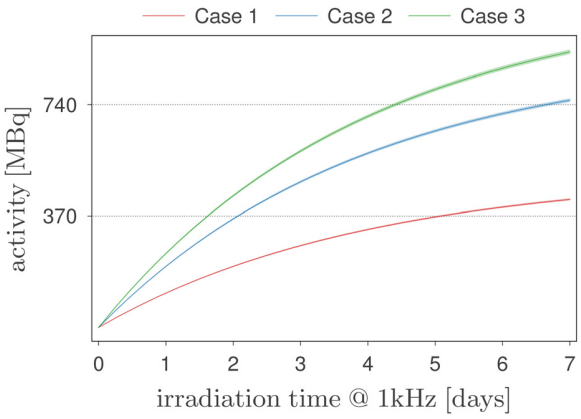

FIG. 20. ^{99}Mo activity as a function of irradiation time, assuming a repetition rate of 1 kHz.

VII. CONCLUSIONS AND DISCUSSION

In this work, Bayesian optimization was applied to PIC simulations to maximize the sum of charge-weighted energies of electron beams accelerated via SM-LWFA, which is equivalent to maximizing the laser-to-beam energy conversion efficiency. Optimization of three distinct profiles resulted in electron beams with median energies ranging from 14 to 17 MeV and charges between 600 and 1300 pC. The optimized profiles achieved laser-to-beam conversion efficiencies of 3.8%, 6.3%, and 8.3% when considering electrons with energies above 8 MeV. Without this threshold, the efficiencies increased to 5.0%, 10.6%, and 11.6% for profiles 1, 2, and 3, respectively. While in the bubble regime there are multiple reports of laser-to-beam efficiencies ranging from 8.2% to 12.4%,[54,62,63] less information is available on the efficiency of SM-LWFA. By estimating the efficiency for this regime from a previous work of our group,[12] a value of 0.11% for particles with energies above 4 MeV was obtained. Compared to this, results from this work show a significant improvement, achieving for the SM-LWFA efficiency levels comparable to those typically reported for the bubble regime.

The optimal beams can generate bremsstrahlung photons capable of producing ^{99}Mo through the ^{99}Mo(γ, n)^{100}Mo reaction route in a tantalum-molybdenum target. Monte Carlo simulations estimated preliminary ^{99}Mo yields for each configuration, enabling calculation of irradiation times to achieve activity levels of 370 and 740 MBq,

comparable to the clinical activity of its daughter isotope, ^{99m}Tc, used in medical procedures.

For the optimal gas-density profiles, the laser-plasma dynamics along the ramps and plateaus was presented and discussed. Additionally, electrons comprising the final accelerated beams were backtracked to assess their energy gains throughout propagation. Energy-binned histograms were plotted for the propagation distances at which the backtracked electrons were trapped/injected, providing insights into how the ramps and plateaus influence the final energy and charge distributions in the accelerated beams. In the self-modulated regime, both acceleration mechanisms, LWFA and DLA, coexists. As the laser pulse undergoes self-focusing and self-modulation, the formation of short, intense laser fragments occurs. These fragments are capable of driving bubbles similar to those observed in the nonlinear regime of LWFA. However, due to the presence of multiple fragments, DLA is caused by the overlap of these fragments with the electrons undergoing LWFA acceleration within the bubbles.

Tailored profiles have been investigated for various applications, including plasma beam dumps[64] and proton-driven wakefield acceleration in Project AWAKE.[6] Although experimentally challenging, the implementation of such profiles might be feasible using de Laval nozzles or one-sided shock nozzles[13] to generate appropriate gas jets. Alternatively, when using capillaries, temperature gradients can create density ramps, while Secs. held at constant temperatures can form plateaus of varying densities. This method was successfully applied to tailor the 10-m-long rubidium plasma in Project AWAKE.[65] Additionally, while the presented simulations utilized only hydrogen, future computational studies will explore and optimize gas mixtures, such as hydrogen with nitrogen, to further enhance the energy and charge of electron beams produced by laser wakefield accelerators operating in the self-modulated regime.

While Bayesian optimization effectively maximized electron beam charge and energy, this strategy may not be ideal for ^{99}Mo photoactivation. The chosen objective function, prioritizing high-energy particles (charge $\times$ energy), yielded spectra exceeding 70 MeV. Though these electrons can generate suitable photons (8–20 MeV) for ^{99}Mo photoactivation, they can also produce higher-energy photons, capable of inducing unwanted photonuclear reactions, leading to neutron and secondary particle emissions.[66] This risk must be assessed before using beams with high-energy electrons for isotope production via photoactivation.

The ^{99}Mo yields presented in this work are preliminary, non-optimal results, intended primarily to provide an expected order of magnitude and to allow for relative comparisons between the cases presented. In a previous study,[67] TOPAS demonstrated mixed performance in modeling radioisotope production compared to GEANT4.[68] Key issues include limitations in physics lists, especially at lower energies for light target nuclei, and high sensitivity to the target geometry and placement. Hence, further investigation is required to attain more reliable results. While the current ^{99}Mo yields fall short of clinical practicality, they represent a significant advancement over a prior SM-LWFA-based approach.[18] Furthermore, multiple high-repetition-rate, few-terawatt laser systems could be employed in parallel for achieving clinically relevant activities (370–740 MBq for ^{99}Mo's daughter isotope, ^{99m}Tc) within a few hours.

By incorporating a finite number of azimuthal modes, quasi-cylindrical pseudo-spectral PIC codes capture essential dynamics while accommodating moderate asymmetries, achieving a balance between accuracy and reduced computational costs compared to fully 3D simulations. However, truncating higher-order modes limits their ability to resolve complex asymmetries and fine-scale 3D effects. This study employed three azimuthal modes, a configuration recommended in FBPIC documentation for modeling nonlinear processes like electron self-injection. This setup may also effectively model the nonlinear dynamics of laser pulses in self-modulated LWFA with tailored plasma density profiles. However, due to the lack of detailed comparisons with full 3D simulations under these conditions, the results should be interpreted carefully. Cartesian 3D simulations may still be required for highly asymmetric setups or to ensure fidelity in capturing complex transverse dynamics.

Finally, the laser parameters adopted in this work are optimistic, as no currently available systems, to our knowledge, can deliver pulse energies in the range of hundreds of mJ at kHz repetition rates, as adopted in this work. EKSPLA[69] offers an 8 fs, 5 TW laser operating at 1 kHz, delivering 42.6 mJ per pulse. Similarly, Amplitude[70] provides a 20 fs, 1 TW laser capable of delivering 20 mJ per pulse at the same repetition rate. With ongoing advancements in laser technology, systems with parameters comparable to those used in this study are expected to become available in the near future.

ACKNOWLEDGMENTS

The authors acknowledge computing resources provided by LNCC's SDumont HPC system (project LPA-FARMA) and the N8 Centre of Excellence in Computationally Intensive Research (N8 CIR), provided and funded by the N8 research partnership and EPSRC (Grant No. EP/T022167/1). This study was financed in part by the Conselho Nacional de Desenvolvimento Cientifico e Tecnológico (CNPq, Grant Nos. 405143/2021-4 and 140941/2023-1), the Fundação de Amparo à Pesquisa do Estado do Rio Grande do Sul (FAPERGS, Grant Nos. 21/2551-0002027-0 and 24/2551-0001552-3), and the Coordenação de Aperfeiçoamento de Pessoal de Nível Superior, Brasil (CAPES, Grant No. 88887.620985/2021-00). Javier Resta López is supported by the Generalitat Valenciana, Spain, under grant agreement CIDEGENT/2019/058.

AUTHOR DECLARATIONS

Conflict of Interest

The authors have no conflicts to disclose.

Author Contributions

B. S. Nunes: Conceptualization (equal); Data curation (equal); Formal analysis (equal); Investigation (equal); Methodology (equal); Resources (lead); Software (equal); Validation (equal); Visualization (equal); Writing – original draft (equal); Writing – review & editing (equal). **A. Bonatto:** Conceptualization (lead); Data curation (equal); Formal analysis (equal); Funding acquisition (equal); Investigation (equal); Methodology (equal); Project administration (lead); Resources (lead); Software (equal); Supervision (equal); Validation (equal); Visualization (equal); Writing – original draft (equal); Writing – review & editing (equal). **S. P. Santos:** Writing – review & editing (equal). **R. P. Nunes:** Software (equal); Writing – review & editing (equal). **C. Bonțoiu:** Writing – review & editing (equal). **M. S. Alva-Sánchez:**

Funding acquisition (equal); Project administration (equal); Supervision (equal); Writing – review & editing (equal). **R. E. Samad:** Conceptualization (equal); Funding acquisition (equal); Writing – review & editing (equal). **N. D. Vieira, Jr.,:** Conceptualization (equal); Funding acquisition (equal); Writing – review & editing (equal). **G. Xia:** Writing – original draft (equal). **J. Resta-Lopez:** Funding acquisition (equal); Writing – review & editing (equal).

DATA AVAILABILITY

The data that support the findings of this study are available from the corresponding authors upon reasonable request.

REFERENCES

[1]E. Esarey, C. B. Schroeder, and W. P. Leemans, "Physics of laser-driven plasma-based electron accelerators," Rev. Mod. Phys. **81**, 1229–1285 (2009).

[2]T. Tajima and J. M. Dawson, "Laser electron accelerator," Phys. Rev. Lett. **43**, 267–270 (1979).

[3]P. Chen, J. J. Su, J. M. Dawson, K. L. Bane, and P. B. Wilson, "On energy transfer in the plasma wake field accelerator," Phys. Rev. Lett. **56**, 1252–1255 (1986).

[4]I. Blumenfeld, C. E. Clayton, F. J. Decker, M. J. Hogan, C. Huang, R. Ischebeck, R. Iverson, C. Joshi, T. Katsouleas, and N. Kirby, "Energy doubling of 42 GeV electrons in a metre-scale plasma wakefield accelerator," Nature **445**, 741–744 (2007).

[5]R. D'Arcy, A. Aschikhin, S. Bohlen, G. Boyle, T. Brümmer, J. Chappell, S. Diederichs, B. Foster, M. J. Garland, L. Goldberg, P. Gonzalez, S. Karstensen, A. Knetsch, P. Kuang, V. Libov, K. Ludwig, A. M. de la Ossa, F. Marutzky, M. Meisel, T. J. Mehrling, P. Niknejadi, K. Pöder, P. Pourmoussavi, M. Quast, J. H. Röckemann, L. Schaper, B. Schmidt, S. Schröder, J. P. Schwinkendorf, B. Sheeran, G. Tauscher, S. Wesch, M. Wing, P. Winkler, M. Zeng, and J. Osterhoff, "FLASHForward: Plasma wakefield accelerator science for high-average-power applications," Philos. Trans. R Soc. A **377**, 20180392 (2019).

[6]E. Adli, A. Ahuja, O. Apsimon, R. Apsimon, A.-M. Bachmann, D. Barrientos, F. Batsch, J. Bauche, V. K. B. Olsen, M. Bernardini, T. Bohl, C. Bracco, F. Braunmüller, G. Burt, B. Buttenschön, A. Caldwell, M. Cascella, J. Chappell, E. Chevallay, M. Chung, D. Cooke, H. Damerau, L. Deacon, L. H. Deubner, A. Dexter, S. Doebert, J. Farmer, V. N. Fedosseev, R. Fiorito, R. A. Fonseca, F. Friebel, L. Garolfi, S. Gessner, I. Gorgisyan, A. A. Gorn, E. Granados, O. Grulke, E. Gschwendtner, J. Hansen, A. Helm, J. R. Henderson, M. Hüther, M. Ibison, L. Jensen, S. Jolly, F. Keeble, S.-Y. Kim, F. Kraus, Y. Li, S. Liu, N. Lopes, K. V. Lotov, L. M. Brun, M. Martyanov, S. Mazzoni, D. M. Godoy, V. A. Minakov, J. Mitchell, J. C. Molendijk, J. T. Moody, M. Moreira, P. Muggli, E. Öz, C. Pasquino, A. Pardons, F. P. Asmus, K. Pepitone, A. Perera, A. Petrenko, S. Pitman, A. Pukhov, S. Rey, K. Rieger, H. Ruhl, J. S. Schmidt, I. A. Shalimova, P. Sherwood, L. O. Silva, L. Soby, A. P. Sosedkin, R. Speroni, R. I. Spitsyn, P. V. Tuev, M. Turner, F. Velotti, L. Verra, V. A. Verzilov, J. Vieira, C. P. Welsch, B. Williamson, M. Wing, B. Woolley, and G. Xia, "Acceleration of electrons in the plasma wakefield of a proton bunch," Nature **561**, 363–367 (2018).

[7]E. Gschwendtner, K. Lotov, P. Muggli, M. Wing, R. Agnello, C. C. Ahdida, M. C. A. Goncalves, Y. Andrebe, O. Apsimon, R. Apsimon, J. M. Arnesano, A.-M. Bachmann, D. Barrientos, F. Batsch, V. Bencini, M. Bergamaschi, P. Blanchard, P. N. Burrows, B. Buttenschön, A. Caldwell, J. Chappell, E. Chevallay, M. Chung, D. A. Cooke, H. Damerau, C. Davut, G. Demeter, A. C. Dexter, S. Doebert, F. A. Elverson, J. Farmer, A. Fasoli, V. Fedosseev, R. Fonseca, I. Furno, S. Gessner, A. Gorn, E. Granados, M. Granetzny, T. Graubner, O. Grulke, E. D. Guran, V. Hafych, A. Hartin, J. Henderson, M. Hüther, M. Kedves, F. Keeble, V. Khudiakov, S.-Y. Kim, F. Kraus, M. Krupa, T. Lefevre, L. Liang, S. Liu, N. Lopes, M. M. Calderon, S. Mazzoni, D. M. Godoy, J. Moody, K. Moon, P. I. M. Guzmán, M. Moreira, T. Nechaeva, E. Nowak, C. Pakuza, H. Panuganti, A. Pardons, K. Pepitone, A. Perera, J. Pucek, A. Pukhov, R. L. Ramjiawan, S. Rey, A. Scaachi, O. Schmitz, E. Senes, F. Silva, L. Silva, C. Stollberg, A. Sublet, C. Swain, A. Topaloudis, N. Torrado, P. Tuev, M. Turner, F. Velotti, L. Verra, V. Verzilov, J. Vieira, H. Vincke, M. Weidl, C. Welsch, M. Wendt, P. Wiwattananon, J. Wolfenden, B. Woolley, S. Wyler, G. Xia, V. Yarygova, M. Zepp, and G. Z. D. Porta, "The AWAKE run 2 programme and beyond," Symmetry **14**, 1680 (2022).

[8]A. Gonsalves, K. Nakamura, J. Daniels, C. Benedetti, C. Pieronek, T. de Raadt, S. Steinke, J. Bin, S. Bulanov, J. van Tilborg, C. Geddes, C. Schroeder, C. Tóth, E. Esarey, K. Swanson, L. Fan-Chiang, G. Bagdasarov, N. Bobrova, V. Gasilov, G. Korn, P. Sasorov, and W. Leemans, "Petawatt laser guiding and electron beam acceleration to 8 GeV in a laser-heated capillary discharge waveguide," Phys. Rev. Lett. **122**, 084801 (2019).

[9]N. E. Andreev, L. M. Gorbunov, V. I. Kirsanov, A. A. Pogasova, and R. R. Ramazashvili, "Resonant excitation of wakefields by a laser pulse in a plasma," JETP Lett. **55**, 551 (1992). See http://jetpletters.ru/ps/0/article_19308.shtml.

[10]J. Krall, A. Ting, E. Esarey, and P. Sprangle, "Enhanced acceleration in a self-modulated-laser wake-field accelerator," Phys. Rev. E **48**, 2157–2161 (1993).

[11]D. L. Fisher and T. Tajima, "Enhanced raman forward scattering," Phys. Rev. E **53**, 1844–1851 (1996).

[12]E. P. Maldonado, R. E. Samad, A. Bonatto, R. P. Nunes, S. Banerjee, and N. D. Vieira, "Study of quasimonoenergetic electron bunch generation in self-modulated laser wakefield acceleration using TW or sub-TW ultrashort laser pulses," AIP Adv. **11**, 065116 (2021).

[13]L. Rovige, J. Huijts, I. Andriyash, A. Vernier, V. Tomkus, V. Girdauskas, G. Raciukaitis, J. Dudutis, V. Stankevic, P. Gecys, M. Ouille, Z. Cheng, R. Lopez-Martens, and J. Faure, "Demonstration of stable long-term operation of a kilohertz laser-plasma accelerator," Phys. Rev. Accel. Beams **23**, 093401 (2020).

[14]L. Rovige, J. Huijts, I. A. Andriyash, A. Vernier, M. Ouillé, Z. Cheng, T. Asai, Y. Fukuda, V. Tomkus, V. Girdauskas, G. Raciukaitis, J. Dudutis, V. Stankevic, P. Gecys, R. Lopez-Martens, and J. Faure, "Optimization and stabilization of a kilohertz laser-plasma accelerator," Phys. Plasmas **28**, 033105 (2021).

[15]B. S. Nunes, E. R. F. Rodrigues, J. A. P. Fruscalso, R. P. Nunes, A. Bonatto, and M. S. Alva-Sánchez, "Highly enriched uranium-free medical radioisotope production methods: An integrative review," Appl. Sci. **12**, 12569 (2022).

[16]S. Chemerisov, P. Tkac, C. Jonah, B. Micklich, V. Makarashvili, G. Vandegrift, G. Dale, K. Woloshun, M. Holloway, F. Romero, D. Dalmas, and J. Harvey, "Development activities in support of accelerator production of ^{99}Mo production through the γ,n reaction on ^{100}Mo," Trans. Am. Nucl. Soc. **107**, 68–71 (2012).

[17]F. T. Tárkányi, A. V. Ignatyuk, A. Hermanne, R. Capote, B. V. Carlson, J. W. Engle, M. A. Kellett, T. Kibedi, G. N. Kim, F. G. Kondev, M. Hussain, O. Lebeda, A. Luca, Y. Nagai, H. Naik, A. L. Nichols, F. M. Nortier, S. V. Suryanarayana, S. Takács, and M. Verpelli, "Recommended nuclear data for medical radioisotope production: Diagnostic gamma emitters," J. Radioanal. Nucl. Chem. **319**, 487–531 (2019).

[18]N. D. Vieira, E. P. Maldonado, A. Bonatto, R. P. Nunes, S. Banerjee, F. A. Genezini, M. Moralles, A. V. F. Zuffi, and R. E. Samad, "Laser wakefield electron accelerator: Possible use for radioisotope production," in *2021 SBFoton International Optics and Photonics Conference (SBFoton IOPC)* (IEEE, 2021).

[19]C. Birdsall and A. Langdon, *Plasma Physics via Computer Simulation* (Adam Hilger, 1991).

[20]E. Brochu, V. M. Cora, and N. de Freitas, "A tutorial on Bayesian optimization of expensive cost functions, with application to active user ayesian and hierarchical reinforcement learning," arXiv:1012.2599 (2010).

[21]A. Döpp, C. Eberle, S. Howard, F. Irshad, J. Lin, and M. Streeter, "Data-driven science and machine learning methods in laser–plasma physics," High Power Laser Sci. Eng. **11**, e55 (2023).

[22]R. J. Shalloo, S. J. D. Dann, J.-N. Gruse, C. I. D. Underwood, A. F. Antoine, C. Arran, M. Backhouse, C. D. Baird, M. D. Balcazar, N. Bourgeois, J. A. Cardarelli, P. Hatfield, J. Kang, K. Krushelnick, S. P. D. Mangles, C. D. Murphy, N. Lu, J. Osterhoff, K. Põder, P. P. Rajeev, C. P. Ridgers, S. Rozario, M. P. Selwood, A. J. Shahani, D. R. Symes, A. G. R. Thomas, C. Thornton, Z. Najmudin, and M. J. V. Streeter, "Automation and control of laser wakefield accelerators using Bayesian optimization," Nat. Commun. **11**, 6355 (2020).

[23]S. Jalas, M. Kirchen, P. Messner, P. Winkler, L. Hübner, J. Dirkwinkel, M. Schnepp, R. Lehe, and A. R. Maier, "Bayesian optimization of a laser-plasma accelerator," Phys. Rev. Lett. **126**, 104801 (2021).

[24]F. Irshad, S. Karsch, and A. Döpp, "Multi-objective and multi-fidelity Bayesian optimization of laser-plasma acceleration," Phys. Rev. Res. **5**, 013063 (2023).

[25]A. Ferran Pousa, S. Jalas, M. Kirchen, A. Martinez de la Ossa, M. Thévenet, S. Hudson, J. Larson, A. Huebl, J.-L. Vay, and R. Lehe, "Bayesian optimization of

laser-plasma accelerators assisted by reduced physical models," Phys. Rev. Accel. Beams **26**, 084601 (2023).
[26]A. Pukhov, Z.-M. Sheng, and J. M. ter Vehn, "Particle acceleration in relativistic laser channels," Phys. Plasmas **6**, 2847–2854 (1999).
[27]J. L. Shaw, N. Lemos, K. A. Marsh, F. S. Tsung, W. B. Mori, and C. Joshi, "Estimation of direct laser acceleration in laser wakefield accelerators using particle-in-cell simulations," Plasma Phys. Control. Fusion **58**, 034008 (2016).
[28]T. Wang, V. Khudik, A. Arefiev, and G. Shvets, "Direct laser acceleration of electrons in the plasma bubble by tightly focused laser pulses," Phys. Plasmas **26**, 083101 (2019).
[29]K. Schmid and L. Veisz, "Supersonic gas jets for laser-plasma experiments," Rev. Sci. Instrum. **83**, 053304 (2012).
[30]Z.-H. He, A. G. R. Thomas, B. Beaurepaire, J. A. Nees, B. Hou, V. Malka, K. Krushelnick, and J. Faure, "Electron diffraction using ultrafast electron bunches from a laser-wakefield accelerator at kHz repetition rate," Appl. Phys. Lett. **102**, 064104 (2013).
[31]J. Couperus, A. Köhler, T. Wolterink, A. Jochmann, O. Zarini, H. Bastiaens, K. Boller, A. Irman, and U. Schramm, "Tomographic characterisation of gas-jet targets for laser wakefield acceleration," Nucl. Instrum. Methods Phys. Res. A **830**, 504–509 (2016).
[32]B. B. Chiomento, A. V. F. Zuffi, N. D. V. Junior, F. B. D. Tabacow, E. P. Maldonado, and R. E. Samad, "Development of dielectric de laval nozzles for laser electron acceleration by ultrashort pulses micromachining," in *2021 SBFoton International Optics and Photonics Conference (SBFoton IOPC)* (IEEE, 2021).
[33]Z. Lei, Z. Jin, A. Zhidkov, N. Pathak, Y. Mizuta, K. Huang, N. Nakanii, I. Daito, M. Kando, and T. Hosokai, "Controllable electron self-injection in laser wakefield acceleration with asymmetric gas-jet nozzle," Prog. Theor. Exp. Phys. **2023**, 033J01.
[34]Z. Lei, Z. Jin, Y.-J. Gu, S. Sato, A. Zhidkov, A. Rondepierre, K. Huang, N. Nakanii, I. Daito, M. Kando, and T. Hosokai, "Modular supersonic nozzle for the stable laser-driven electron acceleration," Rev. Sci. Instrum. **95**, 015111 (2024).
[35]V. Tomkus, M. Mackevičiūtė, J. Dudutis, V. Girdauskas, M. Abedi-Varaki, P. Gečys, and G. Račiukaitis, "Laser-machined two-stage nozzle optimised for laser wakefield acceleration," J. Plasma Phys. **90**, 965900102 (2024).
[36]C. Aniculaesei, V. B. Pathak, H. T. Kim, K. H. Oh, B. J. Yoo, E. Brunetti, Y. H. Jang, C. I. Hojbota, J. H. Shin, J. H. Jeon, S. Cho, M. H. Cho, J. H. Sung, S. K. Lee, B. M. Hegelich, and C. H. Nam, "Electron energy increase in a laser wakefield accelerator using up-ramp plasma density profiles," Sci. Rep. **9**, 11249 (2019).
[37]Q. Yu, Y. J. Gu, X. F. Li, S. Huang, Q. Kong, and S. Kawata, "Electron self-injection into the phase of a wake excited by a driver laser in a nonuniform density target," Phys. Plasmas **22**, 073107 (2015).
[38]Z. Zhang, J. Liu, W. Wang, W. Li, C. Yu, Y. Tian, R. Qi, C. Wang, Z. Qin, M. Fang, J. Liu, K. Nakajima, R. Li, and Z. Xu, "Generation of high quality electron beams from a quasi-phase-stable cascaded laser wakefield accelerator with density-tailored plasma segments," New J. Phys. **17**, 103011 (2015).
[39]K. Swanson, H.-E. Tsai, S. Barber, R. Lehe, H.-S. Mao, S. Steinke, J. van Tilborg, K. Nakamura, C. Geddes, C. Schroeder, E. Esarey, and W. Leemans, "Control of tunable, monoenergetic laser-plasma-accelerated electron beams using a shock-induced density downramp injector," Phys. Rev. Accel. Beams **20**, 051301 (2017).
[40]G. Fubiani, E. Esarey, C. B. Schroeder, and W. P. Leemans, "Improvement of electron beam quality in optical injection schemes using negative plasma density gradients," Phys. Rev. E **73**, 026402 (2006).
[41]C. Benedetti, F. Rossi, C. B. Schroeder, E. Esarey, and W. P. Leemans, "Pulse evolution and plasma-wave phase velocity in channel-guided laser-plasma accelerators," Phys. Rev. E **92**, 023109 (2015).
[42]R. Lehe, M. Kirchen, I. A. Andriyash, B. B. Godfrey, and J.-L. Vay, "A spectral, quasi-cylindrical and dispersion-free particle-in-cell algorithm," Comput. Phys. Commun. **203**, 66–82 (2016).
[43]B. B. Godfrey, "Numerical Cherenkov instabilities in electromagnetic particle codes," J. Comput. Phys. **15**, 504–521 (1974).
[44]A. Huebl, R. Lehe, J.-L. Vay, D. P. Grote, I. Sbalzarini, S. Kuschel, D. Sagan, F. Pérez, F. Koller, and M. Bussmann, "Openpmd 1.1.0: Base paths for mesh- and particle-only files and updated attributes" (2018).
[45]M. V. Ammosov, N. B. Delone, and V. P. Krainov, "Tunnel ionization of complex atoms and atomic ions in electromagnetic field," in *SPIE Proceedings*, edited by J. A. Alcock (SPIE, 1986).
[46]F. Salehi, A. J. Goers, G. A. Hine, L. Feder, D. Kuk, B. Miao, D. Woodbury, K. Y. Kim, and H. M. Milchberg, "MeV electron acceleration at 1 kHz with $<$ mJ laser pulses," Opt. Lett. **42**, 215–218 (2017).
[47]A. Goers, G. Hine, L. Feder, B. Miao, F. Salehi, J. Wahlstrand, and H. Milchberg, "Multi-MeV electron acceleration by subterawatt laser pulses," Phys. Rev. Lett. **115**, 194802 (2015).
[48]D. Woodbury, L. Feder, V. Shumakova, C. Gollner, R. Schwartz, B. Miao, F. Salehi, A. Korolov, A. Pugžlys, A. Baltuška, and H. M. Milchberg, "Laser wakefield acceleration with mid-IR laser pulses," Opt. Lett. **43**, 1131 (2018).
[49]A. Bonatto, E. Maldonado, R. Nunes, R. Samad, F. Tabacow, N. Vieira, and A. Zuffi, "On the development of a low peak-power, high repetition-rate laser plasma accelerator at IPEN," in Proceedings of the 12th International Particle Accelerator Conference IPAC2021, Brazil (2021).
[50]M. Balandat, B. Karrer, D. R. Jiang, S. Daulton, B. Letham, A. G. Wilson, and E. Bakshy, "BoTorch: programmable Bayesian optimization in PyTorch," CoRR abs/1910.06403 (2019).
[51]C. E. Rasmussen and C. K. I. Williams, *Gaussian Processes for Machine Learning* (MIT Press, 2008).
[52]N. Srinivas, A. Krause, S. M. Kakade, and M. W. Seeger, "Information-theoretic regret bounds for Gaussian process optimization in the bandit setting," IEEE Trans. Inf. Theory **58**, 3250–3265 (2012).
[53]M. J. V. Streeter, Y. Ma, B. Kettle, S. J. D. Dann, E. Gerstmayr, F. Albert, N. Bourgeois, S. Cipiccia, J. M. Cole, I. Gallardo González, A. E. Hussein, D. A. Jaroszynski, K. Falk, K. Krushelnick, N. Lemos, N. C. Lopes, C. Lumsdon, O. Lundh, S. P. D. Mangles, Z. Najmudin, P. P. Rajeev, R. Sandberg, M. Shahzad, M. Smid, R. Spesyvtsev, D. R. Symes, G. Vieux, and A. G. R. Thomas, "Characterization of laser wakefield acceleration efficiency with octave spanning near-IR spectrum measurements," Phys. Rev. Accel. Beams **25**, 101302 (2022).
[54]F. Irshad, C. Eberle, F. M. Foerster, K. v Grafenstein, F. Haberstroh, E. Travac, N. Weisse, S. Karsch, and A. Döpp, "Pareto optimization and tuning of a laser wakefield accelerator," Phys. Rev. Lett. **133**, 085001 (2024).
[55]A. Sundström, I. Pusztai, P. Eng-Johnsson, and T. Fülöp, "Attosecond dispersion as a diagnostics tool for solid-density laser-generated plasmas," arXiv:2202.00406 (2022).
[56]S. Kiselev, A. Pukhov, and I. Kostyukov, "X-ray generation in strongly nonlinear plasma waves," Phys. Rev. Lett. **93**, 135004 (2004).
[57]C. Gahn, G. D. Tsakiris, A. Pukhov, J. Meyer-ter-Vehn, G. Pretzler, P. Thirolf, D. Habs, and K. J. Witte, "Multi-MeV electron beam generation by direct laser acceleration in high-density plasma channels," Phys. Rev. Lett. **83**, 4772–4775 (1999).
[58]I. Cohen, T. Meir, K. Tangtartharakul, L. Perelmutter, M. Elkind, Y. Gershuni, A. Levanon, A. V. Arefiev, and I. Pomerantz, "Undepleted direct laser acceleration," Sci. Adv. **10**, eadk1947 (2024).
[59]J. Perl, J. Shin, J. Schümann, B. Faddegon, and H. Paganetti, "TOPAS: An innovative proton Monte Carlo platform for research and clinical applications," Med. Phys. **39**, 6818–6837 (2012).
[60]B. Faddegon, J. Ramos-Méndez, J. Schuemann, A. McNamara, J. Shin, J. Perl, and H. Paganetti, "The TOPAS tool for particle simulation, a Monte Carlo simulation tool for physics, biology and clinical research," Phys. Med. **72**, 114–121 (2020).
[61]V. Drozdovitch, A. B. Brill, R. J. Callahan, J. A. Clanton, A. DePietro, S. J. Goldsmith, B. S. Greenspan, M. D. Gross, M. T. Hays, S. C. Moore, J. A. Ponto, W. W. Shreeve, D. R. Melo, M. S. Linet, and S. L. Simon, "Use of radiopharmaceuticals in diagnostic nuclear medicine in the United States: 1960–2010," Health Phys. **108**, 520–537 (2015).
[62]J. Götzfried, A. Döpp, M. F. Gilljohann, F. M. Foerster, H. Ding, S. Schindler, G. Schilling, A. Buck, L. Veisz, and S. Karsch, "Physics of high-charge electron beams in laser-plasma wakefields," Phys. Rev. X **10**, 041015 (2020).
[63]J. Feng, Y. Li, J. Tan, W. Wang, Y. Li, X. Zhang, Y. Meng, X. Ge, F. Liu, W. Yan, C. Fu, L. Chen, and J. Zhang, "Laser plasma-accelerated ultra-intense electron beam for efficiently exciting nuclear isomers," Laser Photonics Rev. **17**, 2300514 (2023).

[64]O. Jakobsson, A. Bonatto, Y. Li, Y. Zhao, R. P. Nunes, B. Williamson, G. Xia, and T. Tajima, "Tailored plasma-density profiles for enhanced energy extraction in passive plasma beam dumps," Plasma Phys. Control. Fusion **61**, 124002 (2019).
[65]G. Plyushchev, R. Kersevan, A. Petrenko, and P. Muggli, "A rubidium vapor source for a plasma source for awake," J. Phys. D: Appl. Phys. **51**, 025203 (2018).
[66]T. M. Martin, T. Harahsheh, B. Munoz, Z. Hamoui, R. Clanton, J. Douglas, P. Brown, and G. Akabani, "Production of ^{99}Mo/^{99m}Tc via photoneutron reaction using natural molybdenum and enriched ^{100}Mo: Part 1, theoretical analysis," J. Radioanal. Nucl. Chem. **314**, 1051–1062 (2017).
[67]B. A. Broder, R. Freifelder, A. Kucharski, and C.-T. Chen, "Modelling cyclotron-based production of radioisotopes via TOPAS," Phys. Med. Biol. **68**, 015017 (2023).
[68]S. Agostinelli, J. Allison, K. Amako, J. Apostolakis, H. Araujo, P. Arce, M. Asai, D. Axen, S. Banerjee, G. Barrand, F. Behner, L. Bellagamba, J. Boudreau, L. Broglia, A. Brunengo, H. Burkhardt, S. Chauvie, J. Chuma, R. Chytracek, G. Cooperman, G. Cosmo, P. Degtyarenko, A. Dell'Acqua, G. Depaola, D. Dietrich, R. Enami, A. Feliciello, C. Ferguson, H. Fesefeldt, G. Folger, F. Foppiano, A. Forti, S. Garelli, S. Giani, R. Giannitrapani, D. Gibin, J. Gómez Cadenas, I. González, G. Gracia Abril, G. Greeniaus, W. Greiner, V. Grichine, A. Grossheim, S. Guatelli, P. Gumplinger, R. Hamatsu, K. Hashimoto, H. Hasui, A. Heikkinen, A. Howard, V. Ivanchenko, A. Johnson, F. Jones, J. Kallenbach, N. Kanaya, M. Kawabata, Y. Kawabata, M. Kawaguti, S. Kelner, P. Kent, A. Kimura, T. Kodama, R. Kokoulin, M. Kossov, H. Kurashige, E. Lamanna, T. Lampén, V. Lara, V. Lefebure, F. Lei, M. Liendl, W. Lockman, F. Longo, S. Magni, M. Maire, E. Medernach, K. Minamimoto, P. Mora de Freitas, Y. Morita, K. Murakami, M. Nagamatu, R. Nartallo, P. Nieminen, T. Nishimura, K. Ohtsubo, M. Okamura, S. O'Neale, Y. Oohata, K. Paech, J. Perl, A. Pfeiffer, M. Pia, F. Ranjard, A. Rybin, S. Sadilov, E. Di Salvo, G. Santin, T. Sasaki, N. Savvas, Y. Sawada, S. Scherer, S. Sei, V. Sirotenko, D. Smith, N. Starkov, H. Stoecker, J. Sulkimo, M. Takahata, S. Tanaka, E. Tcherniaev, E. Safai Tehrani, M. Tropeano, P. Truscott, H. Uno, L. Urban, P. Urban, M. Verderi, A. Walkden, W. Wander, H. Weber, J. Wellisch, T. Wenaus, D. Williams, D. Wright, T. Yamada, H. Yoshida, and D. Zschiesche, "Geant4—a simulation toolkit," Nucl. Instrum. Methods Phys. Res. A **506**, 250–303 (2003).
[69]See https://ekspla.com/products/multi-tw-khz-tunable-femtosecond-opcpa-system-ultraflux-custom/ for "Multi TW few cycle OPCPA systems."
[70]See https://https://amplitude-laser.com/products/femtosecond-lasers/lasers-for-science/arco/ for "Femtosecond lasers."